Numerical Simulation of Cavitation Phenomena inside Fuel Injector Nozzles

BARIS BICER

(Degree)
博士（工学）

(Date of Degree)
2015-09-25

(Date of Publication)
2016-09-01

(Resource Type)
doctoral thesis

(Report Number)
甲第6491号

(URL)
https://hdl.handle.net/20.500.14094/D1006491

Numerical Simulation of Cavitation Phenomena inside Fuel Injector Nozzles

by

BARIŞ BİÇER

A thesis

presented to Graduate School of Maritime Sciences of

Kobe University in fulfilment of

the thesis requirement for the degree of

Doctor of Philosophy

Kobe University,

Kobe, Japan

July, 2015

Abstract

The occurrence of cavitation phenomena inside a nozzle of a fuel injector for diesel engines is directly connected with local pressure drop. Understanding of cavitation flow in a nozzle of a fuel injector has major importance, since it plays a significant role in the fuel spray atomization, which strongly affects diesel engine performance and emissions.

The main goal of this dissertation is to establish an effective combination of numerical cavitation models, which can accurately simulate the complex recirculation flow, the cloud cavitation shedding and the re-entrant jet inside fuel injector nozzles. For this purpose, both an in house code and the free computational fluid dynamics (CFD) package OpenFOAM are used. Numerical results are validated quantitatively through the comparison with experimental results of turbulent cavitating flows in a one-side rectangular nozzle. The images of cavitation are captured by a high-speed camera and the turbulent velocity is measured by a Laser Doppler Velocimetry (LDV). The presented work is divided into three major parts:

1. The first objective of the presented thesis is to assess the applicability of the existing bubble dynamics models, i.e., the Rayleigh-Plesset (RP) equation and simplified RP equation, which is called Rayleigh (R) equation, to the prediction of the growth and collapse of cavitation bubbles in Diesel fuel injector. Then, a Modified Rayleigh (MR) equation, based on the critical pressure P_C, is proposed to overcome the drawbacks of the existing models. The agreement between calculated and measured bubble radii confirmed the validity of the RP equation. Numerical calculations are performed under various conditions, such as a water injection at low injection pressure and a diesel fuel injection at high injection pressure. The proposed MR equation is confirmed to give a good estimation of the growth and collapse rates of cavitation bubbles under various pressure conditions.

2. Next, the applicability of the various combinations of the models on the turbulent

flow and cavitation to the numerical simulations of the transient cavitating flows in a nozzle is examined.

(a) The first combination consists of the RNG $k-\varepsilon$ model and barotropic cavitation model or Kunz's cavitation model, which are not based on the bubble dynamics models. OpenFOAM is used for the numerical calculations. As a result, it is confirmed that the combination of Homogeneous Equilibrium Model (HEM), a Barotropic (Baro) equation and a RANS turbulence model, RNG $k-\varepsilon$ model, underestimates cavitation length and cannot reproduce transient cavitation behaviour, which plays a dominant role in atomization of injected liquid jet and spray. While the combination of Kunz's cavitation model and RNG $k-\varepsilon$ model is able to predict the recirculation flow and the cloud shedding well by tuning the model's empirical constants.

(b) Second, the combination in a house code based on Lagrangian Bubble Tracking Method (BTM), RP equation and Large Eddy Simulation (LES) is examined. This combination is confirmed to give a good prediction for the cavitation length, thickness as well as cavitation cloud shedding. However, it requires a fine grid and a long CPU time, and is applicable only to incipient cavitation.

(c) The final combination of Volume-of-Fluids (VOF), RNG $k-\varepsilon$ model and Mass Transfer Model (MTM), whose source terms are given by R or MR equations, is tested using OpenFOAM. It is found that the recirculation flow, the cloud shedding and the re-entrant are well simulated by the combination with MR equation, whereas cavitation length and thickness are overestimated with R equation.

3. Finally, the two-equation RANS turbulence models, such as $k-\omega$ SST and RNG $k-\varepsilon$ models, with various meshes of different cell sizes and the one equation eddy viscosity model under the framework of Large Eddy Simulation (LES) with a fine mesh are investigated to simulate the turbulent flow in an one-side rectangular nozzle. The results conclude that RNG $k-\varepsilon$ model with MR equation gives a good prediction for the cavitation length and thickness in a nozzle with the fine mesh of less than 50 μm in the minimum mesh size Δx_{min}. The cavitation cloud shedding is well reproduced by RNG $k-\varepsilon$ using the mesh with the minimum mesh size Δx_{min}=50 μm. The $k-\omega$ SST model with MR equation predicts well the cavitation

length and thickness in a nozzle with the finer mesh with less than 25 μm in Δx_{min}. Also, the cavitation cloud shedding is well simulated with the $k-\omega$ SST model and MR equation using fine mesh size Δx_{min}=25 μm. The recirculation flow and the vortex shedding accompanied by cavitation cloud until the exit of the nozzle are well simulated with the combination of MR/LES models using the fine grid with minimum mesh size Δx_{min} of 4.4 μm compared to RANS models.

The study concludes that the MR equation together with appropriate turbulence model and a fine mesh can simulate not only the complex cavitating recirculation flow, cloud cavitation shedding and re-entrant jet flow but also cavitation thickness, length as well as mean and turbulence velocities quantitatively, and can be used to explore cavitation phenomena inside fuel injector nozzles.

List of Publications

This PhD thesis is written based on following papers:

1. **Barış Biçer**, Akira Sou, **2015**: "Application of the Improved Cavitation Model to Turbulent Cavitating Flow in Fuel Injector Nozzle," *submitted to the International Journal of Applied Mathematical Modelling*, (in review).

2. **Barış Biçer**, Akira Sou, **2015**: "Numerical Models for Simulation of Cavitation in Diesel Injector Nozzles," *Atomization and Spray*, 25 (1), 1-18.

3. **Barış Biçer**, Akira Sou, **2014**: "Bubble Dynamics Model for Predicting the Growth and Collapse of Cavitation Bubbles in Diesel Injectors," *Atomization and Spray*, 24 (10), 915-935.

4. Akira Sou, **Barış Biçer**, **2014**: "Numerical Simulation of incipient Cavitation Flow in a Nozzle of Fuel Injector," *Computers & Fluids*, 103, 42-48.

5. **Barış Biçer**, Akira Sou, **2015**: "Turbulence and Bubble Dynamics Models to Simulate Transient Cavitation Flow in Fuel Injector Nozzle," *ICLASS 2015,* 13^{th} *Triennial International Conference on Liquid Atomization and Spray Systems,*Tainan, TAIWAN.

6. **Barış Biçer**, Akira Sou, **2014**: "Numerical Simulation of Turbulent Cavitating Flow in Diesel Fuel Injector," *Proceedings of the* 3^{rd} *International Symposium of Maritime Sciences (ISMS),* 3, 33-38, Kobe, JAPAN.

7. **Barış Biçer**, Akira Sou, **2014**: "Models for Prediction of Cavitation in Diesel Injector Nozzles," 9^{th} *OpenFOAM Workshop,* Zagreb, CROATIA.

8. **Barış Biçer**, Akira Sou, **2013**: "Numerical Simulation of Cavitation Phenomena in Diesel Injector Nozzles," 16^{th} *Annual Conference ILASS-ASIA,* 58-65, Nagasaki, JAPAN.

Acknowledgement

I have had an exciting and challenging period through the past 5 years in Kobe University and Japan, where I have definitely learnt how to overcome the difficulties and to solve the problems inside life. Therefore, Japan gave me a big chance to discover the treasures and competence inside myself.

First of all, I would like to express my sincere gratitude to my supervisor, Prof. Akira Sou, for his helpful comments, steady encouragement, inspiration and valuable guidance throughout my PhD. I am very grateful that he showed me how to have a good skill for not only present research but also for future and also provided the opportunities to pursue my study as well as for improving my knowledge and expertise in the nozzle cavitation and CFD area.

I would also express my thanks to my previous supervisor Prof. Makoto Uchida for his all supports and guidance. Then, I would like to convey my gratefulness to Prof. Akihisa Abe for his kind comments and revision to improve the quality of my thesis. Moreover, I would like to acknowledge Prof. Masao Furusho for his great financial support to attend the OpenFOAM® course in Chalmers University, which gave to me an extra motivation, confidence and great experience about cavitation modelling to finish my thesis.

I would also like to say a big thank you for Mr. Goshima, the other Professors, officer, fellows and good friends in the Graduate School of Maritime Sciences in Kobe University, for the joy, collaboration, help and support they brought me. In addition, I would like to warmly thank to members of EFS Lab for their kind friendship. The financial support by the Ministry of Education, Culture, Sports, Science Technology (MEXT) of the Japanese Government and research funds are greatly appreciated.

I would also like to express my big thanks to the developers of the OpenFOAM® package for their hard work, fabulous collaboration and free releasing.

The last but not least, a big warm thank and appreciation first goes to my sweetie wife because of her great patient, love, support and dedication for me. She gave me two

cute kids HANNA NUR and KERIM ERDOGAN, whose presents are one of the best power push me forward. Secondly, i would like to express my endless appreciation for my mum, dad, sisters, relatives and Turkish friends. Their love, prays and sacrifice are great encouragement for me to fulfil my dreams through this journey.

Finally, I would like to say my big appreciations and glorification to my creator, ALLAH. I certainly know that I was not able successfully to complete my PhD without his support, help and guidance. Therefore; *"... My success (in my task) can only come from ALLAH. In Him I trust, and unto Him I look"*.(HUD-88)

"Gayret bizden, tevfik ve başarı Allah'tandır."

Barış Biçer

June, 2015

"Dedicated to RAHMAN, who is most merciful..."

Contents

List of Figures

List of Tables

Abbreviations

BTM	**B**ubble **T**racking **M**ethod
CFD	**C**omputatinal **F**luids **D**ynamics
DNS	**D**irect **N**umerical **S**imulation
FVM	**F**inite **V**olume **M**ethod
HEM	**H**omogeneous **E**quilibrium **M**odels
MTM	**M**ass **T**ransfer **M**odels
LDV	**L**aser **D**oppler **V**elocimetry
LES	**L**arge **E**ddy **S**imulation
PISO	**P**ressure-**I**mplicit with **S**plitting of **O**perators
RANS	**R**eynolds-**A**veraged-**N**avier-**S**tokes
SIMPLE	**S**emi-**I**mlicit **M**ethod for Pressure-**L**inked **E**quations
TVD	**T**otal **V**ariation **D**iminishing
VOF	**V**oume-**O**f-**F**luids

Nomenclature

Roman Symbols

a	speed of sound $[m/s]$
A	cross-sectional area of nozzle $[m^2]$
C_c	condensation rate constant
C_v	vaporization rate constant
C_{VM}	virtual mass coefficient
Co	courant number
D	diameter $[\mu m]$
$\mathbf{g}$	gravitational acceleration $[m/s^2]$
F_1	first blending function
F_2	second blending function
F_d	drag force $[N]$
F_{lf}	lift force $[N]$
k	turbulence kinetic energy $[m^2/s^2]$
K	cavitation number
l	characteristic length $[mm]$
L	length $[mm]$
n_0	bubble number density $[1/m^3]$
P	pressure $[Pa]$
R	radius $[\mu m]$
R_c	condensation source term
R_e	vaporization source term
Re_n	Reynolds number
S	rate of strain tensor
t	thickness of nozzle $[mm]$
$\mathbf{U}$	velocity $[m/s]$
V_{in}	inlet velocity of a nozzle $[m/s]$

V_n	mean velocity in a nozzle [m/s]
W	width of nozzle [mm]

Greek Symbols

α	volume fraction [-]
Δt	time step [s]
Δx	cell size in x direction [μm]
ρ	density [kg/m^3]
ρ^0	density at given temperature [kg/m^3]
μ	dynamic viscosity [kg/ms]
ν	kinematic viscosity [m^2/s]
ϵ	turbulent dissipation rate [m^3/s^2]
ω	the specific rate of turbulent dissipation rate [$1/s$]
Ψ	compressibility [s^2/m^2]
σ	surface tension [N/m]

Subscripts

0	initial
b	bubble
$back$	back
C	critical
cav	cavitation
eff	effective
equ	equilibrium
inj	injection
G	gas
L	liquid
m	mixture
max	maximum
min	minimum
n	nozzle
out	outlet
sat	saturation

sgs	sub-grid scale
u	upstream
V	vapour
t	turbulence

Chapter 1

Introduction

1.1 Motivation

In today's world, the environmental pollution caused by fuel emissions from transportation such as cars and heavy vehicles has been reached to be one of the major problems due to excessively releasing harmful gases such as soot, NO_x and CO_2. Figure 1.1 shows global carbon emission from fossil fuels which significantly rose since 1990 [1]. As seen in Figure 1.1, CO_2 emissions have increased by over 16 times between 1900-2008, and by about 1.5 times between 1990-2008.

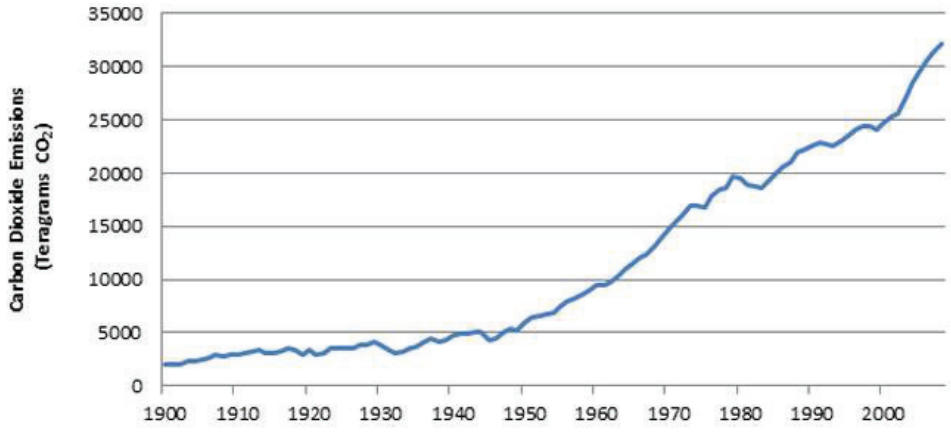

Figure 1.1: Global CO_2 emissions from fossil fuels 1900-2008 [1]

This situation directly threats the life of humans and animals, and results in vital diseases [2]. Lots of efforts have been paid to find the different energy sources, which are called "renewable energy sources" with less polluting. However, due to their high cost in the production and usage, fossil fuels are still dominating and widely used to convert the chemical energy into mechanical power in all over the world. Therefore, the diesel engine and its combustion became one of the challenging topics for the engineers to reduce the

released harmful gases.

One of the options to decrease the NO_x, CO_2 and other harmful gases released by diesel engine is to increase the engine efficiency. The fuel spray atomization inside a diesel engine has an essential importance since it reduces the exhaust gas emissions and increases the engine efficiency. Before the combustion process, the amount of fuel is injected into the combustion chamber and will be mixed with high heated air. The injector nozzle is one of the particular components, which influences the mixing process of fuel and air in the combustion chamber. Certainly, this mixing efficiency is changing according to size and shape of nozzles, number of the injection holes and their positions in combustion chamber. Therefore, the internal nozzle flow characteristics have to be understood well in order to design a fuel injector, since it directly affects the fuel spray characteristics.

Previous studies pointed out that characteristics of fuel spray inside combustion chambers are strongly influenced by cavitation which takes place inside fuel injector nozzle [3–6].

1.1.1 Cavitation Definition

Figure 1.2 shows the schematic phase diagram of water which is given for pressure versus temperature. The horizontal motion corresponds to well-known process of boiling by heating liquid at constant pressure. When the temperature reaches boiling point, the phase changes from liquid to vapour will be seen. On the other hand, vertical motion displays the main concept of cavitation phenomena, which occurs when the local pressure drops below saturation pressure under the constant temperature. As seen in Figure 1.2, the driving phenomenon of boiling is an increase in temperature at constant pressure, whereas the driving phenomena cavitation is the sudden pressure reduction.

Cavitation is usually undesirable phenomena for the hydraulic machinery applications since the cavitation pockets collapses and results in sharp pressure peaks on adjacent surfaces, which leads to erosion. That is why the cavitation may be known as a main reason of several negative effects, such as noise, vibrations, performance alterations, erosion and structural damages on e.g. pump impellers, turbines, ship propellers or in valves [7, 8].

Contrary to the above mentioned apprehension, cavitation can be thought beneficial in fuel injector's nozzles since it improves the atomization of diesel spray. This situation makes the cavitation an important issue in design and operation of diesel engine, which should be taken under control, or at least well understood.

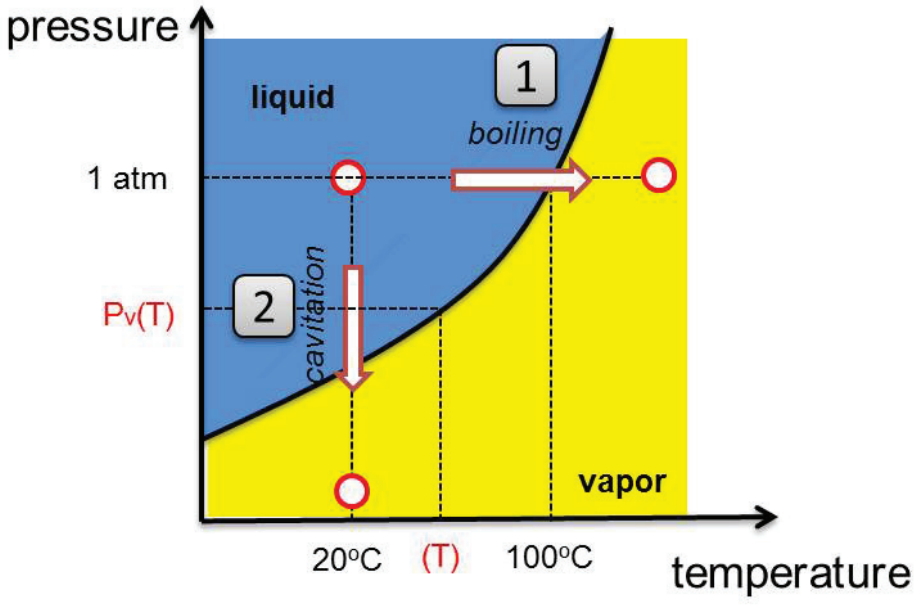

Figure 1.2: Water phase change diagram

1.1.2 Cavitation in Fuel Injector Nozzle

Cavitation in a fuel injector nozzle can be defined as the phase transition of liquid into vapour due to sudden local pressure drop. Figure 1.3 shows the schematic illustration of the cavitation phenomena occurring inside a nozzle hole. As seen at the entrance of nozzle, there is a strong change in cross-section and flow direction due to present of sharp edges. Addition to this, the boundary layer tends to separate from the hole wall and the vena contracta is formed. As a consequence, a recirculation zone appears between the vena contracta and the orifice wall. There is a pressure fluctuation in this region due to the acceleration of the fluid. During the pressure depression, if the static pressure falls below the vaporization pressure, the cavitation will be appeared. More specifically, to start the cavitation in this region, presence of nuclei which is called as small bubbles and their diameters change around $10^{-6}\mu$m, are needed. If the small bubbles enter into the low pressure region, they start to grow up and lead to cavitation.

Cavitation inside a fuel injector nozzle tends to enhance the jet turbulence which leads to increase the spray angle and to promote the fuel atomization of the diesel engine as shown in Figure 1.4. As seen in Figure 1.4, when the injection pressure P_{inj} is low, the cavitation only appears at the entrance of the nozzle. With the increasing of P_{inj}, cavitation inside nozzle starts to develop and extend throughout nozzle exit. As a result, cavitation alters the velocity profile and turbulence level inside nozzle, and directly affects the primary

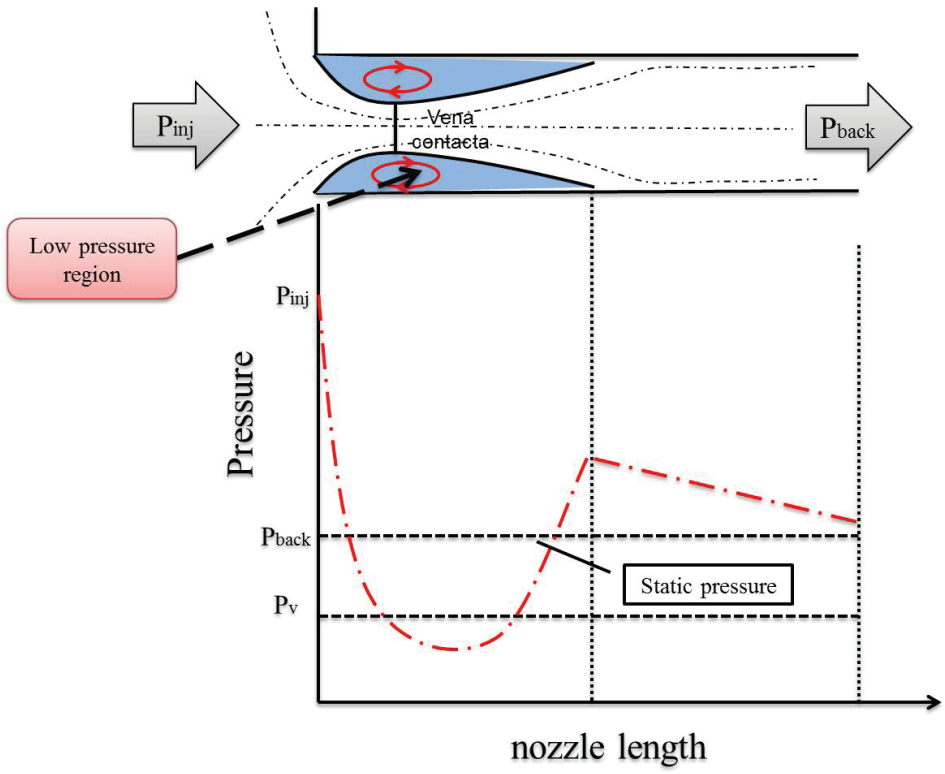

Figure 1.3: Schematic illustration of cavitation inside nozzle

break-up and subsequent atomization of fuel. Finally, the enhanced atomization also results in better combustion process, which in turn will decrease the fuel consumption and reduce the released harmful exhaust gases and particulate emissions.

Addition to benefits of the cavitation inside fuel injector nozzle, it should be mentioned about the disadvantages that can be seen in the multi-hole nozzle as a severe erosion problem. In some cases, the erosion problem can lead to disastrous results. Therefore, significant damages and erosion can be seen on the provided most of modern nozzles, which are particularly used with high pressure common-rail systems after operating few hundred hours of operation [9].

In order to better understand the effects of cavitation inside injector nozzle, a large variety of experimental works have been performed using large-scale transparent nozzles [4, 10–14], which enable to facilitate visualization of cavitation structure. Figure 1.5 shows the enlarged symmetric transparent nozzle used in our experiment, whose length L_N, width W_N and thickness t_N are 16 mm, 4 mm and 2 mm, respectively.

Although, there are some experimental works using real size of injector nozzle [5, 15–17], it should be noted that performing experiment with an actual nozzle is very difficult due to:

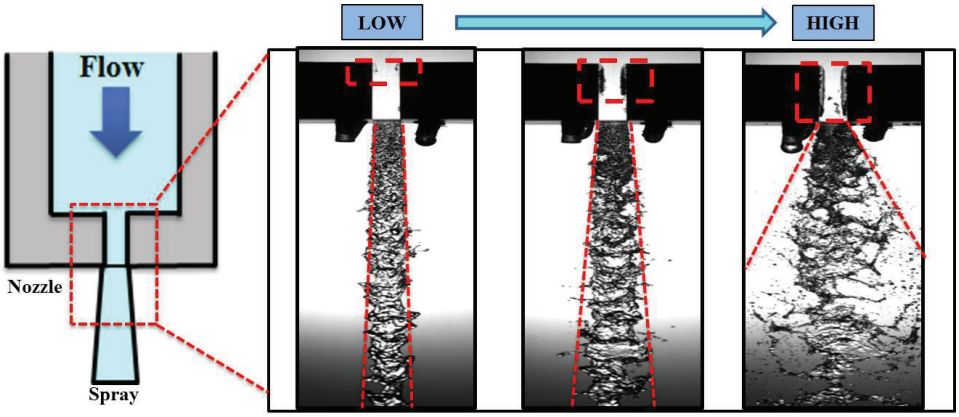

Figure 1.4: Cavitation in rectangular nozzle and spray discharged liquid jet

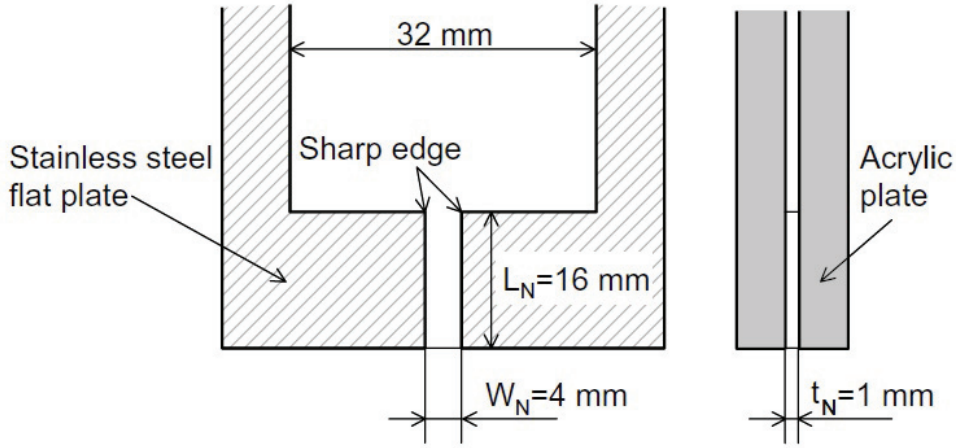

Figure 1.5: Large scale rectangular nozzle [6]

- refraction of light at cylindrical side wall of the nozzles,
- very small scale of the nozzles of about 0.1 mm in diameter and 1 mm in length,
- operating at high injection pressure (up to 1800-2000 bar) using common rail injection system, which may bang up the experimental tools,
- and high velocity up to hundreds meters per second in the nozzles,
- the total time of the operation inside the nozzle in the order of few ms,
- complexity of the transient cavitating flow, which is affected by the dynamic behaviour of the injector shape.

These drawbacks make the experimental visualization and measurements extremely formidable in an actual nozzle, and also create a big difficulty to execute the experimental

work at exactly same operating conditions and geometry. Therefore, lots of numerical models have been developed for many years to predict and simulate the cavitation in injector nozzles [18–26]. The huge density and viscosity differences between liquid and gas phases make the numerical simulations difficult. That is why the experimental and numerical works of the turbulent cavitating flow inside fuel injector nozzle and its influence on spray atomization are still an on-going and prominent research topic.

1.2 Objectives and Achievements

As explained in the previous section, a good understanding of cavitation flow in a nozzle of fuel injector for diesel engines has major importance, since it plays a significant role in the fuel spray atomization and strongly affects diesel engine performance and emissions. Because of the experimental difficulties connected with flow measurements and visualization inside actual size of injector nozzle, Computational Fluid Dynamics (CFD) simulations stand for an important tool to predict and model the cavitation inside injector nozzle with the development of high performance computers. Therefore, CFD works becomes in great demand topic compared to experimental studies due to being easy, low work-time and low-cost.

The main objective of the present dissertation is to develop an effective combination of numerical models, which is able to simulate the complex recirculation flow, the cloud cavitation shedding and the re-entrant jet inside fuel injector nozzles. For this purpose, both an in-house code and OpenFOAM®, which is based on object-oriented programming, free open source CFD tool [27] are used. Numerical results are validated using experimental results of an one-side rectangular nozzle whose images were captured by a high-speed camera and the turbulent velocity was measured by a Laser Doppler Velocimetry (LDV) [19]. Following achievements are performed within present thesis:

- The applicability of the existing bubble dynamics models, i.e., the Rayleigh-Plesset (RP) equation, simplified RP which is called Rayleigh (R) equation, was assessed to the prediction of the growth and collapse of cavitation bubbles in diesel fuel injector. Then, a Modified Rayleigh (MR) equation taking into account the critical pressure P_c is proposed to overcome the drawbacks of the RP and R equations.

- Applicability of the various combinations of models to cavitation flow simulation in a nozzle of liquid fuel injector is examined.

  - First, applicability of cavitation models which are not based on bubble dynamics models, such as combination of Homogeneous Equilibrium Model (HEM), a Barotropic (Baro) equation and RANS turbulence model ($RNGk-\varepsilon$), and Kunz's cavitation model [22] with VOF and RNG $k-\varepsilon$ are examined using OpenFOAM® software.
  - Second, in a house code consists of Lagrangian Bubble Tracking Method (BTM), RP equation and Large Eddy Simulation (LES) is applied for the simulation of nozzle cavitation.
  - Third, CFD applicability of the MR equation is shown with the combination of Volume-of-Fluids (VOF), Mass Transfer Model (MTM) and RNG $k-\varepsilon$ model using OpenFOAM®.

- Finally, the effect of turbulence models on cavitation simulation was presented using $k-\omega$ SST, RNG $k-\varepsilon$ and LES (*k-equation eddy-viscosity*) models with MR equation in OpenFOAM®.

The numerical results are validated through the experimental results of one-side rectangular nozzle whose transient cavitation distribution was taken by high-speed camera, and mean and turbulent velocities were obtained by LDV, which are useful for quantitative validation.

1.3 Thesis Outline

The present work consists of nine chapters.

1. ***Chapter 1*** includes the introductory, where the motivation of this thesis is outlined along with a brief explanation of air pollution caused by fossil fuels. After that, definition of cavitation is presented, and formation of cavitation inside injector nozzle is explained. Thesis objectives and achievements are also given with the thesis outline in the same chapter.

2. ***Chapter 2*** reviews previous relevant publications of experimental and numerical studies on cavitation occurring in both enlarged and real size of injector nozzles. Emphasis has been given to numerical publications, in which different cavitation models were used.

3. ***Chapter 3*** presents the applicability of the existing bubble dynamics models, i.e., RP equation and R equation, is assessed to predict the growth and collapse of cavitation bubbles in diesel fuel injector. Additionally, a MR equation based on the critical pressure P_c equation is proposed to overcome the drawbacks of the former models. Results are analytically confirmed to agree with the prediction of RP equation.

4. ***Chapter 4*** exhibits the experimental equipment which includes experimental conditions and results that are used for the validation of the numerical calculations.

5. ***Chapter 5*** shows the applicability of the different combinations of cavitation models, which ignore the bubble dynamics, such as barotropic cavitation model and Kunz's cavitation model to turbulent cavitation flows in a fuel injector nozzle. Turbulent effect is taken into account using RNG $k-\varepsilon$.

6. ***Chapter 6*** provides the details and results related to bubble dynamics with the combination model of Eularian-Lagrangian Bubble Tracking Method (BTM), Rayleigh-Plesset (RP) and Large Eddy Simulation, which is in-house code.

7. ***Chapter 7*** presents applicability of proposed MR equation to turbulent cavitating flows and its superiority versus R equation in a fuel injector nozzle using RNG $k-\varepsilon$ turbulence model.

8. ***Chapter 8*** indicates the effects of the turbulence models on cavitation simulation using $k-\omega$ SST, RNG $k-\varepsilon$ and LES (*k-equation eddy-viscosity*) models with MR equation in OpenFOAM®.

9. Finally, ***Chapter 9*** shows the summary of the major results and findings of the present thesis.

Chapter 2

Literature Review

2.1 Introduction

A great number of studies have been provided on the topic of cavitation inside fuel injector nozzles and its effect on spray atomization both experimentally and numerically in the literature heretofore. In this chapter, a literature survey, which supplies an overview of research carried out on relevant to the present thesis, is presented. Addition to this, important findings on the topic of nozzle cavitating flow are provided.

The survey mainly focuses on experimental studies conducted with large and real size injector nozzles, which have aim of highlighting the fundamental understanding of the cavitation phenomena inside fuel injector nozzles. Additionally, various numerical investigations of cavitation models are discussed by giving important numerical findings. Finally, some of studies particularly relevant to present thesis are investigated in more detail.

2.2 Experimental Observations on Internal Nozzle Flow

A large variety of experimental works have been performed on cavitation in fuel injector nozzles, which lead to contribution to the understanding of the cavitation phenomena and its influence on spray atomization. These experimental efforts can be classified into two groups regarding to using scaled-up and real size nozzles.

An early experimental work in fuel injector nozzle was carried out by Bergwerk [28]. He conducted experiments using transparent simplified large-scale and real size single hole injector nozzles to investigate the differences in cavitating flows. He found that cavitation developing and hydraulic flip are observed with the increasing of cavitation number in large scale nozzle, whereas a relative effect of geometry imperfections such as ruffled

spray with increasing cavitation number in real small scale nozzle is captured.

Concerning to same framework, the effect of the nozzle geometry related to cavitation number and Reynolds number was studied by Spikes and Pennington [29]. They employed small transparent nozzle with a steady-state flow rig and predicted discharge coefficient. Finally, they showed that cavitation results are more affected in the variation of the discharge coefficient compared to Reynolds number when the the flow is turbulent.

Nurick [30] conducted experiments in scaled-up transparent nozzles using both circular and rectangular sharp-edged geometries. He found that the cavitation inside nozzle and shape of hydraulic flip vary subject to cavitation number, nozzle radius, length to diameter ratios of nozzle, and differences between upstream and downstream pressures. He provided a phenomenological model to be mostly used for a limiting case of axi-symmetric orifices.

Further, Wu *et al.* [31] examined more detailed measurements related to different pressures and spray atomization, and showed the influence of the cavitation on atomized spray cone angle.

More recently, Bode *et al.* [32] carried out study on cavitating flow using a real size transparent nozzle. They explored a cavitation film appearing at the inlet of nozzle since they raised up the pressure difference, even though the pressure conditions were smaller than real injector. Additionally, the collapsing of the cavitating bubbles are observed at the outside of injector nozzle.

Hiroyasu *et al.* [3] conducted one of the useful experiment using large-scale transparent nozzle to predict the presence of cavitation. They took pictures in the low speed of nozzle flow to observe the correlation between the nozzle cavitation and spray atomization. They found out that spray atomization is improved by the extension of cavitation to the exit of injector nozzle, and first break-up length is decreased due to the present of cavitation inside nozzle. These efforts provide an important correlation to better understand the cavitating nozzle flow and its influence on spray break-up. They also showed that the nozzle length does not have any important effect on the discharge coefficient.

Soteriou *et al.* [11] performed experiment using large-scale transparent injector nozzles to comprehend the different flow regimes and their forming inside nozzle. As a result, they classified the cavitation into three distinct regions, i.e., a separated boundary layer inner region, a main stream flow, and an attached boundary layer inner region. They also showed that the presence of the needle leads to increase the turbulence in the sac

and to limit hydraulic flip in the standard nozzle, whereas hydraulic flip tends to take place with the increasing of the cavitation number without needle. Furthermore, Soteriou *et al.* [33, 34] used laser light sheet illumination in order to investigate the onset and developing of cavitation inside large scale nozzle with the aim of getting more deep-insight into the internal flow characteristics of nozzle. Laser Droplet Velocimetry (LDV) technique was used to take measurements of the velocity profiles within the nozzle under the non-cavitating conditions. This technique permits to make further investigation of new details on the cavitation flow characteristics inside nozzles.

Chaves *et al.* [4] extended the work of Soteriou *et al.* [11] and carried out some measurements in small-size nozzles with high injection pressure varying up to 100 MPa, and back pressure was set to be 0.1 MPa as atmospheric pressure. They showed the description of the supercavitation, in which the cavities moving through the exit of the nozzle, as a distinct from hydraulic flip. They further tested the scale effects of nozzle using available large-scale results and their own results for actual size nozzle. According to findings, they concluded that cavitation cannot be scaled-up due to having own length scale which was not depended on the length scale of nozzle geometry.

He and Ruiz [10] carried out experimental work with two-dimensional enlarged nozzle using water as the working fluid, and used LDV to measure the flow rate. They found out that cavitation has substantial impact on the velocity profile near the nozzle inlet. Subsequently, turbulence is predicted more higher after the cavitation started to appear.

Badock *et al.* [5] also carried out experiments using both laser sheet illumination and shadowgraph techniques to analyse the cavitation phenomena inside real size single hole of nozzle and spray break-up at the exit of nozzle hole. A Bosch common rail system was used for experiments to generate the unsteady injection conditions with the rail pressure up to 60 MPa. They predicted the view of liquid surrounded by a cavitating film using laser sheet illumination, whereas it was not visible with shadowgraph.

In the study of Arcoumanis *et al.* [35], cavitation monitored inside an actual size nozzle was compared with those obtained in a scaled-up transparent acrylic injector nozzle. They observed the appearance of string cavitation inside real size of nozzle only at low needle lift. They also employed LDV technique to measure the local mean velocity and the turbulent kinetic energy within the injector nozzle. They explored that cavitation in large-scale nozzles is observed in the form of foamy bubble clouds, while in the real-size nozzle, there are clear voids as same as shown by Chaves *et al.* [4]. This similarity indicates

that cavitation inside nozzle cannot be scaled-up.

Roth *et al.* [36] studied the dynamic behaviour of the incipient cavitation using transparent scaled-up mini-sac and VCO type's injector nozzles with six conical holes. LDV technique was also used to measure the details of velocity in non-cavitating and cavitating conditions. As an important finding, entrance of the injector nozzle formed by recirculation zones for cavitation incipient is defined as a possible region for cavitation initiation. As obtained from the LDV data, turbulence level is raised up in down part of the nozzle since the cavitation number increased. On the other hand, turbulent kinetic energy gradually decreases for all cavitation conditions to the level of non-cavitating flow.

Moreover, Winklhofer *et al.* [14] conducted experiments using one straight and two converging nozzles working with European diesel fuel. They made an extensive post-processing by taking 20-30 backscattered photos of the two-phase flow for each operating conditions, and they measured the velocity profiles using a fluorescence tracing method. To separate cavitation such as no cavitation and foamy regions, colour schemes were used with blue, red and greenish yellow, respectively as shown in Figure 2.1. They predicted that values of the mass flow rate are almost same for all three types of nozzle at cavitation inception and choked flow conditions, even though choked flow condition took place after cavitation inception appeared.

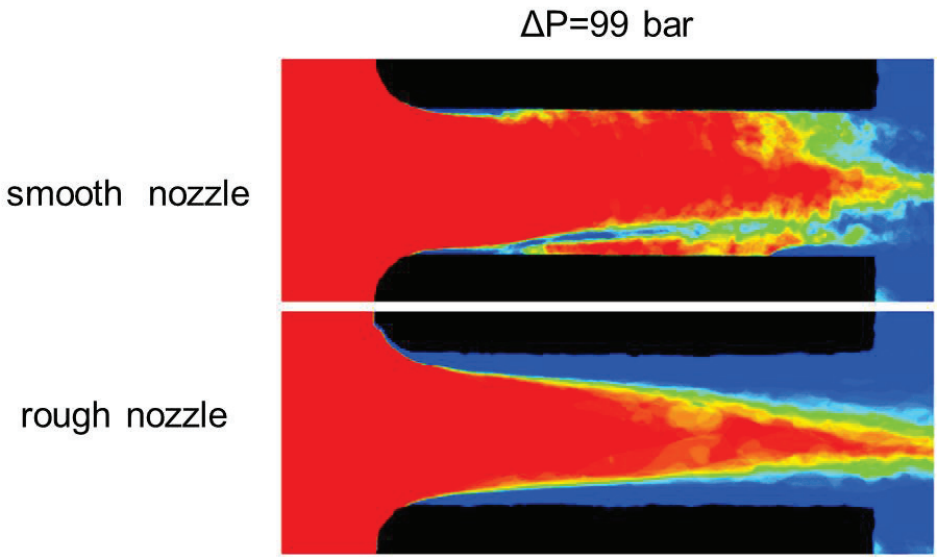

Figure 2.1: Cavitation fields [14]

Besides, Sou *et al.* [6] made an experimental work using large scale 2-D transparent single-hole nozzle. They used LDV technique to measure the velocity patterns inside nozzle

hole. They displayed that cavitation regime strongly affects the liquid jet atomization, and observed that cavitation inception starts as bubble clouds in the recirculation zone near the inlet of a nozzle. As shown in Figure 2.2, a cavitation regime in 2-D nozzles is divided into four group such as; no cavitation, developing cavitation, super cavitation and hydraulic flip. Finally, it was concluded that the generation of a long cavitation film forms the development of cavitation zone almost to the exit (supercavitation), and shedding of cavitation clouds accompanied in vortices finally induced a large deformation of the liquid jet.

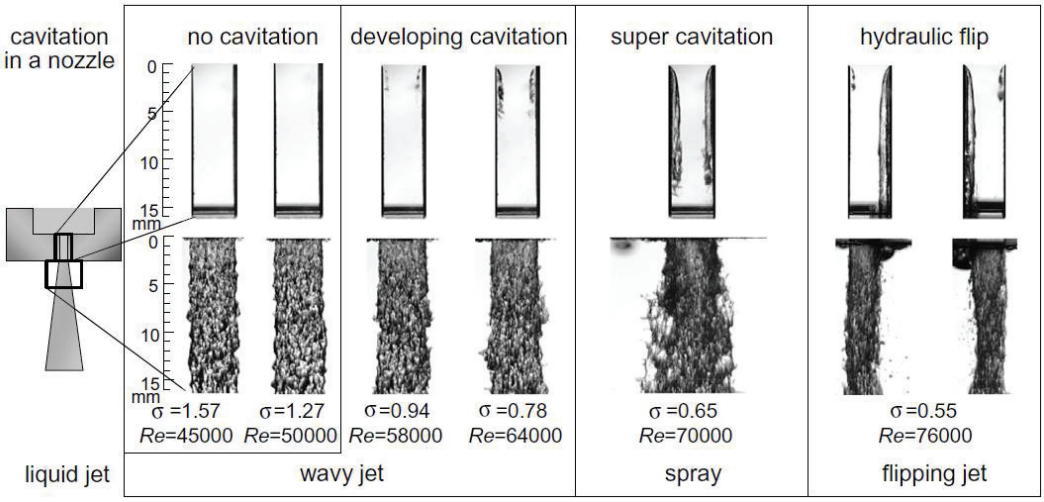

Figure 2.2: Cavitation regimes in 2-D nozzle [6]

Furthermore, Henry and Collicot [13] carried out experiment using large scale simplified nozzle. They found that a conglomeration of tiny bubbles formed the cavitation area. This invention also confirmed the assumption that a cavitation phenomenon is triggered by presence of nuclei. Further information about the experiments of scaled-up nozzles can be found in another previous works [37–42].

More focus on the actual size nozzle studies, Blessing *et al.* [43] conducted experiment using 1-hole and 6-hole mini-sac actual size nozzles with high pressure conditions. They used a CCD camera to visualize the internal flow, whereas shadowgraph images were used to measure the jet close to exit of nozzle. They found that cavitation decreases with the increasing of the inlet edge's rounding due to resulting in a higher uniformity. Collicott and Li [44] carried out a real scale nozzle experiment with 200 μm at real pressure condition up to 2100 bar. They explored that surface roughness and nozzle inlet shape have influence on the nozzle flow. Further information related cavitation experiment using real size

geometries can be found in the previous studies [16, 45–47].

Before end up this part, it is worthy to mention about another velocity measuring technique, which is called Particle Image Velocimetry (PIV). It is commonly used to measure the instantaneous velocity in the entire domain of the nozzle that is the the different point of PIV than LDV technique, which is mainly used for point measurement. Walther *et al.* [48] used PIV technique to predict the velocity fields inside actual size single hole fuel injector nozzle. Additionally, Aleiferis *et al.* [49] used PIV technique to examine the flow pattern inside optical acrylic type injector nozzle to facilitate the measurements. As a matter of fact, it should be noted that PIV technique is not widely used in fuel injector nozzles due to difficulty of the measurements in cavitating flow.

As explained so far, although experimental efforts provide important information in order to well understand the cavitation phenomena inside fuel injector nozzle, it still remains a big challenge for experimental studies, since most of them carried out either enlarged nozzle or under real pressure condition. Besides, visualization of high speed cavitating nozzle flow is needed more effort to get more reliable results.

2.3 Numerical Modelling of Multiphase Flows

The major difficulty of the modelling of the cavitation flows originates from a sharp variation in density due to sudden change in pressure gradient. Therefore, lots of useful numerical models have been developed for many years to simulate cavitation phenomena inside fuel injector nozzles. In this section, a brief survey of available approaches to multiphase cavitating flows and discussion of the substantial results in the cavitation modelling are presented.

Since the cavitation is multiphase phenomena, it should be noted that there are at least two different phases with different physical properties and their interactions. Due to simplicity, only liquid and gas phases are considered in the present thesis. In order to model the multiphase cavitating flows, it is firstly needed to specify two-phase treatment of the liquid and gas, and as well as the phase transition among the phases as source term. Figure 2.3 shows the classifications of the existing multiphase approaches in the literature used for the modelling of cavitation.

As seen in Figure 2.3, multiphase models used for the cavitation simulation are mainly divided into 3 groups such as, two-fluid models, volume tracking methods usually called as Volume-of-Fluids (VOF) and homogeneous equilibrium models (HEM), which

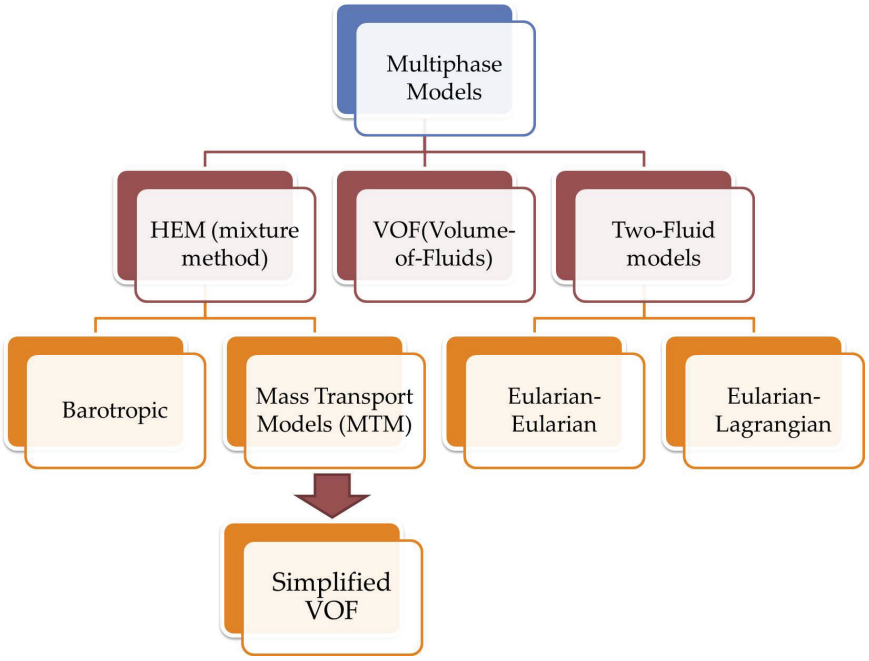

Figure 2.3: Classification of multiphase approaches

corresponds to perfectly mixture single fluid model.

2.3.1 Two-Fluid Models

This model treats the liquid and gas phases separately and assumes that both phases co-exist in every cell. The governing equations are solved for both phases and interactions between the phases are modelled by correlating. Therefore, the model does not assume the momentum equilibrium and can be used to predict different phase velocities. This model can be categorized into two sub-groups: Eularian-Eularian approach and Eularian-Lagrangian approach.

The Eularian-Eularian approach supposes that both liquid and gas phases are calculated in the Eularian frame as continuum phases. Yuan and Schnerr [50] used this approach to simulate the strong interaction of cavitating nozzle flow with the outside of jet formation. They included three different phases such as; liquid, vapour formed by liquid and gas which already exists inside of liquid. Therefore, three conservation equations are solved for each phases.

Addition to this, Alajbegovic *et al.* [23] also studied a three-phase flow in a swirl-type of injector. They treated cavitation as single mixture with the consideration of bubble dynamics and solved a set of conservation equations for each phase with $k - \varepsilon$ turbulence model. They validated model results with the experimental findings of steady-

state cavitation occurring inside a small scale asymmetrical nozzle. The results showed that model has ability to well predict the cavitation phenomena.

Battistoni and Grimaldi [51] examined the effects of the different fuels, i.e. a standard diesel fuel and a pure bio-diesel using Eularian-Eularian approach with consideration of bubble dynamics on moving grids from needle opening to closure. They used cylindrical and conical types of five-hole nozzles, and discussed the different properties of two fuels. They concluded that bio-diesel causes to significantly higher mass flow only if the nozzle design induced large cavitation which extends up to the nozzle outlet section in the case of high needle lift. On the contrary, if the needle lift is small, and the flow is turbulent, diesel fuel results in higher mass flows due to lower frictions.

In the Eularian-Lagrangian approach, the liquid is considered as the carrier/continuum phase in a Eularian frame of reference, whereas vapour bubbles are assumed as the dispersed/discrete phase using a Lagrangian frame of reference by utilizing bubble parcels to model the all of the vapour bubbles. In this approach, the force balance equation is required for the dispersed phase, and another equation is needed to capture the change of bubble size.

Giannidakis *et. al* [26] employed advanced Eularian-Lagrangian model in order to simulate the cavitation for the automotive fuel injector real size nozzles. The model also consisted of bubble-bubble interaction, bubble growth and collapse, bubble turbulent dispersion and hydrodynamic breakup. The model was validated using real size six-hole fuel injector nozzle. The results showed that the transient cavitation behaviour of the side holes induces better atomization compared to center one.

Sou *et. al* [19] also used Eularian-Lagrangian approach by coupling with Large Eddy Simulation (LES) and Rayleigh Plesset (RP) equation, and applied into one side rectangular large scaled nozzle. This study is included in the framework of present thesis to model the cavitation phenomena. Therefore, further information about mathematical equations and findings are given in Chapter 5. The two-fluid models are not widely preferred in the CFD simulations of cavitation phenomena inside fuel injector nozzles due to its high computational cost.

2.3.2 Volume-of-Fluids (VOF)

This method was originally proposed by by Hirt and Nichols [52] and mostly refers to ”volume tracking methods” in the literature. The model assumed that there is a clear and

discontinuous interface between liquid and gas phases, and involved a transport equation based on the liquid volume fraction as indicated below.

$$\frac{\partial(\alpha_L \rho_L)}{\partial t} + \nabla \cdot (\alpha_L \rho_L \mathbf{U}) = 0 \tag{2.1}$$

where $\mathbf{U}$, α_L and ρ_L show mixture velocity, volume fraction and density of liquid, respectively. RHS of equation 2.1 zero refers to no mass transfer between phases.

The exact position of the interface is not known explicitly and therefore special techniques needs to be applied to capture the well-defined interface, and to avoid smearing of the interface as a part of the solution algorithm. Therefore, a scheme called "Compressive Interface Capturing Scheme for Arbitrary Meshes" (CICSAM) developed by Ubbink [53] is used in OpenFOAM® for treatment of the advection term in the transport equation. It should be noted that original VOF method is used to simulate interaction between two immiscible fluids by tracking the interface in each computational mesh spread over the domain.

The original framework of VOF includes the surface tension force term f_σ inside momentum equation, which is calculated per unit volume via Continuum Surface Force (CSF) model in OpenFOAM® as shown below [54].

$$f_\sigma = \sigma \kappa \nabla \alpha_L \tag{2.2}$$

where σ and κ show the surface tension coefficient acting locally at the interface between immiscible fluids and the curvature, whereas $\nabla \alpha_L$ stands for the normal vector at the interface. In the case of constant surface tension coefficient σ, the force originating from surface tension acts in the direction normal to the interface. Therefore, the curvature of the interface can be defined with respect to the divergence of the unit vector to the interface:

$$\kappa = -\nabla \left(\frac{\nabla \alpha_L}{|\nabla \alpha_L|} \right) \tag{2.3}$$

It should be noted that $\nabla \alpha_L$ has a non-zero value only at the interface, indicating a local character of the surface tension term.

The VOF method usually requires the resolution of all involved time and length scales to accurately predict sharp the interface. This causes to have a very fine mesh, and therefore, very high computational cost. Hence, applications of this method to the cavitating flows in real nozzles are still limited [55–57].

2.3.3 Homogeneous Equilibrium Model (HEM)

HEM model treats the cavitating multiphase flows as a single fluid assuming that liquid and gas phases are perfectly mixed in a cell. Hence, only one set of conservation equation for the single mixture phase is solved. The main assumptions for HEM model can be defined as follows:

- The relative velocity between the two phases is negligible compared with the high average flow velocity in the orifice. Therefore, the fluid consists of a mixture of liquid and vapour as single fluid. For this reason, this model is also called as ”single fluid” models in the literature.

- Both phases are assumed to be in thermodynamic equilibrium (The two-phase flow is isothermal), which means that inter-phase heat and mass transfer occur instantaneously.

- Applying these assumptions, the phase change follows an isentropic path; hence the energy equation can be neglected as well.

Ultimately, HEM models computationally cost less time and, therefore, it is widely used in the numerical simulation of cavitation. The most difficult part of this method is to close up the governing equation set. There are various forms depending on how the equation of state and pressure equation are formulated to close the system such as barotropic equation of state and Mass Transfer models including bubble dynamics and semi-analytical approaches.

2.4 Cavitation Models

In the numerical modelling of the cavitation inside injector nozzle, one of the important parts is how to treat the cavitation. In other words, how to model the phase transition among the phases as source term. In this section, models, which have been widely used in the literature for cavitation modelling, are presented. Most of models are defined under the framework of HEM approach, and required an additional equation to close the system of Navier-Stokes equation since the density is an additional parameter.

2.4.1 Barotropic Model

Delannoy and Kueny [58] proposed a barotropic cavitation model, which is based on the compressible homogeneous mixture approach to model growth and collapse of cavitation. The model links to variation of the fluid density ρ in the computational domain respect to pressure variation i.e. $\rho = \rho(P)$. They ignored the viscosity effect (therefore only solved Euler equation) and turbulence model was not considered. They applied model into cavitation inside a Venturi using water and found that predicted detachment frequency is different than experiment.

Schmidt *et al.* [18, 59] also used similar approach with the work of Delannoy and Kueny. They proposed a 2-D transient model to simulate the nozzle flows inside fuel injectors with different geometric parameters. They also took into account the compressibility of both liquid and vapour phases to improve the numerical stability. The sound speed is presented respect to HEM model proposed by Wallis [60], which is also called linear compressibility model in the literature. They found that inlet rounded nozzles leads to produce a much thinner cavitation region compared to sharp edge nozzles.

A very similar model has been also implemented into OpenFOAM® [27] by Karrholm *et al.* [61] and used by many researchers for the cavitation analysis [62–64]. However, this model ignores the turbulence effects, which leads to fail to capture adequately cavitation region and vortical structure. Further explanation about barotropic cavitation model used in OpenFOAM® is given in Chapter 5 due to including inside framework of this thesis.

Additionally, Coutier *et al.* [65] further extended this model by taking into account the viscous and turbulence effects. Other applications of barotropic model can be found in the previous studies [66–69].

2.4.2 Mass Transport Models

Another more precise and applicable approach to model the cavitation in the framework of HEM and to close the system is Mass Transfer Model (MTM). The MTM model uses the governing equations for a perfect gas-liquid mixture often in combination with a transport equation for liquid or gas volume fraction. A mass transfer model is required a source term to evaluate the phase change between liquid and vapour as indicated in the RHS of transport equation 2.4.

$$\frac{\partial(\alpha_L \rho_L)}{\partial t} + \nabla \cdot (\alpha_L \rho_L \mathbf{U}) = R_c + R_e \tag{2.4}$$

where R_c and R_e display rate of mass transfer source terms for condensation and evaporation, respectively.

As explained in the previous section 2.3.2, the standard VOF method is used for capturing the sharp interfaces without phase transition between immiscible fluids. This means that in the equation 2.1, RHS is zero. In order to model the cavitation, the standard VOF method needs to be extended to include the source term due to phase transition. In the framework of present thesis, the source term introduced by Schnerr and Sauer [20] is used.

2.4.2.1 Definition of Simplified VOF / Dispersed VOF

The simplified VOF model proposed by Schnerr and Sauer [20], which is also called dispersed VOF, ignores the surface tension force and does not track the sharp interface between phases. Instead of this, the motion of a certain fluid volume through the computational domain is tracked and phase transition takes place among the phases.

Within the scope of the conventional VOF approach, the two-phase flow is treated as a homogeneous mixture and therefore only one set of equations is used for also simplified VOF. Figure 2.4 shows the schematic sketch of the distribution of the vapour phase and its difference between standard VOF and simplified VOF. In the case of simplified VOF, it is assumed that the vapour bubbles are homogeneously distributed in the computational cell during cavitation, and surface tension force term is ignored.

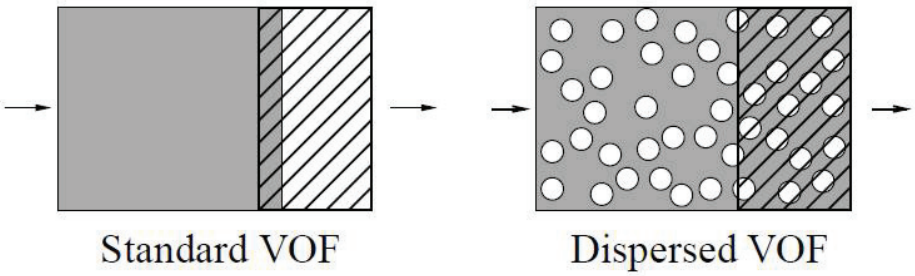

Figure 2.4: Transition from standard VOF application to simplified VOF [20]

Under the framework of simplified VOF model, the difference among the available cavitation models originates from the different treatment of the source terms as indicated in the RHS of the transport equation 2.4. The various cavitation models are introduced and differences are elaborated in the following sections.

2.4.2.2 Schnerr-Sauer Model [20]

This model is based on following assumptions:

- Cavitation phenomena are modelled based on the bubble dynamics, which stands for the growth and collapse of the bubbles.
- The bubbles created by nuclei are assumed already to be existed in the liquid.
- The growth and collapse of the bubbles are depending on the pressure condition.
- The slip between the vapour bubbles and the liquid is ignored.
- From a numerical point of view, the cavitation model predicts the bubble growth, bubble collapse and convection of the vapour phase.
- Non-condensable gas is not taken into account.

In this model, the volume fraction of the vapour α_G is given by

$$\alpha_V = 1 - \alpha_L = \frac{\frac{4}{3}\pi R_b^3 n_0}{1 + \frac{4}{3}\pi R_b^3 n_0} \tag{2.5}$$

where R_b and n_0 denote bubble radius and bubble nuclei number density (the number of nuclei per unit volume), respectively. R_b is represented in terms of n_0 as:

$$R_b = \left[\left(\frac{3\alpha_V}{4\pi(1-\alpha_V)n_0}\right)\right]^{1/3} \tag{2.6}$$

According to Schnerr and Sauer model, bubble growth and collapse are calculated by using Rayleigh (R) equation [70],

$$\frac{dR_b}{dt} = sgn(P_V - P_L)\sqrt{\frac{2\left|P_V - P_L\right|}{3\rho_L}} \tag{2.7}$$

where P_L is the local pressure. Finally, mass transfer rates are given as

$$\begin{aligned} R_e = \quad & -C_v \frac{3\rho_L\rho_V}{\rho_m}\frac{\alpha_L(1-\alpha_L)}{R_b} sgn(P_V - P_L)\sqrt{\frac{2\left|P_V - P_L\right|}{3\rho_L}} \qquad , P_L < P_V \\ R_c = \quad & C_c \frac{3\rho_L\rho_V}{\rho_m}\frac{\alpha_L(1-\alpha_L)}{R_b} sgn(P_V - P_L)\sqrt{\frac{2\left|P_L - P_V\right|}{3\rho_L}} \qquad , P_V < P_L \end{aligned} \tag{2.8}$$

where C_c and C_v are the rate constants for condensation and vaporization, respectively. This model has been already implemented into OpenFOAM® and widely used in the previous studies [57, 71–76]. This model is also included and applied inside the framework of present thesis.

2.4.2.3 Kunz Model [22]

Kunz *et al.* proposed a cavitation model based on the liquid volume fraction α_L by similar sink and source terms, which indicated the mass transfer between liquid and vapour phases with empirical constants. This approach was a semi-analytical model and based on the conservation of mass-momentum around the cavity interface.

The evaporation and condensation source terms in the RHS of the transport equation 2.4 were given in this model as follows.

$$\begin{aligned} R_e &= C_v \frac{\alpha_L \rho_V min[0, P_L - P_V]}{t_\infty (0.5 \rho_L U_\infty^2)} \qquad , P_L < P_V \\ R_c &= C_c \frac{(1-\alpha_L)\alpha^2 \rho_V}{t_\infty} \qquad , P_V < P_L \end{aligned} \tag{2.9}$$

U_∞ and t_∞ show the mean stream velocity and mean flow time scale, respectively. t_∞ is computed as L/U_∞ where L displays the characteristics length scale (which is taken to be the nozzle length in this thesis).

They set the empirical constants C_v and C_L both to be 100. The $k-\varepsilon$ turbulence model was utilised to represent the effect of turbulence with wall functions in their study. They found that the model has a good agreement regarding to pressure results of the hemispherical head form with the experimental data taken for both 2-D and 3-D cases.

They also informed that model is less successful to predict the cone and blunt fore-body head forms because of single phase turbulence modelling. The main shortcoming of this model is to tune the constant parameters subject to the cavitation application. This model is also used under the framework of this thesis and results are presented in the Chapter 5.

2.4.2.4 Merkle Model [25]

Merkle *et al.* also developed a similar pressure-based approach with Kunz's model [22] for the evaporation and condensation rates in order to take into account the mass transfer among the two phases. The general form of the source terms for this cavitation model are given as

$$\begin{aligned} R_e &= C_{dest} \frac{\alpha_L \rho_L min[0, P_L < P_V]}{t_\infty \rho_V (0.5 \rho_L U_\infty^2)} \qquad , P_L < P_V \\ R_c &= C_{prod} \frac{(1-\alpha_L) max[0, P_L < P_V]}{t_\infty (0.5 \rho_L U_\infty^2)} \qquad , P_V < P_L \end{aligned} \tag{2.10}$$

where C_{dest} and C_{prod} indicate the empirical constants, which were set to be $C_{dest} = 1$ and $C_{prod} = 80$ in their study. As a physical explanation of equation 2.10, only the liquid phase can make contribution to vaporization, therefore, only α_L term is seen. This model has been also implemented into OpenFOAM® free software for the cavitation simulation.

2.4.2.5 Singhal Full Cavitation Model [21]

The another approach for the cavitation simulation based on the bubble dynamics was presented by Singhal *et al.*. They included the formation and transportation of the bubbles and the fluctuations of the pressure and velocity.

They additionally took into account the non-condensation gases, which were dissolved and presented in the liquid. In this model, the liquid density is depended of the mass fraction f and the relation is represented by

$$\frac{1}{\rho_L} = \frac{f}{\rho_V} + \frac{1-f}{\rho_L} \tag{2.11}$$

and the vapour volume fraction α_V is given

$$\alpha_V = f\frac{\rho_L}{\rho_V} \tag{2.12}$$

The final form of model includes a mixture of liquid, vapour and non-condensable gas given by

$$\frac{1}{\rho_L} = \frac{f_V}{\rho_V} + \frac{f_G}{\rho_G} + \frac{1-f_V-f_G}{\rho_L} \tag{2.13}$$

where ρ_G shows the non-condensable gas density and it is calculated as:

$$\alpha_L = f_G\frac{\rho_L}{\rho_G} \tag{2.14}$$

liquid volume fraction α_L is calculated as

$$\alpha_V = 1 - \alpha_V - \alpha_G \tag{2.15}$$

The general form of the source terms for this cavitation model are given in terms of vapour mass fraction f_V

$$\begin{aligned} R_e &= C_e\frac{\sqrt{k}}{\sigma}\rho_L\rho_V\left[\frac{2[P_V-P_L]}{\rho_L}\right]^{0.5} - (1-f_V-f_G) \qquad ,P_L < P_V \\ R_c &= C_c\frac{\sqrt{k}}{\sigma}\rho_L\rho_V\left[\frac{2[P_L-P_V]}{\rho_L}\right]^{0.5} f_V \qquad ,P_V < P_L \end{aligned} \tag{2.16}$$

where k and σ stand for turbulent kinetic energy and surface tension, whereas C_e and C_c are model constants, which were set to be 0.02 and 0.01, respectively.

They used the standard Navier-Stokes equations with $k-\varepsilon$ turbulence model. They considered constant density for both vapour and liquid phases. Model was validated using a NACA66 (MOD) hydrofoil, a submerged cylindrical body, and a flow in a sharp-edged nozzle. This model has been also widely used in other previous studies [77–79].

2.4.2.6 Zwart Model [24]

Zwart *et al.* proposed a cavitation model based on the bubble dynamics to predict the total mass transfer rates. They ignored the non-condensable gas and used same R equation to calculate the bubble growth and collapse as indicated in equation 2.7. The general form of the source terms for this cavitation model are given

$$\begin{aligned} R_e &= F_{vap}\frac{3\alpha_{nuc}(1-\alpha_V)\rho_V}{R_b}\sqrt{\frac{2\left|P_L-P_V\right|}{3\rho_L}} \qquad , P_L < P_V \\ R_c &= F_{con}\frac{3n_0\rho_V}{R_b}\sqrt{\frac{2\left|P_L-P_V\right|}{3\rho_L}} \qquad , P_V < P_L \end{aligned} \tag{2.17}$$

where F_{vap} and F_{con} show the constant model parameters, which were set to be 50 and 0.01, whereas R_b was taken as 1 μm. α_{nuc} is the nucleation site volume fraction, which was set to be $5x10^{-4}$.

They validated their model using flow around a hydrofoil with cavitation induced at both the leading edge and mid-chord, and they predicted good results.

2.4.3 Other Cavitation Models

The cavitation models, which have been widely used in the literature, are explained by now. Addition to this, a brief survey about other proposed cavitation models is given in this section.

One of the earliest cavitation model related to the density evolution to the motion of the bubbles was proposed by Kubota *et al.* [80]. Constant bubble number density was considered and their model was governed by Rayleigh Plesset (RP) equation subject to pressure field. This model is also termed "Bubble Two-Phase Flow" (BTF) in literature. They presumed that flow is compressible and viscous whose density changed for cavitation analysis. This model has been used for the prediction of the cavitation around of hydrofoils. Finally, it was reported that this model is appropriate for the applications of large scale,

low Mach number flows, whereas it is not desirable for small scale, high Mach number flows in fuel injector nozzles.

Kato *et al.* [81] suggested a cavitation model by taking into account both inertial and thermal effects to predict the growth of cavitation bubbles. To validate the model, cavitation of cold liquids where the inertial forces are dominated, and boiling, where the thermal effects are dominant, were chosen. However, they found non-physical results in the application of the model into fuel injector nozzle that predicted bubble growth exceeded the radius of nozzle.

Chen *et al.* [82] proposed a pressure based cavitation model, which is based on HEM mixture assumption. They ignored the turbulence model in their model and validated model using the external flows around axisymetric head forms, as well as using the internal flow in sharp edge nozzle. They obtained a good prediction in the case of external flow simulation in terms of cavitation region and pressure distributions. For the flow nozzle application, the model showed a strong Reynolds (Re) number effect, which causes to unsteady, periodic shedding of cavitation at high Re number.

Senocak and Shyy [83] presented a cavitation model, which represented changes in density using a pressure-based approach with a transport equation. They also revised the SIMPLE algorithm to solve the pressure velocity coupling for the turbulent cavitating flow. They used $k - \varepsilon$ turbulence model with wall functions and applied the model over a cylindrical object and an air foil. They were able to capture good prediction that matched with experimental results.

More recently, Srinivasan *et al.* [84] proposed another pressure-based methodology using HEM approach in order to simulate unsteady viscous cavitating flows. Compressibility effect is also taken into account and single fluid Navier-Stokes equations are solved in the model. They further improved this study for the multi-dimensional incompressible flows, and presented a wise model which consisted a novel cavitation induced momentum defect term in the liquid phase momentum equation [85]. They obtained good results which are consistent with the experiments for unsteady cavitation, even though its application to nozzle flows is limited.

2.5 Turbulence Modelling

Since the cavitation flows are turbulent, effects of the turbulence are needed to take into account to accurately model the cavitation phenomena inside fuel injector nozzles.

Turbulence models can be mainly classified into three groups:

- Reynolds Averaged Navier-Stokes (RANS)
- Large Eddy Simulations (LES)
- Direct Numerical Simulations (DNS)

The RANS models apply a Reynolds decomposition technique to the Navier Stokes equations which are time averaged by breaking the velocity down into its mean and fluctuating components. Therefore, main focus is given on the mean flow and the mean flow properties in these models. Since the RANS models requires reasonable CPU time and provides the mean flow prediction, they are widely used in the engineering applications over the last decades.

LES models resolve large scales energy-containing eddies since the momentum, mass, energy and other scalar parameters are affected mostly by large eddies, while the influence on the resolved flow, i.e., mean flow and large eddies, because of smallest and unresolved eddies are modelled by a sub-grid scale model (SGS). Therefore, LES simulations need much more fine mesh, storage and CPU time compared to RANS simulations. Although these disadvantages, the success of the LES approach in capturing the details of small-scale flow structures in cavitating flows and its important role on the cavitation prediction were demonstrated in many previous studies [57, 75, 86–88].

DNS models include resolving the mean flow and all turbulent fluctuations in the turbulent flow. Therefore, Navier-Stokes equations are solved on the sufficiently fine grid and they require much more storage and CPU time compared to RANS and LES models. Hence, applications of these models are limited for the industrial flow computations.

2.6 Summary

In this chapter, a detailed literature survey about cavitation experimental efforts including both large scaled and real size nozzles, and various numerical models for the prediction of the cavitation is presented.

Although, lots of significant information have been obtained from experimental data, there is still confusion and difficulties to predict the pattern of the two mixture phase with turbulence, especially inside real size of fuel injector nozzles. One of the important result obtained from the scaled-up nozzle experiments is that cavitation cannot be scaled up

with regard to nozzle geometry since it has its own length scale in terms of flow field. Nevertheless, observation in experiments with real size nozzles has difficulties due to the reasons which were enumerated on page 5.

On the other hand, it was found that there is an intimate relation between cavitation and turbulence since the nozzle flow is observed highly transient in both scaled-up and actual size nozzles. Previous experimental studies also showed that nozzle geometry, operating conditions and needle position will specify the pattern of the cavitation inside nozzle. It was found that cavitation also can enhance the spray atomization and increase the spray angle.

Experimental studies are so important to provide a useful data for the test and validation of the numerical cavitation models. Therefore, experimental studies need to be carried out quantitatively and qualitatively accurate as much as possible.

With the development of the high performance computers, numerical analysis started to increase and extend. Several advantages, i.e. low cost, speed, detailed information capability in realistic and ideal conditions make the numerical simulation and analysis more attractive with respect to experimental investigations. Therefore, various numerical cavitation models have been proposed in the literature to predict the cavitation phenomena inside fuel injector nozzles, and its effect on the spray atomization.

As discussed before, cavitation is multiphase phenomena (at least two phases, i.e. liquid and gas phases are considered within present thesis) with phase change. Although, most of cavitation models have been used and applied without taking into account the effect of the turbulence modelling, the experimental studies showed that nozzle flow is highly turbulent, and therefore the turbulence effect should be taken into account for more accurate prediction. Therefore, following three points should be carefully specified in order to simulate cavitation accurately.

1. Two phase treatment of the liquid and gas phases
2. Phase change modelling among the phases (as explained in section 2.4, lots of approaches have been proposed to model the source terms)
3. Proper turbulence modelling

As a result, a cavitation model should comprise of a combination of the three different models. Table 2.1 shows the summary of the all the combinations of the models, which are conducted and used inside the framework of present thesis.

Table 2.1: Summary of the combined models used within thesis

	Multiphase Modelling	**Cavitation Modelling**	**Bubble Dynamics**	**Turbulence Model**	**CFD Tool**
1.	HEM	Barotropic	-	RNG $k-\epsilon$	OpenFOAM
2.	Simplified VOF	Kunz	-	RNG $k-\epsilon$	OpenFOAM
3.	Two-Fluids (E-L)	-	RP	LES	In-house code
4.	Simplified VOF	Schnerr-Sauer	MR	RNG $k-\epsilon$	OpenFOAM
5.	Simplified VOF	Schnerr-Sauer	R	RNG $k-\epsilon$	OpenFOAM
6.	Simplified VOF	Schnerr-Sauer	MR	$k-\omega$ SST	OpenFOAM
7.	Simplified VOF	Schnerr-Sauer	MR	LES	OpenFOAM

Chapter 3

Bubble Dynamics Methodology and New Bubble Dynamics Model

3.1 Introduction

This Chapter presents intensive details about the applicability of the existing bubble dynamics models, i.e., the Rayleigh-Plesset (RP) equation and simplified RP equation, which is also called Rayleigh (R) equation, to the prediction of the growth and collapse of cavitation bubbles in a diesel fuel injector nozzle. In addition to that a Modified Rayleigh (MR) equation taking into account the critical pressure P_c is proposed to overcome the drawbacks of the former models. This study includes one of the originality of the present thesis and already published in the international journal of Atomization and Spray [89].

Many researchers have studied the behaviour of bubbles under a wide range of conditions. The first analysis of cavitation based on bubble dynamics was made by Rayleigh [70]. He simplified the behaviour of a single bubble in a liquid by spherical symmetry assumption. This simple work was further improved by Plesset *et al.* and he derived the RP equation, which takes into account the viscous and surface tension effects [90]. Kubota *et al.* [80] and Chen and Heister [82] coupled the RP equation to the computational fluid dynamics (CFD) solver and calculated void fraction in injector nozzles. Although, the RP equation gives one of the good estimations for spherical bubble dynamics, which ignores the bubble–bubble interaction, bubble–wall interaction, bubble deformation, coalescence, and breakup, it requires a tiny time step for good predictions and, therefore, a long computational time.

A simplified form of RP equation, which ignores the viscous, surface tension, non-condensable gas and high-order terms, and it is called Rayleigh (R) equation in the followings, has been widely used in the numerical simulations of cavitation flows to

calculate the bubble growth and collapse. The model enables a robust and quick calculation with a large time step [20,21,23,24,91]. However, R equation may overestimate the bubble radius when pressure around a bubble lies below the vapour saturation pressure and above the critical pressure, and it gives wrong prediction for the bubble collapse speed. Therefore, MR equation based on critical pressure P_C is proposed to satisfy:

- low computational cost by using a large time step,
- voiding a large numerical error using large time steps,
- good estimations of the growth and collapse rates of cavitation bubbles under various pressure conditions.

Since there are few experimental data available on cavitation bubble dynamics, we treated the calculated results by RP equation as the goal for the other bubble dynamics models, whose validity is confirmed by a comparison between calculated and measured single bubble. To examine the applicability of the bubble dynamics models, a large number of calculations have been conducted under wide range of pressure conditions with various time steps. We simulated the radius of spherical cavitation bubbles in water injected at low injection pressure, and that in diesel oil injected at high injection pressure. It should be noted that the effects of turbulent flow field, liquid compressibility, temperature field, bubble coalescence and breakup are ignored.

3.2 Formulation of Bubble Dynamics

The radius of a spherical bubble R_b in an infinite immobile liquid is calculated by Rayleigh-Plesset (RP) equation [90]:

$$R_b \frac{d^2 R_b}{dt^2} + \frac{3}{2}\left(\frac{dR_b}{dt}\right)^2 = \frac{1}{\rho_L}\left(P_b - P_L - \frac{4\mu_L}{R_b}\frac{dR_b}{dt} - \frac{2\sigma}{R_b}\right) \tag{3.1}$$

where R_b, ρ_L, μ_L and σ denote bubble radii, the liquid density, liquid viscosity and the surface tension, respectively. The subscripts L and b represent the liquid and the bubble, in turn. When a liquid containing dissolved gases is submitted to a low pressure, the bubbles are formed [92]. These micro bubbles consist of vapour and non-condensable gases (e.g. oxygen or nitrogen). Figure 3.1 shows a bubble in a liquid in the equilibrium condition. The pressure in a bubble P_b is the sum of the partial pressure P_G of non-condensable gases in a bubble and the vapour saturation pressure P_V, which is higher

than the pressure of the surrounding liquid P_L by the effect of surface tension:

$$P_b = P_G + P_V = P_L + \frac{2\sigma}{R_b} \tag{3.2}$$

This equation indicates that the thermodynamically equilibrium is assumed at the micro-bubble interface, and the total pressure inside the micro-bubble P_b is always larger than the surrounding pressure P_L because of the surface tension.

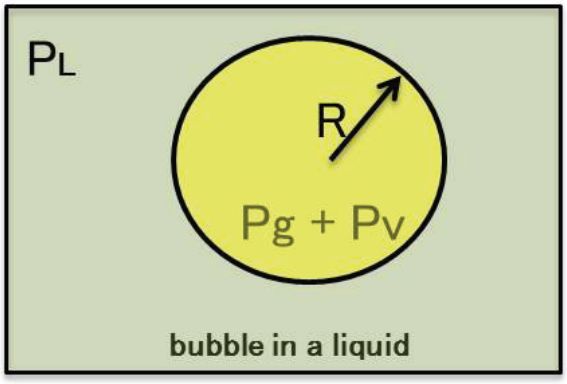

Figure 3.1: Equilibrium condition of a bubble in a liquid

The non-condensable gas pressure P_G is often calculated by considering an isothermal process during the bubble expansion and an adiabatic process for the bubble shrinkage. Initial non-condensable gas pressure P_{G0} can be re-written as follow

$$P_{G0} = P_{L0} + \frac{2\sigma}{R_0} - P_V \tag{3.3}$$

where subscript 0 denotes the initial condition. The pressure and the volume of the gas satisfy the following equations:

$$P|V|^{\gamma} = constant \tag{3.4}$$

$$P_{G0}\left(\frac{4}{3}\pi R_0^3\right)^{\gamma} = P_G\left(\frac{4}{3}\pi R_b^3\right)^{\gamma} \tag{3.5}$$

$$P_G = P_{G0}\left(\frac{R_0}{R_b}\right)^{3\gamma} = \left(P_{L0} + \frac{2\sigma}{R_b} - P_V\right)\left(\frac{R_0}{R_b}\right)^{3\gamma} \tag{3.6}$$

The constant γ is given to be 1 for the isothermal bubble expansion $(dR_b/dt > 0)$, which leads to

$$P_G = P_{G0}\left(\frac{R_0}{R_b}\right)^{3} \tag{3.7}$$

whereas γ is set to be $\gamma = \kappa(= 1.4)$ for the adiabatic bubble shrinkage process $(dR_b/dt < 0)$, which results in

$$P_G = P_{G0}\left(\frac{R_0}{R_b}\right)^{3\kappa} \tag{3.8}$$

Final form of RP equation can be given as follows

$$\rho_L\left[R_b\frac{d^2R_b}{dt^2} + \frac{3}{2}\left(\frac{dR_b}{dt}\right)^2\right] = (P_V - P_L) + P_{G0}\left(\frac{R_0}{R_b}\right)^{3\gamma} - \frac{4\mu_L}{R_b}\frac{dR_b}{dt} - \frac{2\sigma}{R_b} \tag{3.9}$$

R equation is derived by ignoring the high order derivative term, viscous term, surface tension term and the non-condensable gas pressure in RP equation, and given by:

$$\frac{dR_b}{dt} = sgn(P_V - P_L)\sqrt{\frac{2\left|P_V - P_L\right|}{3\rho_L}} \tag{3.10}$$

R equation is a simplified form of the RP equation and has been widely used in the numerical simulations of cavitation flows in diesel injector nozzles due to its simplicity and low computational cost as explained in Chapter 3.1. However, it overestimates bubble radius when pressure lies between the P_V and P_C.

In order to avoid this overestimation while keeping a large time step, a Modified Rayleigh (MR) equation based on the P_C is proposed as follows:

$$\frac{dR_b}{dt} = \begin{cases} sgn(P_C - P_L)\sqrt{\dfrac{2\left|P_V - P_L\right|}{3\rho_L}}, & \text{if } P_L < P_C \quad (3.11a) \\ 0, & \text{if } P_C < P_L < P_V \quad (3.11b) \end{cases}$$

Definition of the critical pressure P_C is given in the next section.

3.2.1 Critical Pressure

If the liquid pressure P_L around a bubble falls below the following pressure threshold, the bubble will start to grow explosively. The pressure threshold is called as critical pressure P_C and demonstrated by [92]

$$P_C = P_V - \frac{4\sigma}{3R_C} \tag{3.12}$$

where R_C is the critical bubble radius and calculated by

$$R_C = R_0\sqrt{\left[3\left(\frac{P_{inj} - P_V}{2\sigma}R_0 + 1\right)\right]} \tag{3.13}$$

where P_{inj} denotes the injection pressure. As seen in equation 3.13, the critical pressure P_C depends on the P_{inj} and the initial radius R_0 of the bubble nuclei. The relationship between P_C and initial nuclei diameter $D_0 = (2R_0)$ is illustrated in Figure 3.2 for a water case with low injection pressure of P_{inj}=0.46 MPa. Noted that the nuclei does not grow at or slightly below P_V but start to grow when $P_L < P_C$. The liquid pressure P_L around an explosively expanding cavity is almost as high as P_V [7, 93].

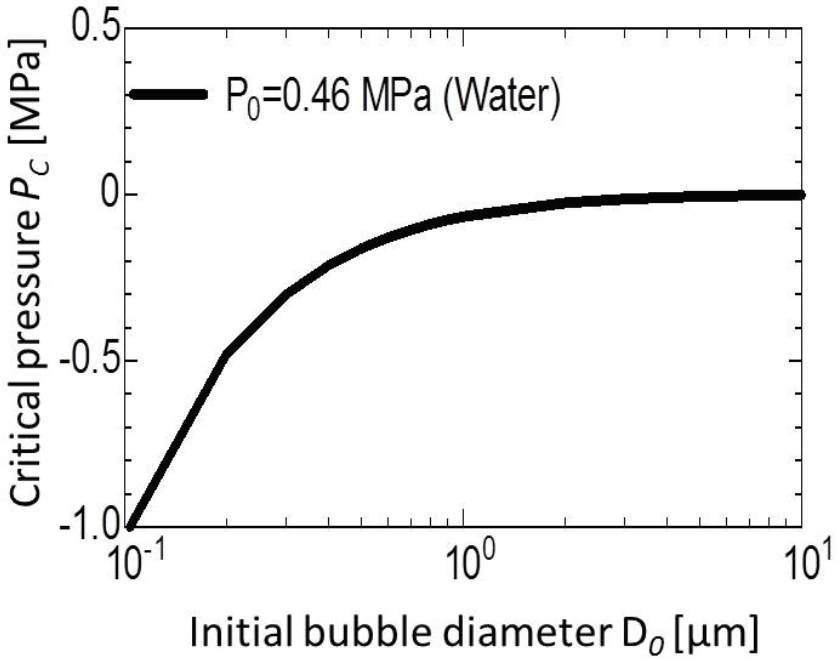

Figure 3.2: Critical pressure P_C variation subject to initial bubble diameter D_0

3.3 Statement of the Problem

In this study, calculations are performed under the following assumptions:

- Bubbles are spherical.
- Liquid compressibility is negligible.
- The pressure inside of the bubble is uniform.
- The gravity and diffusion effects are negligible.
- The vapour and non-condensable gas are the perfect gas.
- The temperatures of the vapour and non-condensable gas are the same.
- The physical properties of gases and liquid are constant

As depicted in Figure 3.3, cavitation bubbles grow in the low-pressure region of the separated boundary layer and the core of vortices [94]. In this study, P_L is assumed to be as high as P_{inj} in the upstream of the nozzle and decreases in the separated boundary layer (or in other words inside recirculation zone) to minimum pressure P_{min}. When the bubble diameter reaches the maximum diameter D_{max}, we let the P_L recover to the equilibrium pressure P_{equ}, which is calculated by equation 3.2. Finally, P_L recovers to the back pressure P_{back} [95].

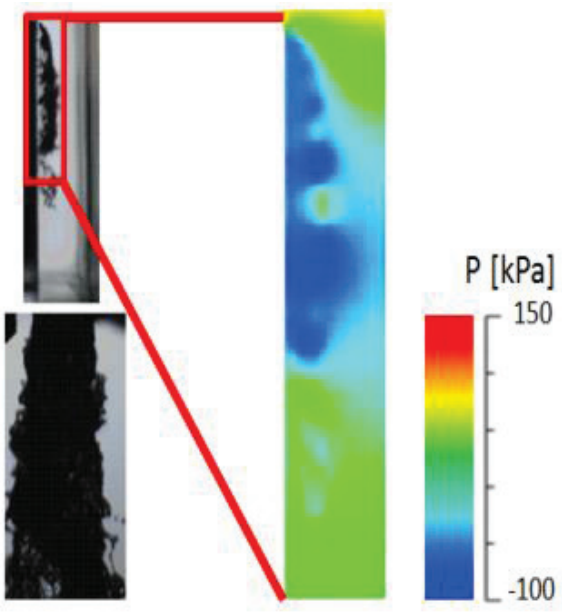

Figure 3.3: Calculated pressure distribution in a nozzle at low injection pressure [94]

In order to simply examine the bubble growth and collapse in the separated boundary layer, two different calculations, i.e. low pressure region when $P_{min} < P_C$ and intermediate pressure region when $P_C < P_{min} < P_V$, are carried out. Figure 3.4 shows the settings for water and diesel oil cases at given P_{inj} and time step Δt.

The case of water injection is carried out in a large scale of nozzle with low P_{inj}, whereas the case of diesel oil in a tiny nozzle and with high P_{inj}. Note that we do not solve pressure and velocity fields but simply varied liquid pressure P_L. The maximum bubble diameter D_{max}, which corresponds to the diameter of the separated boundary layer, is set to be 200, 500 and 1000 μm for the water injection case [95], while it ias set to be 10, 30 and 50 μm for the diesel oil case [96]. When the bubble diameter reached D_{max}, the equilibrium condition is assumed to determine the P_L with respect to equation 3.2.

Three bubble dynamics models such as RP, R and MR equations, are tested under a wide range of calculation conditions as summarized in Table 3.1. Initial bubble diameters

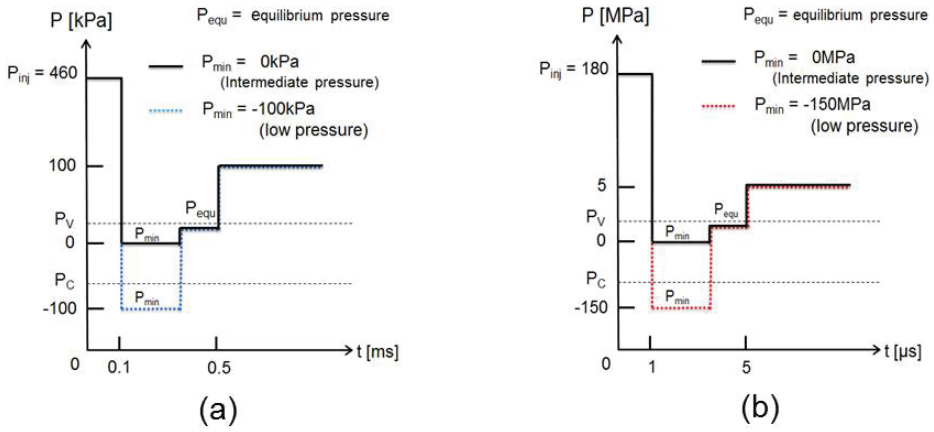

Figure 3.4: Pressure settings for the cases of (a) water and (b) diesel oil injections

D_0 are determined based on P_C and P_{min} using equation 3.13.

Table 3.1: Calculation conditions for water and diesel oil cases

	Low-Pressure Water	**High-Pressure Diesel Oil**
Injection pressure, P_{inj}	460 kPa $(0\text{–}0.1ms)$	180 MPa $(0\text{–}1\mu s)$
Minimum pressure, P_{min} (low and intermediate)	-100, 0 kPa	-150, 0 MPa
Back pressure, P_{back}	10$\backsim$1500 kPa $(0.5 \backsim ms)$	1$\backsim$7 MPa $(0.5 \backsim \mu s)$
Initial bubble diameter, D_0	1 μm, 10 μm	0.001 μm, 0.01 μm
Critical pressure, P_C	-1039 kPa (for $D_0 = 0.1\mu m$) -68 kPa (for $D_0 = 1\mu m$) -0.44 kPa (for $D_0 = 10\mu m$)	-24 MPa (for $D_0 = 0.001\mu m$) -0.94 MPa (for $D_0 = 0.01\mu m$)
Vapour saturation pressure, P_V at 20^0C	2.3 kPa	400 kPa
Maximum bubble diameter, D_{max}	200, 500, 1000 μm	10, 30, 50 μm
Density of liquid, ρ_L	998 kg/m^3	830 kg/m^3
Time step, Δt	$10^{-10} \sim 10^{-6}s$	$10^{-14} \sim 10^{-8}s$

3.4 Numerical Setup

In this study, bubble radius R_b is calculated by simply solving some equations of bubble dynamics under the given pressure conditions. First and second order terms in the equations are discretised as follows:

$$\dot{R}_b = \frac{dR_b}{dt} = \frac{R_b(t) - R_b(t-\Delta t)}{\Delta t} = \frac{R_b^n - R_b^{n-1}}{\Delta t} \tag{3.14}$$

$$\ddot{R}_b = \frac{d^2R_b}{dt^2} = \frac{R_b(t+\Delta t) - 2R_b(t) + R_b(t-\Delta t)}{\Delta t^2} = \frac{R_b^{n+1} - 2R_b^n + R_b^{n-1}}{\Delta t^2} \tag{3.15}$$

where Δt and superscript n show time step and time step number, respectively. The bubble radius at the new time step, which is derived by equation 3.15 and substituted into RP equation 3.1, is determined as follow:

$$R_b^{n+1} = 2R_b^n - R_b^{n-1} - \frac{3}{2R_b^n}(R_b^n - R_b^{n-1})$$

$$+ \frac{\Delta t^2}{\rho_L R_b^n}\left[P_B - P_L - \frac{4\mu}{R_b^n}\left(\frac{R_b^n - R_b^{n-1}}{\Delta t^2}\right) - \frac{2\sigma}{R_b^n}\right] \tag{3.16}$$

The radius at new time step R_b^{n+1} is calculated for R and MR equations,

$$R_b^{n+1} = \left[sgn(P_V - P_L)\sqrt{\frac{2|(P_V - P_L|}{3\rho_L}}\right]\Delta t + R_b^n \tag{3.17}$$

$$R_b^{n+1} = \begin{cases} sgn(P_C - P_L)\sqrt{\dfrac{2\,|P_V - P_L|}{3\rho_L}}\Delta t + R_b^n & \text{if } P_L < P_C \\ 0 & \text{if } P_C \le P_L \le P_V \\ sgn(P_C - P_L)\sqrt{1.27\dfrac{2\,|P_V - P_L|}{3\rho_L}}\Delta t + R_b^n & \text{if } P_V < P_L \end{cases} \tag{3.18}$$

respectively. Note that the growth rate coefficient 2/3 for $P_L < P_C$ is modified to 1.27 for the collapse rate coefficient when $P_V < P_L$, which will be described at the end of this chapter.

3.5 Numerical Results and Discussion

3.5.1 Validation of RP Equation

We treated the calculated bubble dynamics using the RP equation as the goal for the other bubble dynamics models. Therefore, we first examined the validity of the RP equation results through the comparison of measured bubble radius in this section.

Since cavitation bubbles in injector nozzles are formed due to local pressure drop, there is no experiment on bubble size and local pressure. There are a few experimental data available on the time histories of pressure and the radius of bubbles induced by laser [12, 97, 98]. Since the bubble grows not by pressure decrease but by a focused short laser pulse in these experiments, we cannot calculate bubble motion by the R and MR equations.

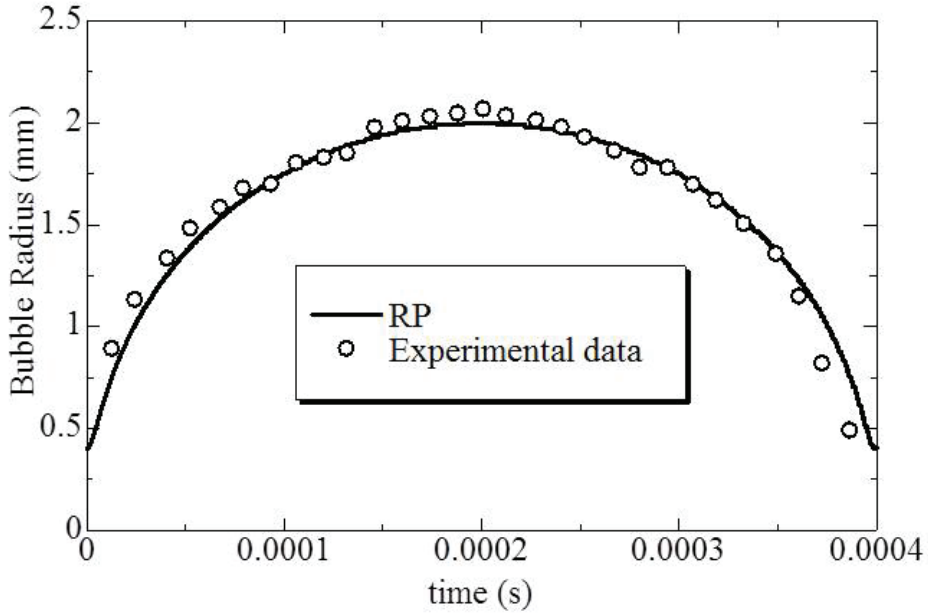

Figure 3.5: Bubble radius measured by Lauterborn and Ohl [12] and calculated by RP equation

We used the experimental data of Lauterborn and Ohl [12] for the validation of the bubble radii calculated by RP equation. For the experimental case, initial radius R_0, P_L and non-condensable gas pressure P_g were given 0.4 mm, 100 kPa and 100 kPa, respectively.

Figure 3.5 displays the comparison of measured and calculated bubble radius by the RP equation. The RP equation gives a good prediction for the growth and collapse of the bubble, which confirms its validity. Further information about the validity of the RP equation can be found in some previous studies [99–101].

3.5.2 Results for Low-Pressure Cases

In this section, bubble radius R_b ias calculated for the water and diesel cases through the low-pressure region where P_L is lower than P_C. Table 3.2 shows the calculation conditions for the low-pressure cases. The minimum pressure P_{min} is set to be -100 kPa and -150 kPa, which are lower than P_C, for water and diesel oil cases, respectively.

Figures 3.6 - 3.9 show calculated bubble diameters using three bubble dynamics models in the case of low minimum pressure for water and diesel oil. The results indicate that a bubble expands drastically as liquid pressure P_L around the bubble drops below the P_C, and then collapse process starts with the recovering of P_L.

The RP equation gives a good prediction for the bubble radius R when time step Δt is small enough. However, the RP equation gives a large error in the cases of larger time steps (e.g. $\Delta t = 10^{-6}s$ for water cases and $\Delta t = 10^{-12} \sim 10^{-10}s$ for diesel oil cases). As seen in Figures 3.6 - 3.9, the R and MR equations give good predictions for the calculated bubble diameter during bubble expansion even with a large Δt.

Table 3.2: Calculation conditions for low minimum pressure cases

	Water	**Diesel Oil**
Injection pressure, P_{inj}	460 kPa $(0\text{–}0.1ms)$	180 MPa $(0\text{–}1\mu s)$
Minimum pressure, P_{min}	-100 kPa (0.1 ms -)	-150 MPa $(1\mu s)$
Initial bubble diameter, D_0	1 μm, 10 μm	0.001 μm, 0.01 μm
Critical pressure, P_C	-68 kPa (for $D_0 = 1\mu m$) -0.44 kPa (for $D_0 = 10\mu m$)	-24 MPa (for $D_0 = 0.001\mu m$) -0.94 MPa (for $D_0 = 0.01\mu m$)
Maximum bubble diameter,D_{max}	500 μm	30 μm
Time step, Δt	$10^{-10} \sim 10^{-6}s$	$10^{-14} \sim 10^{-8}s$

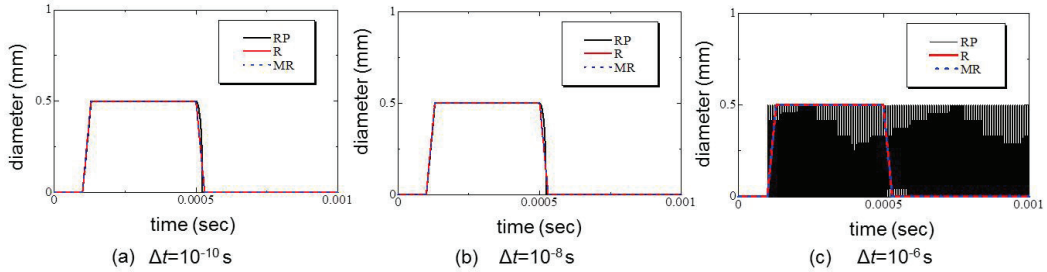

Figure 3.6: Calculated bubble diameter for water injection at low injection pressure ($P_{min} = -100kPa, D_0 = 1\mu m, P_C = -68kPa$)

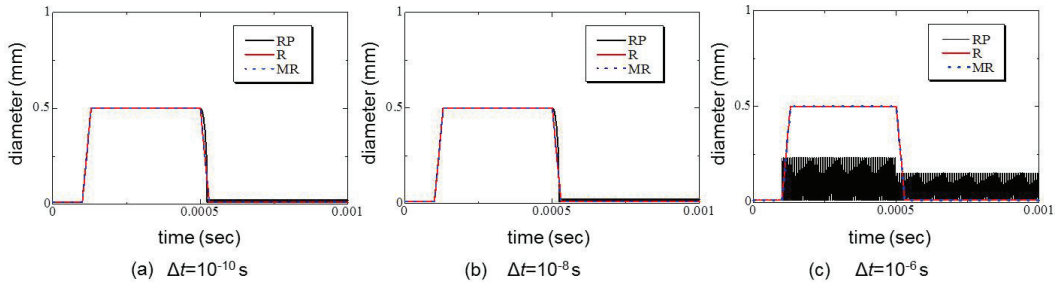

Figure 3.7: Calculated bubble diameter for water injection at low injection pressure ($P_{min} = -100kPa, D_0 = 10\mu m, P_C = -0.44kPa$)

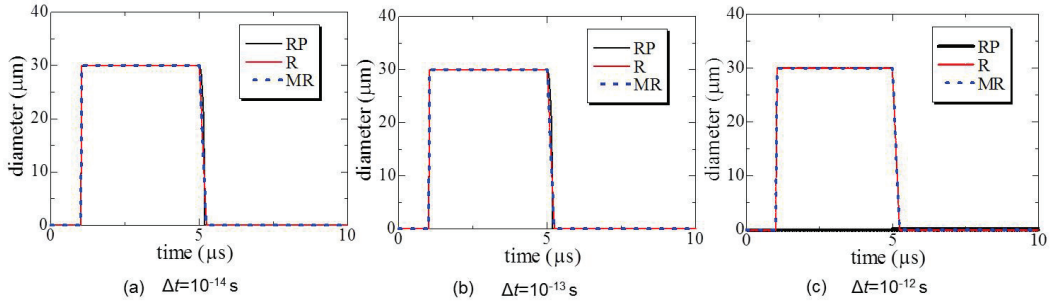

Figure 3.8: Calculated bubble diameter for diesel oil injection at high injection pressure ($P_{min} = -150MPa, D_0 = 0.001\mu m, P_C = -24MPa$)

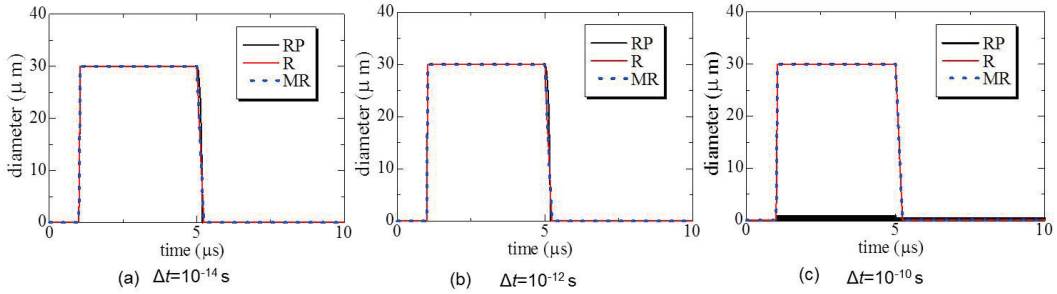

Figure 3.9: Calculated bubble diameter for diesel oil injection at high injection pressure ($P_{min} = -150MPa, D_0 = 0.01\mu m, P_C = -0.94MPa$)

3.5.3 Results for Intermediate Pressure Cases

Table 3.3 shows the calculation conditions of the intermediate minimum pressure. P_{min} is set to be zero, which is higher than the P_C ($P_C < P_{min}$). Since the minimum pressure lies between the vapour pressure and the critical pressure ($P_C < P_{min} < P_V$), it is expected that the bubble growth will not be observed.

Table 3.3: Calculation conditions for intermediate pressure cases

	Water	**Diesel Oil**
Injection pressure, P_{inj}	460 kPa $(0–0.1ms)$	180 MPa $(0–1\mu s)$
Minimum pressure, P_{min}	0	0
Initial bubble diameter, D_0	1 μm	0.001 μm
Critical pressure, P_C	-68 kPa	-24 MPa
Maximum bubble diameter,D_{max}	500 μm	30 μm
Time step, Δt	$10^{-10} \sim 10^{-6} s$	$10^{-14} \sim 10^{-8} s$

Figure 3.10 and 3.11 show the calculated bubble diameter using three bubble dynamics models for water and diesel oil cases, respectively.

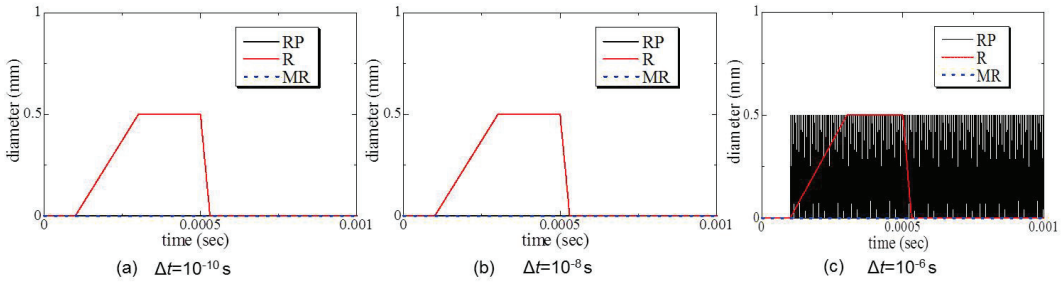

Figure 3.10: Calculated bubble diameter for water injection at low injection pressure ($P_{min} = 0, D_0 = 1\mu m, P_C = -68kPa$)

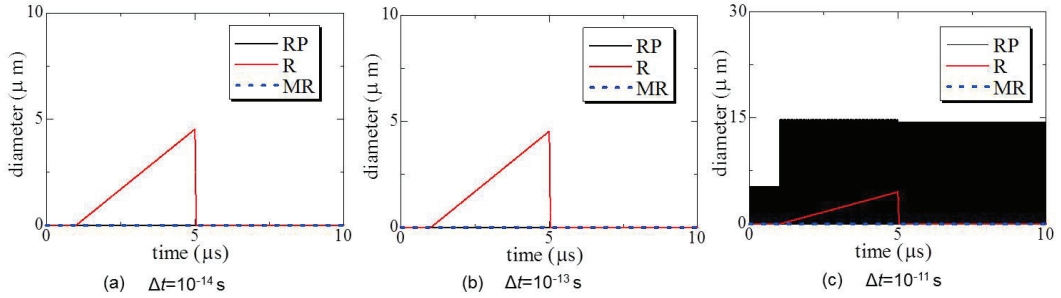

Figure 3.11: Calculated bubble diameter for diesel oil injection at high injection pressure ($P_{min} = 0, D_0 = 0.001\mu m, P_C = -24MPa$)

As seen in the results, R equation gives a large overestimation in bubble diameter, while the RP equation gives error only with small Δt and the MR equation give reasonable predictions for all Δt.

The results shown between Figures 3.6 - 3.11 are summarized in Table 3.4 according to different time steps.

Table 3.4: Summary of the calculations

		Δt (sec)	10^{-10}	10^{-8}	10^{-6}
Low pressure water	$P_C<P_L<P_V$	RP	++	++	--
		R	--	--	--
		MR	+	+	+
	$P_L<P_C$	RP	++	++	--
		R	+	+	+
		MR	+	+	+
		Δt (sec)	10^{-14}	10^{-12}	10^{-10}
High pressure diesel oil	$P_C<P_L<P_V$	RP	++	--	--
		R	--	--	--
		MR	+	+	+
	$P_L<P_C$	RP	++	++	--
		R	+	+	+
		MR	+	+	+

++ : excellent , + : good, -- : bad

3.5.4 Bubble Growth and Collapse Rates

In order to quantitatively evaluate the accuracy of the bubble dynamics models, comparisons of the mean growth and collapse rates dD_b/dt of a bubble are performed among the RP, R, and MR models. The mean growth and collapse rates are calculated according to

$$\frac{dD_b}{dt} = \frac{D_{max} - D_0}{\delta t} \tag{3.19}$$

$$\frac{dD_b}{dt} = \frac{D_{final} - D_{max}}{\delta t} \tag{3.20}$$

where D_{max}, D_0, D_{final} and δt are the maximum, initial and final diameters of bubble and duration, respectively. The definitions of the mean growth and collapse rates are illustrated

schematically in Figure 3.12.

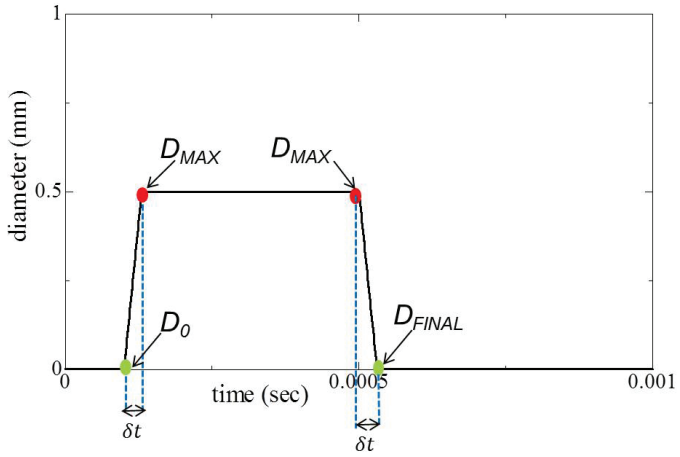

Figure 3.12: Definitions of the mean growth and collapse rates of a bubble

Figure 3.13(a) and 3.13(b) show calculated mean growth rates dD_b/dt of a bubble for water at low P_{inj} ($D_0 = 1\mu m$, $P_C = -68kPa$) and diesel oil at high P_{inj} ($D_0 = 0.001\mu m, P_C = -24MPa$), respectively. As obtained, the R and MR equations give almost the same mean growth rates with the RP equation when $P_{min} < P_C$, whereas the R equation overestimates the mean growth rate and MR equation gives good prediction when $P_C < P_{min} < P_V$.

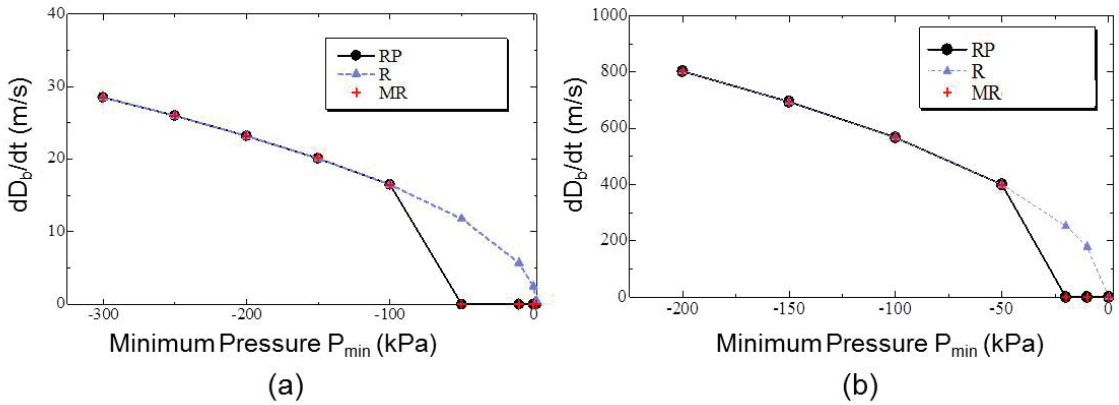

Figure 3.13: Mean growth rates for the cases of (a) water and (b) diesel oil injections

Some of the previous studies stated that the prediction of the cavitation bubbles while collapsing is difficult due to its extremely high speed collapse [92, 102, 103]. Figure 3.14(a) and 3.14(b) indicate the mean collapse rate dD_b/dt for water at low injection pressure P_{inj} ($D_0 = 1\mu m$, $P_C = -68kPa$) and diesel oil at high injection pressure P_{inj} ($D_0 = 0.001\mu m$, $P_C = -24MPa$), respectively. As seen in the results, the MR and R equations overestimate dD_b/dt during the the collapse process. This overestimation also can be

seen in Figure 3.15, which displays differences in bubble diameter calculated by RP, MR and R equations for water ($D_0 = 1\mu m, P_{min} = -100kPa, \Delta t = 10^{-10}s$) and diesel oil ($D_0 = 0.001\mu m, P_{min} = -150MPa, \Delta t = 10^{-13}s$), respectively.

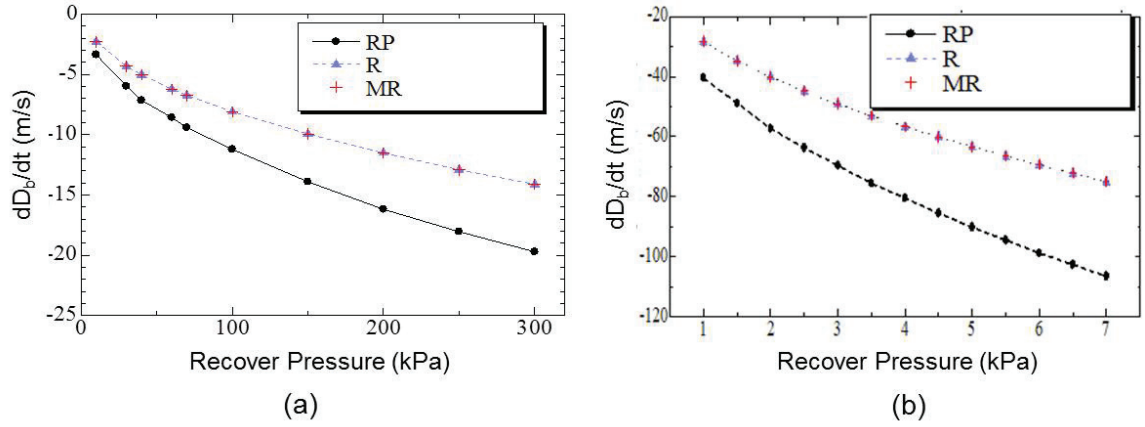

Figure 3.14: Mean collapse rates for the cases of (a) water and (b) diesel oil injections

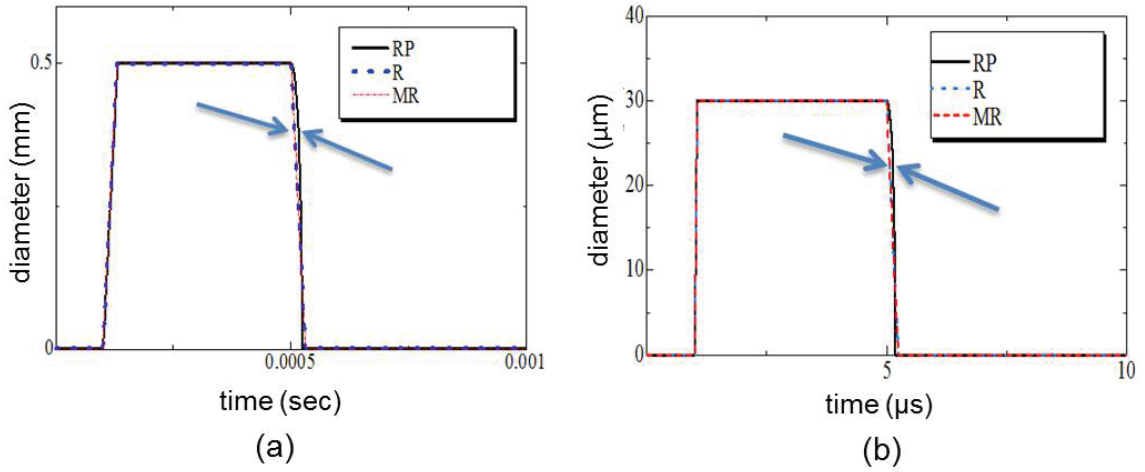

Figure 3.15: Growth and collapse rates for (a) water and (b) diesel oil injections

Difference in calculated collapse rates dD_b/dt by RP equation and other models is clearly illustrated in Figure 3.16 with various D_{max} (=200, 500 and 1000 μm). Addition to this, effect of the surface tension into collapse rate is calculated using following equation:

$$\frac{dR_b}{dt} = sgn\left(P_C - P_L - \frac{2\sigma}{R_b}\right)\sqrt{\frac{2}{3\rho_L}\left|P_C - P_L - \frac{2\sigma}{R_b}\right|} \tag{3.21}$$

where σ is the surface tension. Figure 3.17(a) and 3.17(b) show the effect of the surface tension on collapse rate dD_b/dt calculated with three models for water and diesel oil cases. As obtained, the surface tension term does not affect collapse rate since the pressure term is more dominant than surface tension in equation 3.21. Therefore, its effect is ignorable.

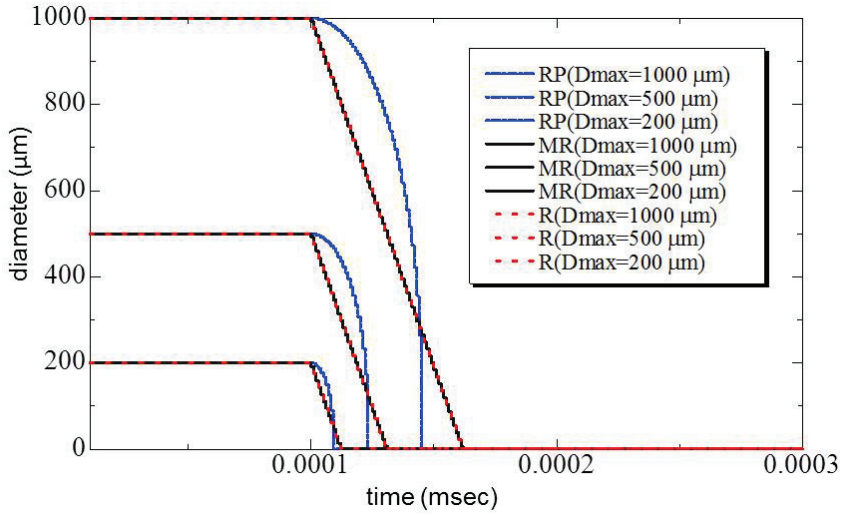

Figure 3.16: Collapse rates of a bubble

Finally, in order to estimate the collapse rate of the bubble properly, as does the RP equation, we propose following equation for collapse ($dR_b/dt < 0$) as well.

$$\frac{dR_b}{dt} = sgn(P_C - P_L)\sqrt{\left(1.27\frac{|P_V - P_L|}{\rho_L}\right)} \tag{3.22}$$

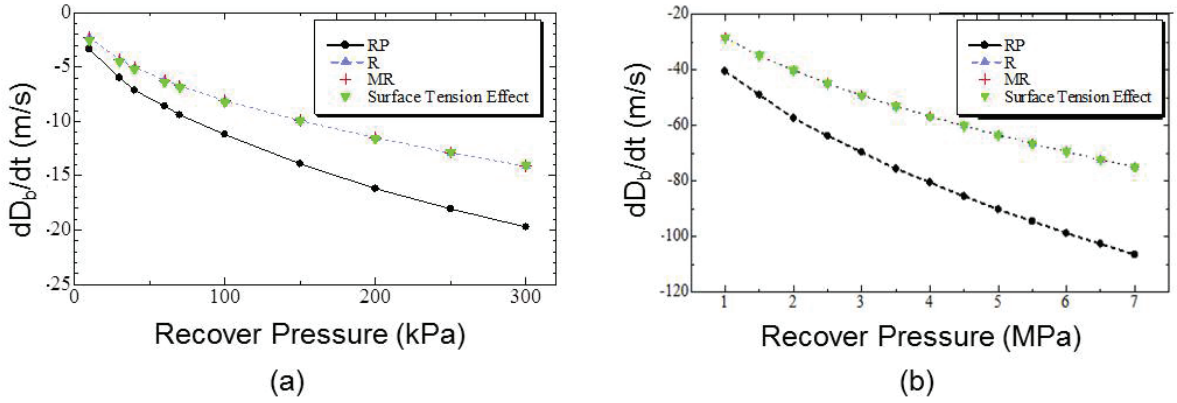

Figure 3.17: Effect of surface tension on collapse rate for (a) water and (b) diesel oil cases

Figure 3.18(a) and 3.18(b) display the mean collapse rate for water and diesel oil, where $D_0 = 0.001\mu m, P_C = -24kPa, D_{max} = 30\mu m$ and $D_0 = 1\mu m, P_C = -68kPa, D_{max} = 500\mu m$, respectively. These results indicate that the MR equation with modified coefficient for collapse gives good predictions for the mean collapse rate.

Figure 3.19 shows the results of collapse rate calculated by RP and MR equations with the modified coefficient for the diesel oil case with different D_{max} 10 and 50 μm. As seen in this results, MR results agree well with RP equation with a small error.

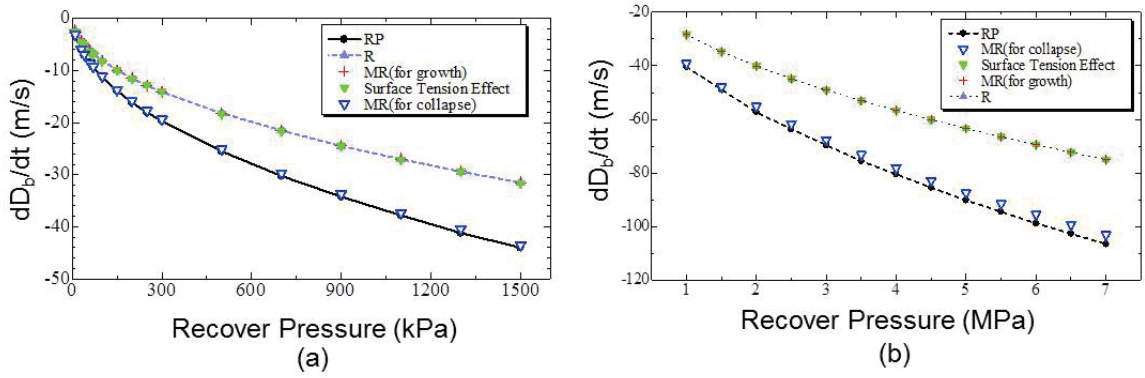

Figure 3.18: Collapse rate with modified coefficient for (a) water and (b) diesel oil cases

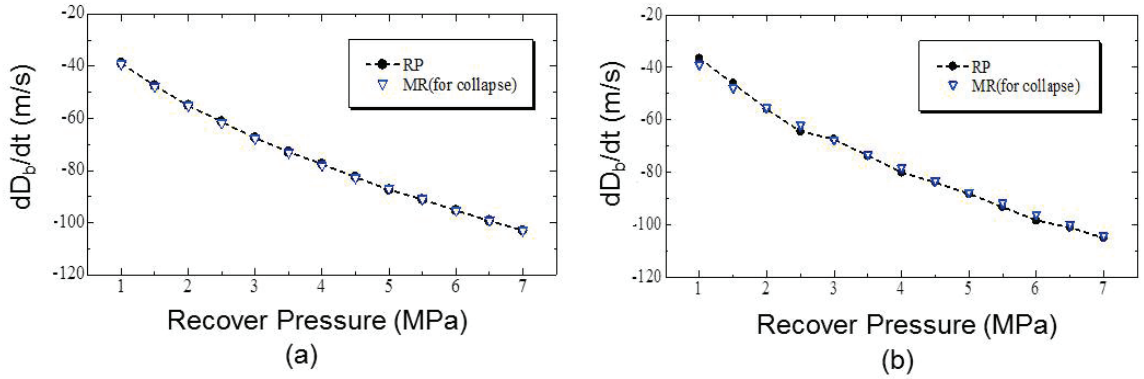

Figure 3.19: Collapse rate of diesel oil case at various recover pressure for (a) $D_{max} = 10\mu m$ and (b) $D_{max} = 50\mu m$

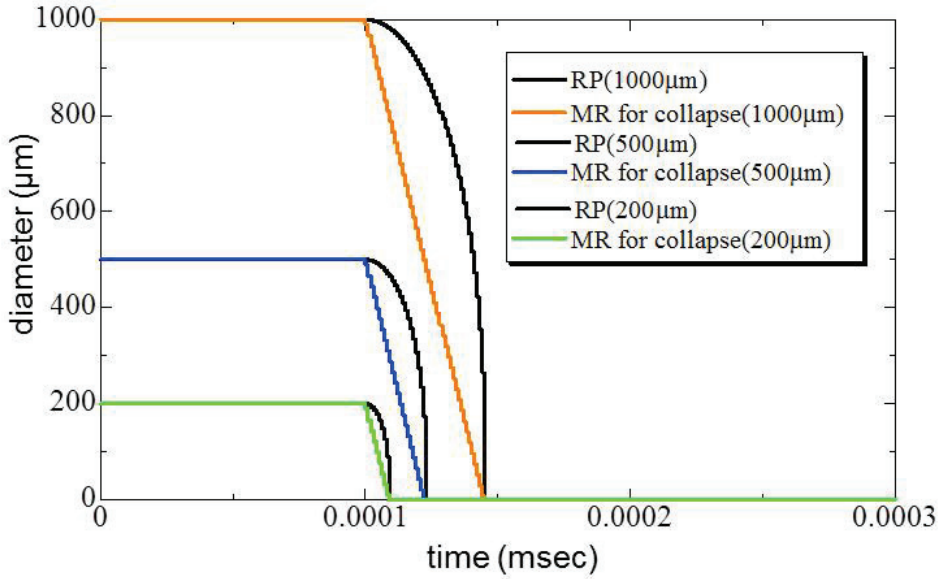

Figure 3.20: Collapse rates calculated by RP and MR (with modified coefficient)

Figure 3.20 shows time histories of collapse rate calculated by RP equation and MR equation (with modified coefficient) for water case with different D_{max}, such as 200,

500 and 1000 μm. The results indicate that MR model is able to give good prediction when compared with RP equation. It should be noted that RP gives non-linear collapse distribution while MR with the modified coefficient predicts linear collapse.

As a result, the general form of MR equation for bubble growth and collapse can be summarized as follows:

$$\frac{dR_b}{dt} = sgn(P_C - P_L)\sqrt{c\left|\frac{P_V - P_L}{\rho_L}\right|} \tag{3.23}$$

where

$$c = \begin{cases} 2/3 & \text{, if } P_L < P_C, \\ 0 & \text{, if } P_C \leq P_L \leq P_V, \\ 1.27 & \text{, if } P_V < P_L. \end{cases} \tag{3.24}$$

3.6 Summary

In this section, the applicability of various bubble dynamics models to predict the growth and collapse of cavitation bubbles in fuel injectors were examined under various pressure conditions for water and diesel oil cases. A modified Rayleigh (MR) equation based on the critical pressure is proposed and its validity is examined through RP equation. The important result can be summarized as follows:

- The Rayleigh–Plesset (RP) equation gives a good prediction for the radius of a spherical bubble without bubble–bubble interaction, bubble–wall interaction, bubble deformation, coalescence, and breakup, only when the time step Δt is enough small.

- When the pressure P_L around of bubble is lower than the critical pressure P_C ($P_L < P_C$), R and MR equations give identical results with a large Δt for the estimation of the bubble growth as provided by RP equation. However, when P_L lies between P_C and P_V ($P_C < P_L < P_V$), the R equation overestimates the bubble growth rate, where MR equation gives a good prediction for the bubble diameter at a wide range of pressure with a large time step Δt.

- The R equation is also not valid in the case of bubble collapse since its predictions always tend to overestimate, whereas the MR equation gives a small error in bubble collapse rate, which was reduced by modifying the collapse rate coefficient.

- Another finding of this study is that the effects of surface tension and non-condensable gases on cavitation in fuel injectors are negligible.

Chapter 4

Experimental Equipment

4.1 Introduction

This section first presents the experimental setup and results, which are used for the validation of the numerical findings. For this experiment, one-side rectangular large scale acrylic nozzle is employed.

4.2 Experimental Setup

4.2.1 Experimental Apparatus

Figure 4.1 shows the schematics of the experimental apparatus. Filtered tap water is discharged through a rectangular nozzle into ambient air by a plunger pump. Liquid flow rate is measured using a flow meter.

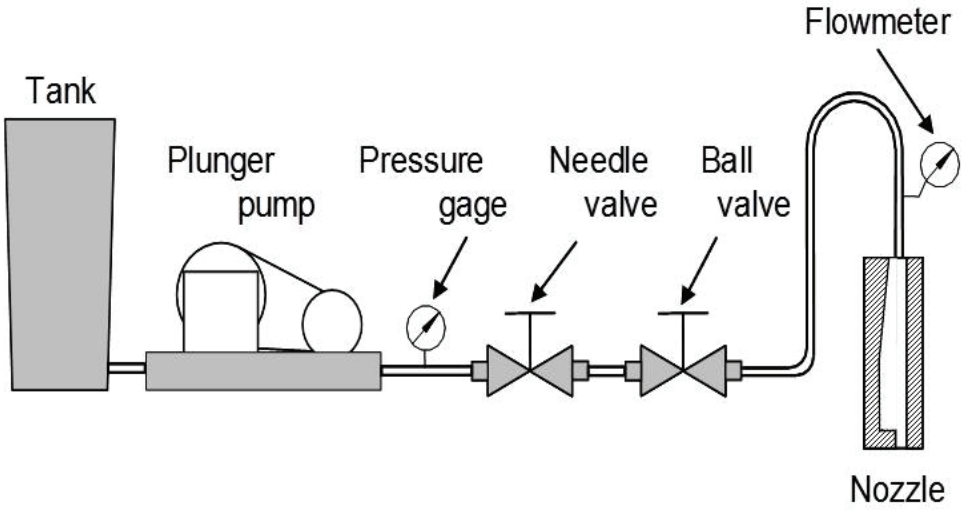

Figure 4.1: Experimental apparatus

Geometry of the rectangular nozzle is given in Figure 4.2. The width W_n, length L_n and thickness t of the nozzle are about 2, 8 and 2 mm, respectively.

The side walls are made of stainless steel thin flat plates, by which a sharp edge was formed at the inlet of the nozzle. The front and back walls are transparent acrylic flat plates for visualization and LDV measurement. In order to decrease the number of computational cells, the width of the upstream region W_u of the nozzle is only four times as wide as the nozzle width W_n, and there is no inlet edge on the right side. Hence, cavitation occurs only along the left wall.

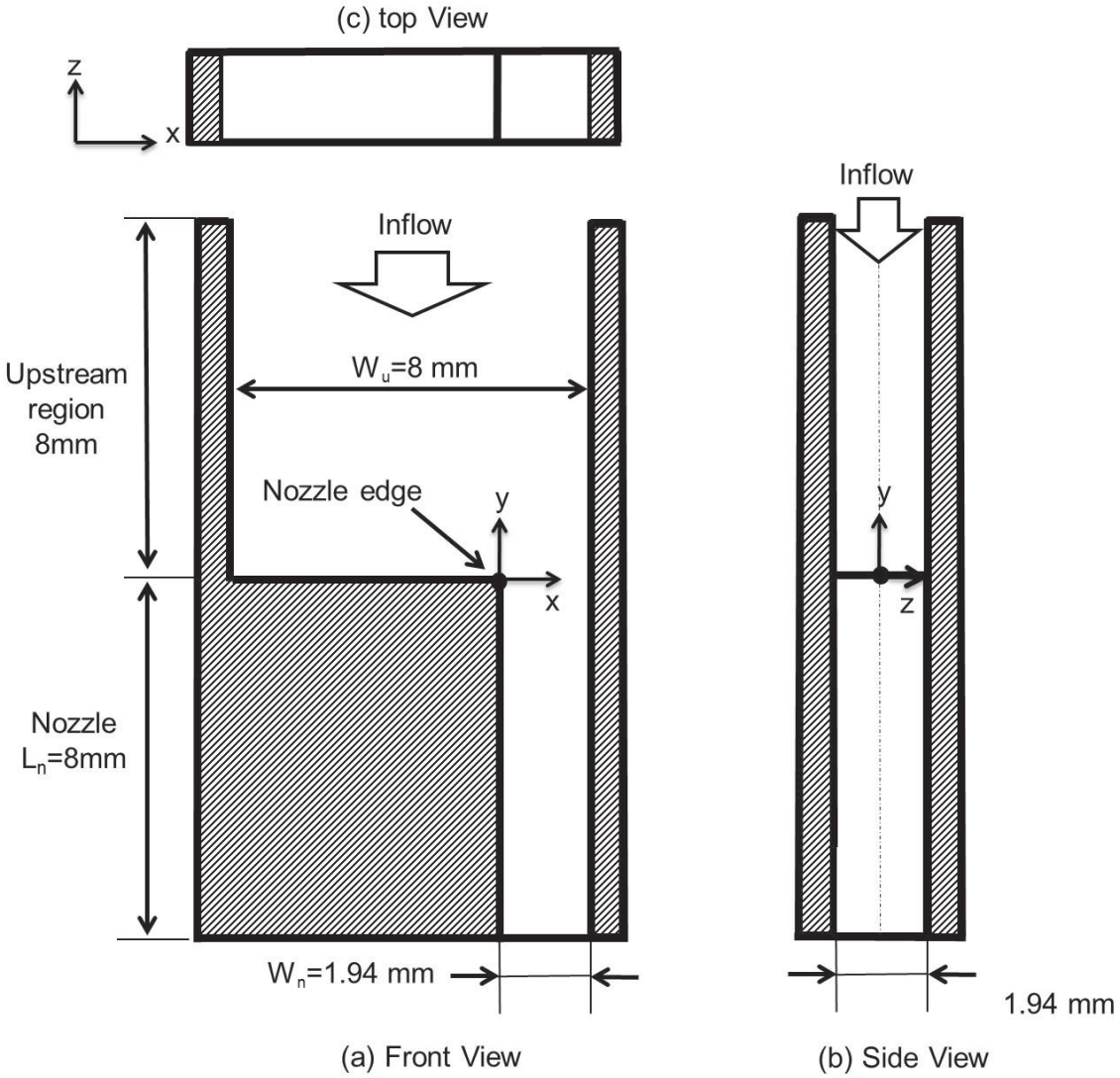

Figure 4.2: Nozzle geometry

The concentration of oxygen dissolved in the water is measured using a dissolved oxygen probe (Hach company, $HQ30d$) and is about 9 mg/L. Still images of cavitation and a liquid jet are taken by using a digital camera (Nikon, $D70,3,008x2000$ pixels) and a flash lamp (Nissin Electronic, $MS-1000$ and $LH-15M$, duration=4μs). Time evolution of cavitation is captured using a high speed digital video camera (Redlake, Motion Pro

$HS-1$, frame rate = 20,000 fps, exposure time=50μs) and a reflector lamp (Panasonic, $PRF-500$).

Turbulent liquid velocity inside the rectangular one-side acrylic nozzle was measured using an LDV system (DANTEC, $60X$ series) at the middle plane in depth of the nozzle channel.

The measurement could not be carried out unless silicon carbide (SiC) particles of 3 μm in mean diameter are added as seeding particles (2.5 g/m^3). Note that the effects of the added seeding particles on cavitation are negligible. This assumption is based on the comparison of the dimensionless cavitation length L^*_{cav}, which is described as the ratio of the mean streamwise length of the cavitation zone L_{cav} to the nozzle length L_n, under the constant injection pressure differences with and without seeding particles as explained in our previous study [6]. According the result, the increase in L^*_{cav} due to seeding particles was less than $\%8$. Hence, the effect of the seeding particles is ignored in this experiment. Further information on experimental setup is described in previous study [6].

4.2.2 Cavitation in Nozzle and Liquid Jet

Experimental conditions are shown in Table 4.1 in details. The two important non-dimensional numbers, which are used to characterize the turbulent cavitating flows, are cavitation number K and the liquid Reynolds number Re_n, and defined by

$$K = \frac{P_a - P_V}{0.5\rho_L V_n^2} \tag{4.1}$$

$$Re_n = \frac{V_n W_n}{\nu_L} \tag{4.2}$$

where P_a, P_V and V_n show the atmospheric pressure, vapour saturation pressure and mean liquid velocity in the nozzle, respectively. ν_L is liquid kinematic viscosity.

Photos of cavitation in the nozzle and a liquid jet near the nozzle are shown in Figure 4.3. Cavitation inside of nozzle and jets are observed as dark colour due to having wavy interface. No cavitation bubble is observed for 0.14 MPa injection pressure P_{inj} and 10.1 m/s in mean liquid velocity V_n in the nozzle.

$V_n = 12.8\ m/s$ ($P_{inj} = 0.22\ MPa$) shows the developing of the cavitation from the entrance of the nozzle due to the number of appearing cavitation bubbles.

For $V_n = 15.4\ m/s$ ($P_{inj} = 0.28\ MPa$), a cavitation sheet is formed and cavitation

extends almost to the exit, which induces a large jet deformation and droplet formation even in the vicinity of the nozzle.

For $V_n > 16.5\ m/s$ ($P_{inj} > 0.31\ MPa$), hydraulic flip is formed, in which the reattachment of the separated boundary layer does not occur within a nozzle and the liquid jet deformation is suppressed.

Table 4.1: Experimental Conditions

Injector pressure, P_{in} [MPa]	mean liquid velocity, V_n [m/s]	Cavitation number, K	Reynolds number, Re_n	Flow rate, Q [ml/s]	Cavitation regime	liquid jet
0.15	10.1	1.92	21900	38	no cavitation	wavy jet
0.16	10.6	1.74	23100	40	developing cavitation	wavy jet
0.22	12.8	1.19	27700	48		
0.25	14.4	0.94	31200	54		
0.28	15.4	0.82	33500	58	super cavitation	spray
0.31	16.5	0.71	35800	62	hydraulic flip	flipping jet

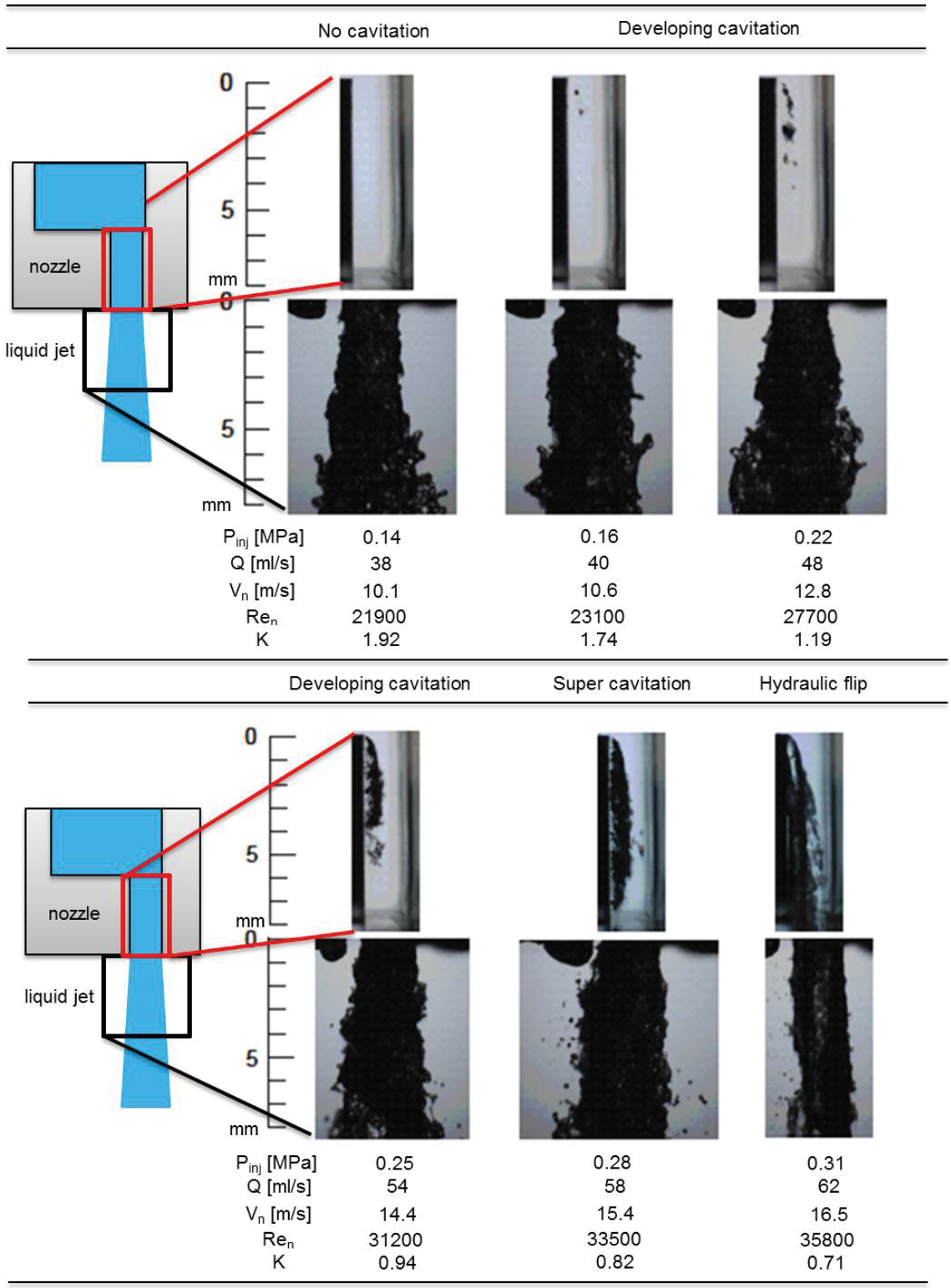

Figure 4.3: Cavitation in the rectangular nozzle and liquid jet

Chapter 5

Applicability of Previous Cavitation Models other than Bubble Dynamics Method

5.1 Introduction

In this Chapter, the applicability of the different cavitation models, such as barotropic model [58] and Kunz's cavitation model [22], to turbulent cavitating flows in a fuel injector nozzle are presented. Both models ignore the bubble dynamics approach. OpenFOAM is used for the numerical simulation of turbulent cavitation flows and turbulent effect is taken into account using RNG $k-\epsilon$, which is known to applicable to the flow with separation and reattachment. Table 5.1 shows the summary of the combined models used within this chapter.

Table 5.1: Summary of the combined models

	Multiphase Modelling	**Cavitation Modelling**	**Bubble Dynamics**	**Turbulence Model**	**CFD Tool**
1.	HEM	Barotropic	-	RNG $k-\epsilon$	OpenFOAM
2.	Simplified VOF	Kunz	-	RNG $k-\epsilon$	OpenFOAM

Numerical results are validated with the experimental data, whose results are presented in Chapter 4, in terms of cavitation length, thickness and cavitation cloud shedding in an one-side rectangular nozzle. The motion of transient cavitation and turbulent velocity in a rectangular nozzle were acquired by using a high speed camera and Laser

Doppler Velocimetry (LDV), which are useful for a quantitative verification of turbulent cavitation flow models.

5.2 Model Equations

5.2.1 Barotropic Model

A barotropic cavitation model with the combination of Homogeneous equilibrium model (HEM) and a RANS turbulence model are used for simulation of the cavitation flow. It is assumed that liquid and vapour phases are perfectly mixed in each cell and the compressibility of the two-phase mixture is taken into account in the calculations. To calculate the cavitation, a common barotropic equation of state proposed by Dellanoy and Kueny [58], which describes the relation between the pressure and density as a closure equation, is employed in the form of the following equation:

$$\frac{D\rho_m}{Dt} = \Psi \frac{DP}{Dt} \tag{5.1}$$

where t and P show time and pressure, respectively. Ψ refers to the compressibility of the mixture phase, and corresponds to the inverse of the speed a of sound squared:

$$\Psi = \frac{1}{a^2} \tag{5.2}$$

This equation can be operated directly in the continuity equation to formulate a pressure equation or integrated to obtain the pressure as a function of the density. The latter approach was conducted by Schmidt *et al.* [18]. The equation of state should be compatible with the liquid and vapour equations of the state both at the limits when there is pure liquid and pure vapour, and also when there is a mixture of them. Both cases can be explained by a linear equation of state:

$$\rho_V = \Psi_V P \tag{5.3}$$

$$\rho_L = \rho_L^0 + \Psi_L P \tag{5.4}$$

where Ψ_L, Ψ_V and ρ_L^0 show liquid and vapour compressibilities, and the liquid density at given temperature, which is represented by

$$\rho_L^0 = \rho_{L,sat} - \Psi_L P_{sat} \tag{5.5}$$

where $\rho_{L,sat}$ and P_{sat} demonstrate liquid density and pressure at saturation, in turn. The volume fraction of vapour in the mixture phase is defined by α_V,

$$\alpha_V = \frac{\rho_m - \rho_{L,sat}}{\rho_{V,sat} - \rho_{L,sat}} \tag{5.6}$$

where the vapour density at saturation $\rho_{V,sat}$ is calculated by

$$\rho_{V,sat} = \Psi_V P_{sat} \tag{5.7}$$

There is no cavitation if α_V is 0, whereas a cell is fully occupied by cavitation if α_V is 1. The mixture density ρ_m is given as follows [61];

$$\rho = (1-\alpha_V)\rho_L^0 + [\alpha_V \Psi_V (1-\alpha_V)\Psi_L]P_{sat} + \Psi(P - P_{sat}) \tag{5.8}$$

The compressibility Ψ is modelled using Wallis linear model [60] as follow,

$$\Psi = \alpha_V \Psi_V + (1-\alpha_V)\Psi_L \tag{5.9}$$

The mixture's molecular viscosity μ_m is given by:

$$\mu_m = \alpha_V \mu_V + (1-\alpha_V)\mu_L \tag{5.10}$$

where μ_L and μ_V show pure liquid and pure vapour dynamic viscosities, respectively.

In this study, OpenFOAM platform is used, under the name of cavitatingFoam [27]. The methodology of the cavitatingFoam solver starts by solving the continuity equation for ρ_m:

$$\frac{\partial \rho_m}{\partial t} + \nabla \cdot (\rho_m \mathbf{U}) = 0 \tag{5.11}$$

where $\mathbf{U}$ denotes the mixture velocity. Then, calculated value of ρ_m is used to attain preliminary values for α_V (in Equation 5.6) and Ψ (in Equation 5.9), and solving the momentum equation

$$\frac{\partial \rho_m \mathbf{U}}{\partial t} + \nabla \cdot (\rho_m \mathbf{U}\mathbf{U}) = -\nabla P + \nabla \cdot [\mu_{eff}(\nabla \mathbf{U} + (\nabla \mathbf{U})^T)] \tag{5.12}$$

where the effective viscosity μ_{eff} is given by

$$\mu_{eff} = \mu_m + \mu_t \tag{5.13}$$

where μ_m and μ_t denote the molecular and turbulence viscosities. The latter is modelled

by one of the RANS turbulence model such as RNG $k-\epsilon$ model.

An iterative PISO algorithm is employed to solve P and correct the velocity $\mathbf{U}$ to achieve continuity. The continuity equation used in the PISO loop is transformed into a pressure equation by using the Equation 5.8 as follows.

$$\frac{\partial(\Psi P)}{\partial t} - [\rho_L^0 + (\Psi_L - \Psi_V)P_{sat}]\frac{\partial \Psi}{\partial t} - P_{sat}\frac{\partial \Psi}{\partial t} + \nabla \cdot (\rho_m \mathbf{U}) = 0 \tag{5.14}$$

When the continuity is satisfied, the values of the properties ρ_m, α_V and Ψ are updated via Equations 5.8, 5.6 and 5.9, respectively. Then, these are used to solve momentum Equation 5.12 again. The algorithm is repeating until the convergence is achieved.

In the numerical calculations, the advections terms are discretised by using a total variation diminishing (TVD) scheme named limited linear [104].

The time step Δt is limited by the Courant number Co and the acoustic Courant number $Co_{acoustic}$ defined as:

$$Co = max\left(\frac{|U|}{\Delta x}\right)\Delta t \tag{5.15}$$

$$Co_{acoustic} = max\left(\frac{1}{\sqrt{\Psi}\Delta x}\right)\Delta t \tag{5.16}$$

where Δx is the cell size in the direction of the velocity. The Courant number is set to be 0.125, while the acoustic Courant number is limited to 12.5. Both values have been set according to their effects on the results accuracy and also by taking into account the computational cost. Time step Δt is set to be 10^{-8} s.

5.2.2 Kunz's Model

Kunz *et al.* [22] proposed a cavitation model based on the liquid volume fraction α_L by similar sink and source terms, which indicates the mass transfer between liquid and vapour phases with empirical constants. This approach is a semi-analytical model, which is based on the conservation of mass-momentum around the cavity interface, and is coupled with Mass Transfer Model by solving following transport equation of liquid,

$$\frac{\partial(\alpha_L \rho_L)}{\partial t} + \nabla \cdot (\alpha_L \rho_L \mathbf{U}) = R_c + R_e \tag{5.17}$$

where R_c and R_e display rate of mass transfer source terms for condensation and evaporation, respectively.

The evaporation and condensation source terms are given in this model as follows.

$$R_e = C_v \frac{\alpha_L \rho_V min[0, P_L - P_V]}{t_\infty (0.5 \rho_L U_\infty^2)} \qquad , P_L < P_V$$
$$R_c = C_c \frac{(1-\alpha_L)\alpha_L^2 \rho_V}{t_\infty} \qquad , P_V < P_L \tag{5.18}$$

U_∞ and t_∞ show the mean stream velocity and mean flow time scale, respectively. t_∞ is computed as L/U_∞, where L displays characteristics length scale (which is set to be the nozzle length in this thesis). In the original model, the empirical constants C_v and C_L are both set to be 100. These constants are used to distinguish between vaporization and condensation in order to enhance the predictive accuracy.

The mixture density ρ_m and viscosity μ_m are calculated based on the volume fraction of the liquid phase as follows

$$\rho_m = (1-\alpha_L)\rho_V + \alpha_L \rho_L \tag{5.19}$$

$$\mu_m = (1-\alpha_L)\mu_V + \alpha_L \mu_L \tag{5.20}$$

Turbulence effects are taken into account using RNG $k-\epsilon$ model. An iterative PIMPLE algorithm is employed to solve P and correct the mixture velocity **U**. Time step Δt and the maximum Courant number are set to be 10^{-8} s and 0.1, respectively.

5.3 Mesh Description and Flow Conditions

It is well know that the results of the CFD calculations are affected by the computational mesh, especially in the regions of the high velocity gradients. Therefore, the mesh number whose independence is shown with details in the section 7.2.4 of Chapter 7, was used for both calculations. The chosen mesh is a structured grid with 73,100 hexahedral cells and 50 μm in minimum cell size.

For the calculations, an Intel Core i7 CPU X 980 @ 3.33 GHz X 6 core (each core has 2 threads), 12 GB RAM PC is employed. Injection pressure P_{inj} is set to be 0.22 and 0.25 MPa, while outlet pressure P_{out} is fixed to the environment pressure as 0.1 MPa. At the nozzle walls, a no-slip condition is applied. The default wall functions provided by OpenFOAM are employed for the turbulent quantities k, ϵ, and ν_t.

The first order upwind scheme is used for the discretization of the convection terms of

the turbulence parameters due to stability reasons. Each calculations takes approximately 2.5 days.

5.4 Numerical Results and Discussion

5.4.1 Results of Barotropic Model

Measured and calculated mean velocities at y = -1.5, -3.0 and -6.0 mm for Pin = 0.22 MPa are shown in Figure 5.1. The combination of HEM, Baro and RNG $k-\epsilon$ shown in red lines indicates slightly wrong prediction and underestimation of mean stream-wise velocity especially through the exit of nozzle.

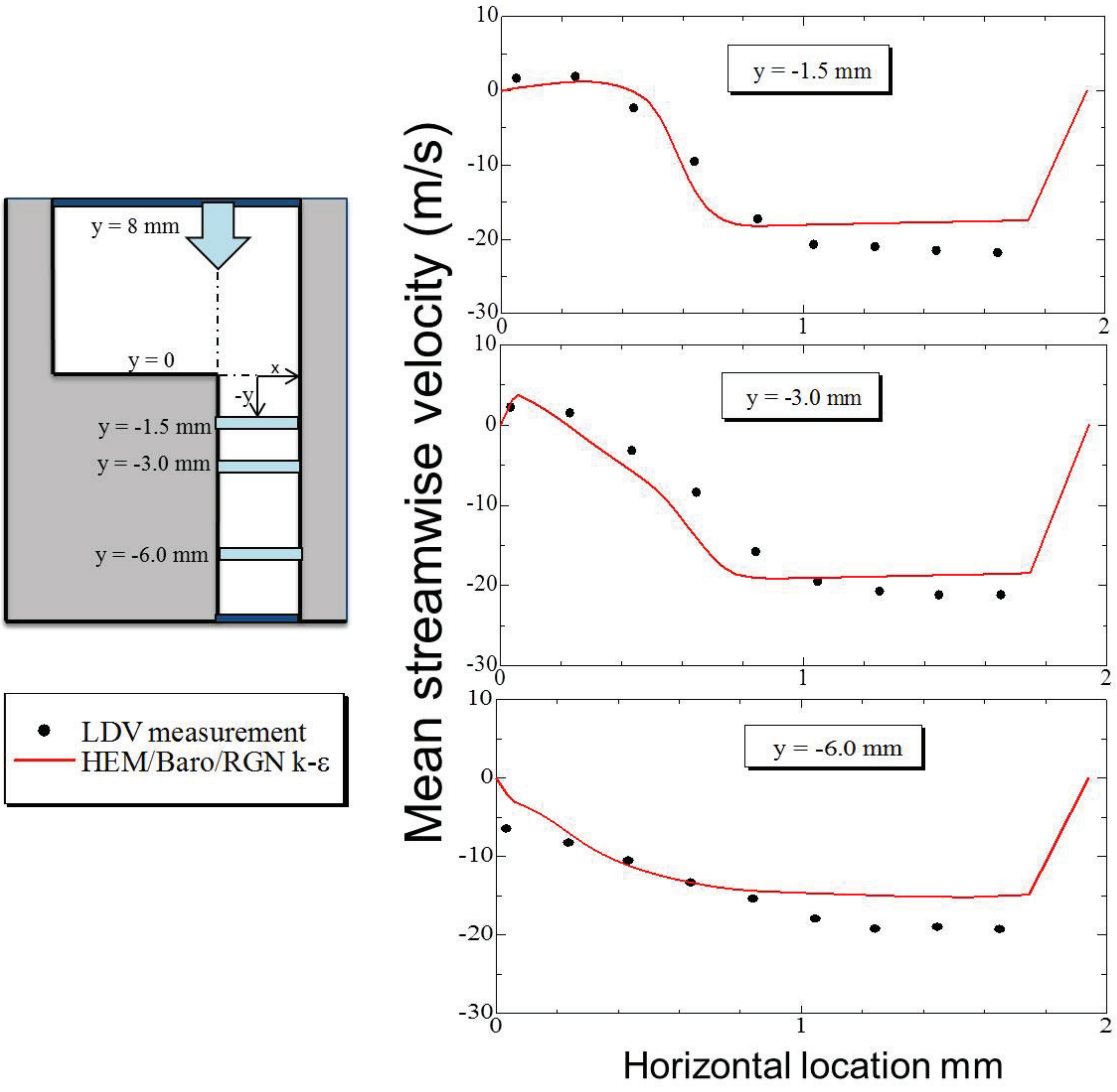

Figure 5.1: Measured and calculated mean velocities at P_{inj} = 0.22 MPa

Figures 5.2, 5.3 and 5.4 show calculated results taken from the central cross section

in depth of the nozzle using the combination of HEM, Baro and RNG $k-\epsilon$ models in terms of liquid volume fraction, pressure and velocity distributions, and turbulence model parameters at $P_{inj} = 0.22$ MPa,$P_{inj} = 0.25$ MPa and $P_{inj} = 0.28$ MPa respectively.

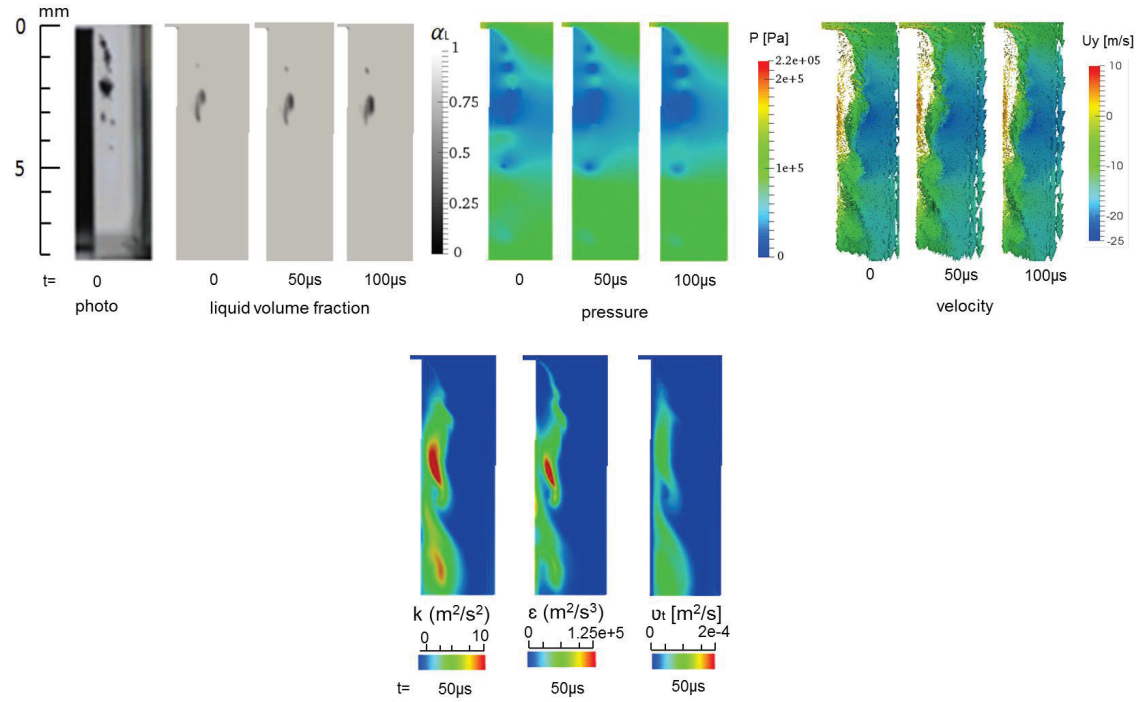

Figure 5.2: Calculated results with barotropic model at P_{inj} = 0.22 MPa

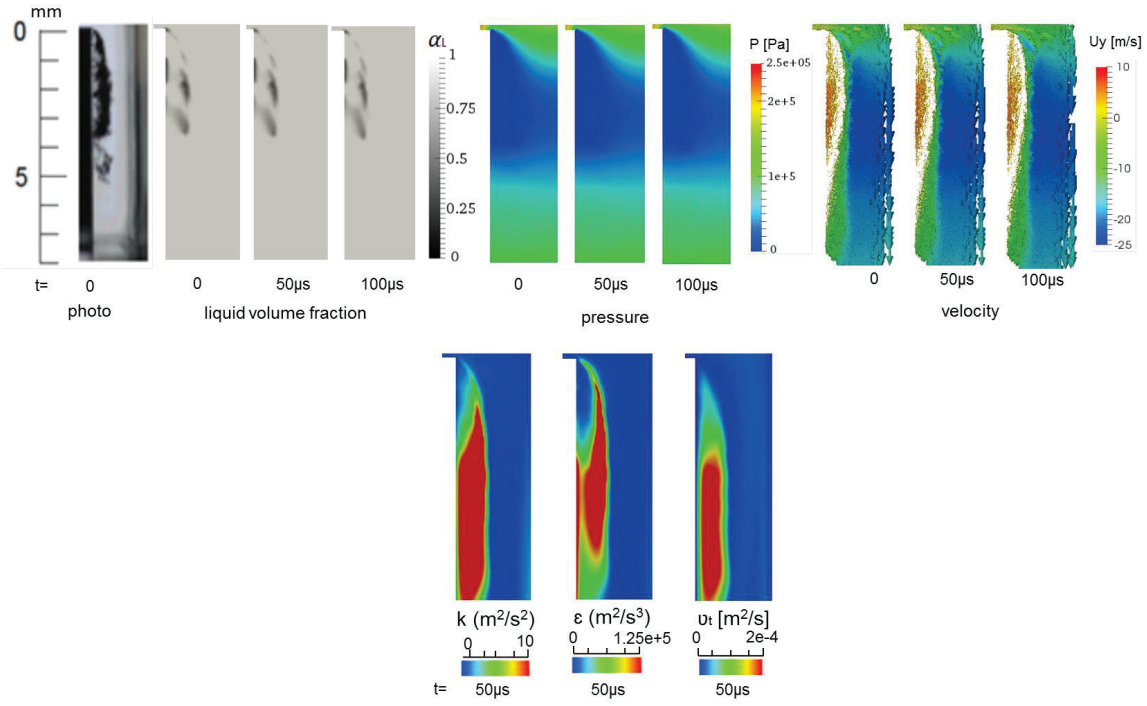

Figure 5.3: Calculated results with barotropic model at P_{inj} = 0.25 MPa

As seen in the results, the combination of HEM, Baro and RNG $k-\epsilon$ underestimates the cavitation region and results in a wrong prediction for cavitation length and thickness. This underestimation can also be seen in Figure 5.5 which shows the measured and calculated mean cavitation length for different injection pressure.

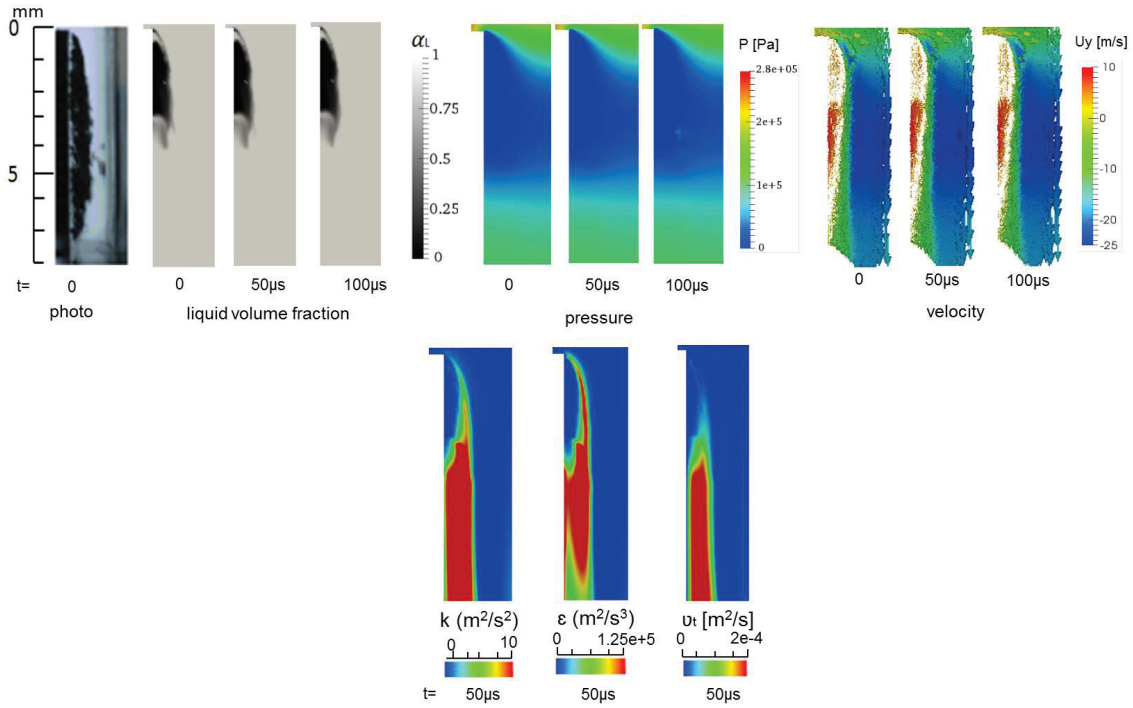

Figure 5.4: Calculated results with barotropic model at P_{inj} = 0.28 MPa

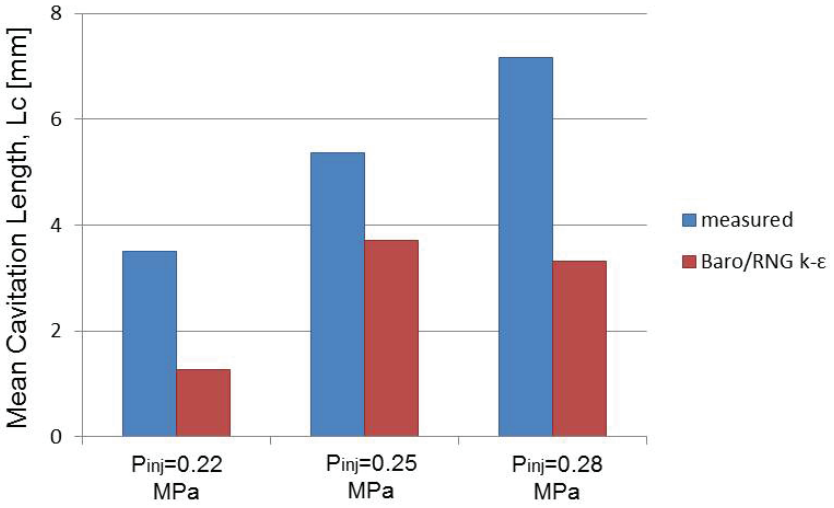

Figure 5.5: Measured and calculated mean cavitation lengths at different conditions

Additionally, this combination is unable to reproduce transient cavitation behaviour with cavitation cloud shedding, which plays a dominant role in atomization of injected

liquid jet and spray for all cases. It should be noted that barotropic closure ignores the bubble dynamics and therefore, it does not have physical sense in the prediction of cavitation. Similar results can be found in our previous works [64, 89, 105].

5.4.2 Results of Kunz's Model

As explained before, Kunz cavitation model includes two empirical constants for condensation C_c and vaporization C_v, which are given 100 in the original formulation. Figure 5.6 displays calculated results taken from the central cross section in depth of the nozzle using the combination of VOF, Kunz and RNG $k-\epsilon$ models in terms of liquid volume fraction, pressure and velocity distributions, and turbulence model parameters at $P_{inj} = 0.22$ MPa. As seen in the results, using 100 for both empirical constants gives underestimation for the cavitation region, and results in wrong prediction for the cavitation length and thickness within recirculation zone. It is also unable to capture the transient cavitation behaviour with cloud shedding.

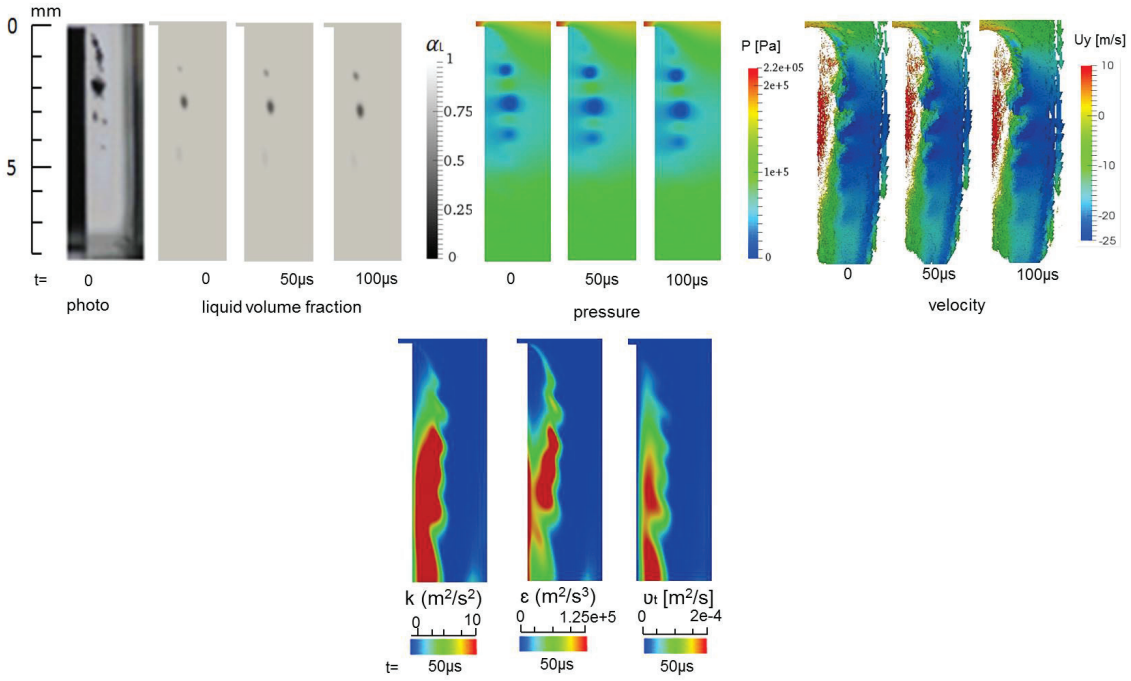

Figure 5.6: Calculated results with Kunz model using $C_c = C_v = 100$ at P_{inj} = 0.22 MPa

After intensive investigations for the constant parameters, C_c and C_v both are set to be 1000 to accurately simulate the cavitation within nozzle. Figure 5.7, Figure 5.8 and Figure 5.9 illustrate the calculated results using the combination of VOF, Kunz and RNG $k-\epsilon$ models in terms of liquid volume fraction, pressure, velocity and turbulence model

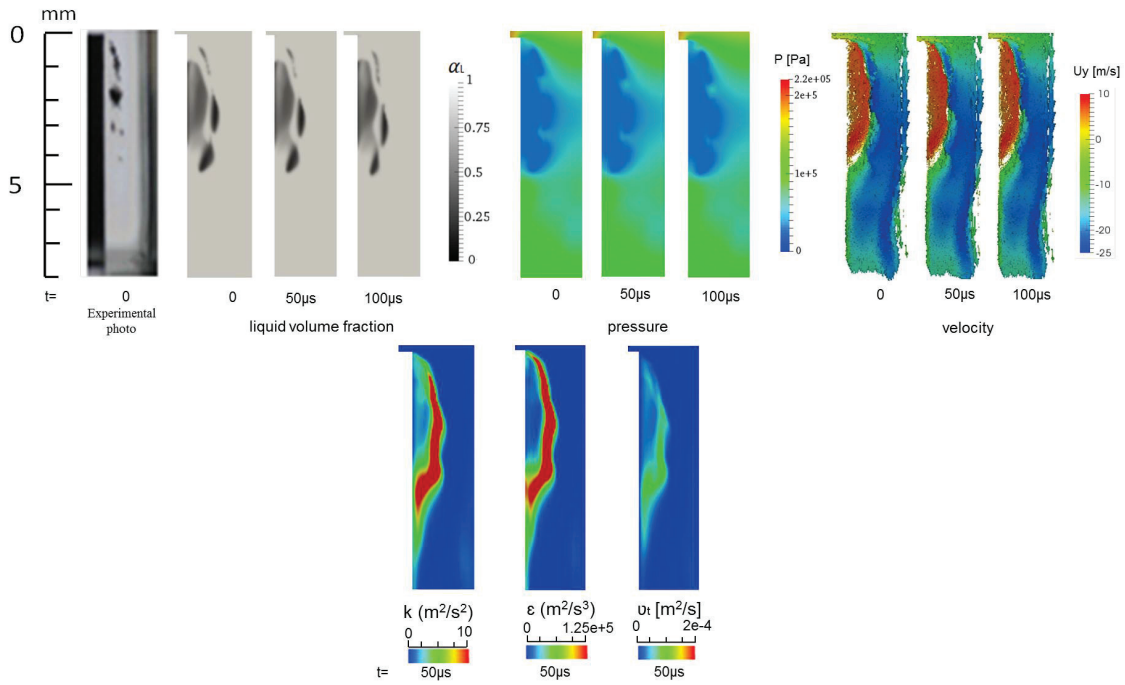

Figure 5.7: Calculated results with Kunz model using $C_c = C_v = 1000$ at P_{inj} = 0.22 MPa

parameters when P_{inj} was 0.22 MPa, 0.25 MPa and 0.28 MPa respectively. As obtained, tuning constant parameters as 1000 results in good prediction and gives better estimation in the sense of cavity length and thickness when compared to experimental data.

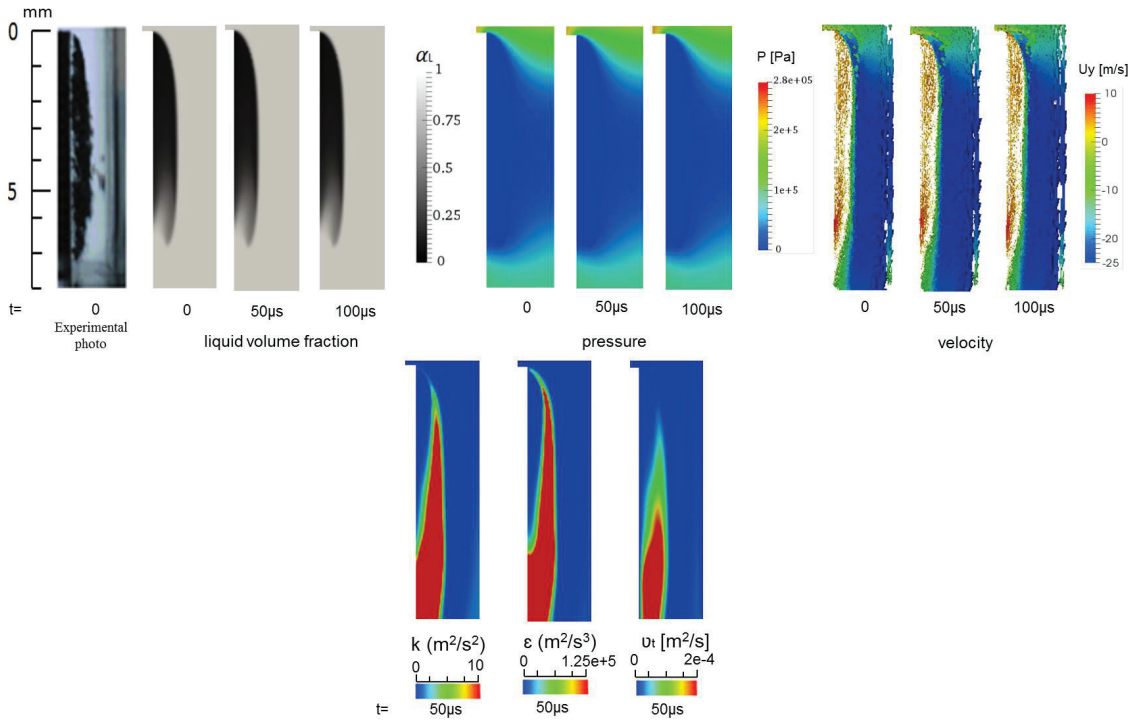

Figure 5.9: Calculated results with Kunz model using $C_c = C_v = 1000$ at P_{inj} = 0.28 MPa

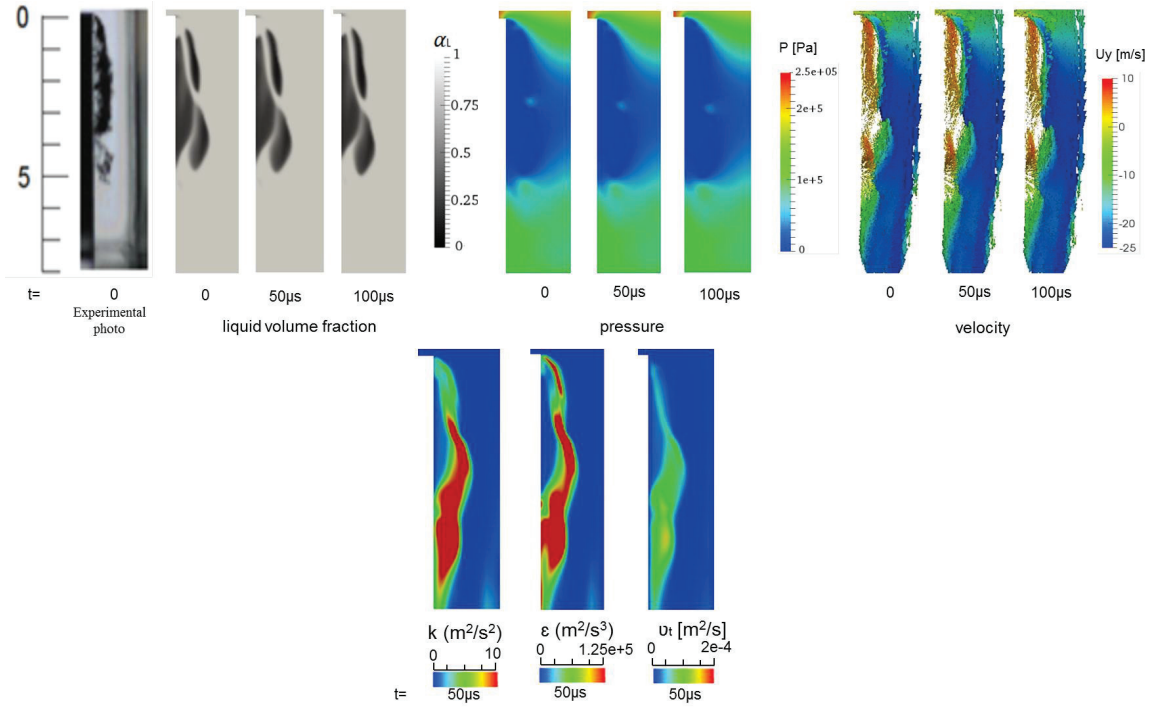

Figure 5.8: Calculated results with Kunz model using $C_c = C_v = 1000$ at P_{inj} = 0.25 MPa

Figure 5.10 also shows calculated and measured cavitation length for the different pressure conditions using tuned parameters. As seen in the results, the combination of Kunz and RNG $k - \epsilon$ models predicts the cavitation lengths with 5-10% error compared to measured data.

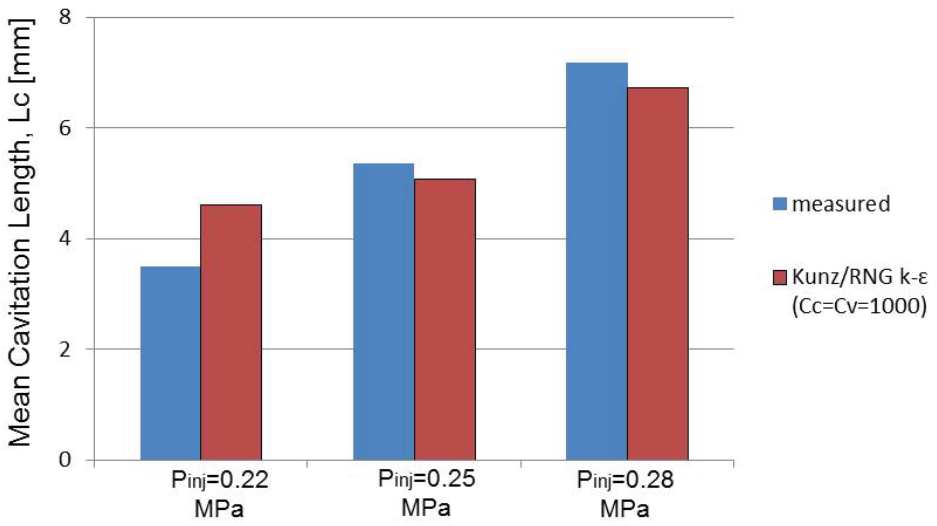

Figure 5.10: Measured and calculated mean cavitation lengths at different conditions

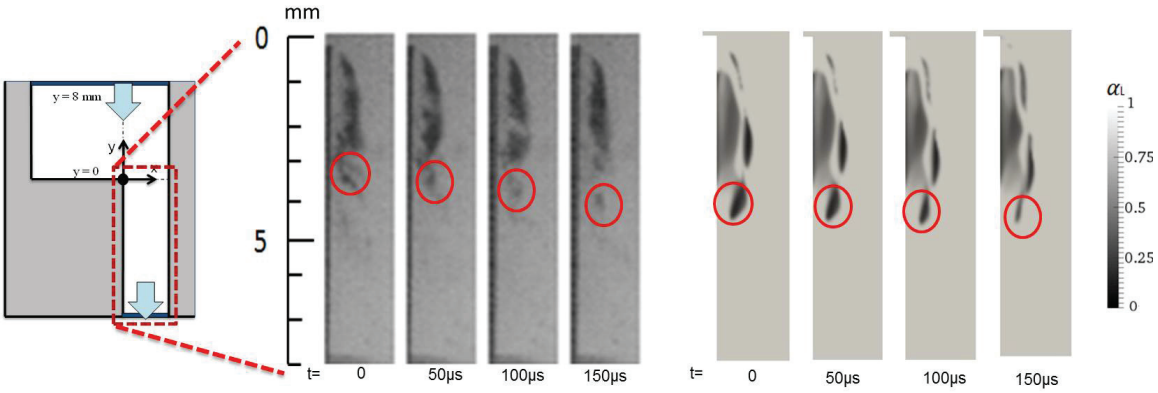

(a) high speed image (b) liquid volume fraction

Figure 5.11: Transient cavitation motion with (a) high speed image (b) Kunz model (P_{inj} = 0.22 MPa)

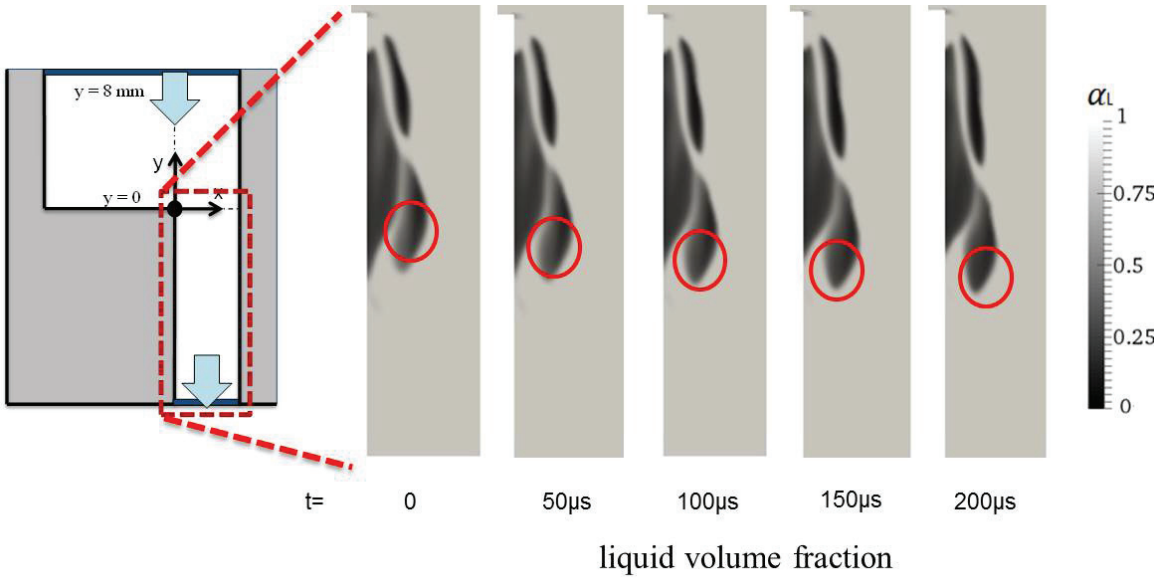

Figure 5.12: Transient cavitation motion obtained with Kunz model (P_{inj} = 0.25 MPa)

Figure 5.11 indicates experimental high speed images of transient cavitation and calculated results taken from the central cross section in depth of the nozzle using the combination of Kunz and RNG $k-\epsilon$ models for P_{inj} = 0.22 MPa. Figure 5.11 (a) was taken using the high speed camera whose time internal is 50 μs. In the low pressure zones within the recirculation region, a huge number of nuclei grow and vortices are shed from the reattachment point. The vortex accompanied by clouds of bubbles is shed and the bubbles collapse during the shedding. The phenomena is well simulated using Kunz's model with the value of 1000 for empirical constants and agreed quite satisfactorily with the high speed image. Figure 5.12 also confirms the validation of the tuned value for model

constants, which displays a good agreement in the prediction of cavitation cloud shedding with the combination of Kunz/ RNG $k-\epsilon$ when P_{inj} is 0.25 MPa.

5.5 Summary

In this Chapter, the feasibility and applicability of the different cavitation models, such as barotropic model and Kunz's cavitation model to turbulent cavitating flows in a fuel injector nozzle are investigated. The validity of numerical results are verified through the experimental data. As a result, the following conclusions are attained.

- The combination of HEM, Barotropic and RNG $k-\epsilon$ under-estimates the cavitation region and results in a wrong prediction for cavitation length and thickness for all cases. Also, It cannot reproduce transient cavitation behavior, which plays a dominant role in atomization of injected liquid jet and spray.

- It is found that tuning parameter of the model constants is so important in order to accurately predict the transient cavitation with Kunz's model.

- Using original value 100 for the model constants gives underestimation for the cavitation region, and results in wrong prediction for the cavitation length and thickness within recirculation zone. It is also unable to capture the cavitation cloud shedding.

- After tuning model parameters to 1000, the combination of VOF, Kunz and RNG $k-\epsilon$ models results in good prediction and gives better estimation in the sense of cavity length and thickness within nozzle. Also, the transient motion of cavitation such as cloud shedding in the recirculation zone is well-predicted. Also, this combination is able to predict supercavitation inside nozzle well.

- Finally, it can be stated that the applicability of barotropic model into modelling of the nozzle cavitation is limited whereas tuning of the model constants are crucial for the correct applicability of Kunz's model.

Chapter 6

Model Combination of Eularian-Lagrangian BTM / RP / LES

6.1 Introduction

This Chapter presents the details and results related to first proposed combination model of Eularian-Lagrangian Bubble Tracking Method (BTM), Rayleigh-Plesset (RP) equation and Large Eddy Simulation, which is in-house code, as indicated in Table 6.1. It is also given model equations, turbulence model description, boundary and initial conditions of the numerical model. This study includes one of the achievements of the present thesis and published in the international journal of Computer&Fluids [19].

Table 6.1: Summary of the combined model

Multiphase Modelling	**Cavitation Modelling**	**Bubble Dynamics**	**Turbulence Model**	**CFD Tool**
Two-Fluids (E-L)	-	RP	LES	In-house code

As explained in previous chapters, the cavitation clouds shedding in a nozzle of fuel injector for diesel engines plays a dominant role in the fuel spray atomization process and the subsequent spray combustion. Cavitation in the nozzle takes various forms, such as a transparent cavitation sheet and clouds of cavitation bubbles, which makes its prediction difficult.

As a first step to develop a cavitation model which can accurately treat both the sheet and cloud cavitations, it is proposed a model combination of BTM, LES and RP equation to simulate the an incipient cavitation, in which only cavitation bubble clouds appear. The growth and collapse of cavitation bubbles and nuclei are computed by tracking their trajectories in a Lagrangian manner and solving the Rayleigh-Plesset equation.

A precursor simulation of a fully developed turbulent flow in a channel, in which periodic boundary condition is adopted for the inlet and exit, is carried out to generate inlet boundary condition for a nozzle simulation.

To verify the validity of the model, the experimental data of one-side rectangular nozzle, whose results are presented in Chapter 4, is used. The transient cavitation motion and turbulent velocity in a rectangular nozzle was acquired by using a high speed camera and Laser Doppler Velocimetry (LDV), which are useful for a quantitative verification of turbulent cavitation flow models.

6.2 Numerical Models

6.2.1 Eularian-Lagrangian Bubble Tracking Model

Growth and collapse of cavitation bubbles and nuclei are computed by solving the following Rayleigh–Plesset equation [90];

$$\ddot{R}_b + \frac{3}{2}\dot{R}_b{}^2 = \left(P_b - P_L - \frac{4\mu_L \dot{R}_b}{R_b} - \frac{2\sigma}{R_b} \right) \tag{6.1}$$

where R_b denotes the bubble radius, μ_L the liquid viscosity and σ the surface tension, respectively. The local instantaneous pressure at the center of the bubble is used as the liquid pressure P_L. Pressure inside the bubble P_b is given by (as previously explained in Chapter 3.2)

$$P_b = P_G + P_V = \left(P_{L0} - P_V - \frac{2\sigma}{R_0} \right) \left(\frac{R_0}{R_b} \right)^{3\kappa} + P_V \tag{6.2}$$

where κ is the ratio of the specific heats, and subscript 0 shows the initial value. The non-condensable gas P_G is calculated by

$$constant = \begin{cases} P_G R_b^3 & \text{if } \frac{dR_b}{dt} > 0 \quad (6.3a) \\ P_G R_b^{3\kappa} & \text{if } \frac{dR_b}{dt} < 0 \quad (6.3b) \end{cases}$$

To evaluate accurately the local instantaneous pressure P_L in equation 6.1, all bubbles and nuclei are tracked by the solving the following equation of n^{th} motion [106]:

$$(\rho_b^n + C_{VM}\rho_L)\frac{d\mathbf{u}_b^n}{dt} = (1 + C_{VM})\rho_L \frac{d\bar{\mathbf{u}}_L}{dt} - \mathbf{F}_d^n - \mathbf{F}_{lf}^n + (\rho_b^n - \rho_L)\mathbf{g} \tag{6.4}$$

where ρ_b and ρ_L are the bubble and liquid densities, C_{VM} the virtual mass coefficient ($C_{VM} = 0.5$), the time, and $\mathbf{g}$ the gravitational acceleration, respectively. The $\mathbf{u}_b$ and $\mathbf{u}_L$

denote the bubble and the liquid velocities at the bubble center. The $\mathbf{F}_d$ and $\mathbf{F}_{lf}$ are the drag force and the lift force calculated by the following correlations [106].

$$\mathbf{F}_d = \frac{3}{4D_b} C_d \rho_L |\mathbf{u}_b - \bar{\mathbf{u}}_L| (\mathbf{u}_b - \bar{\mathbf{u}}_L) \tag{6.5}$$

$$\mathbf{F}_{lf} = C_{lf} (\mathbf{u}_b - \bar{\mathbf{u}}_L) \times (\nabla \times \bar{\mathbf{u}}_L) \tag{6.6}$$

where D_b is the bubble diameter. C_d and C_{lf} show the he drag and lift coefficients for a single bubble and are given by [106]

$$C_d = \frac{24}{Re_b} (1 + 0.15 Re_b^{0.687}) \tag{6.7}$$

$$C_{lf} = 0.5 \tag{6.8}$$

where Re_b is the bubble Reynolds number and defined by

$$Re_b = \frac{\rho_L |\mathbf{u}_b - \bar{\mathbf{u}}_L| D_b}{\mu_L} \tag{6.9}$$

The Lagrangian manner enables us to avoid the numerical diffusion of bubble distribution, to accurately compute the bubble diameter, and to compare calculated and visualized bubble distributions.

The initial bubble diameter is decided by considering the critical pressure P_C and the lowest pressure P_{min} obtained in the simulation. The minimum pressure obtained in our simulation is about $-0.1\ MPa$, by which we confirm that small nuclei whose radii are smaller than 0.3 μm will not grow. We carried out visualization with high spatial resolution and concluded that there are almost no bubble nuclei whose radii are larger than 6 μm. The number density of smaller nuclei is usually much larger than that of larger nuclei. Therefore, in this case we should treat the nuclei whose initial radii are between 1 and 5 μm. For simplicity, the initial radii of the nuclei are set to be 1.5 μm. Following some previous literatures, the nuclei number density for them is set to $10^{12}\ 1/m^3$.

Initial bubble nuclei are randomly distributed into the recirculation zone. When they reach the nozzle exit, they are removed from the calculation. New nuclei are provided from the inlet of the nozzle whose exact positions are randomly calculated according to the flow rate and nuclei number density. Nuclei and growing bubbles are tracked only within the nozzle, and about 32,000 nuclei are calculated in the recirculation zone.

Time step size to solve the flow field is 100 ns, while that to solve the Rayleigh–Plesset equation is 10 ns for an accurate prediction of bubble diameters. The maximum void fraction is less than 0.1% in the present cases, and we ignore bubble collision, coalescence, breakup, and bubble-induced turbulence.

6.2.2 Large Eddy Simulation (LES)

There are some previous works to simulate the turbulent cavitating flow in a nozzle using LES [87, 107–109]. Filtered mass and momentum conservation equations for incompressible turbulent liquid flow are solved as the basic equations:

$$\frac{\partial \bar{u}_i}{\partial x_i} \tag{6.10}$$

$$\frac{\partial \bar{u}_i}{\partial t} + \bar{u}_j \frac{\partial \bar{u}_i}{\partial x_j} = -\frac{1}{\rho_L}\frac{\partial \bar{P}}{\partial x_i} + \frac{\partial}{\partial x_j}(-\tau_{ij} + 2\nu \bar{D}_{ij}) + g_i \tag{6.11}$$

where D_{ij} is given by

$$\bar{D}_{ij} = \frac{1}{2}\left(\frac{\partial \bar{u}_i}{\bar{u}_j} + \frac{\partial \bar{u}_j}{\bar{u}_i}\right) \tag{6.12}$$

In this work, the applicability of the standard Smagorinsky model and the subgrid-scale eddy viscosity model proposed by Vreman [110] to the turbulent flow in a nozzle is examined. We applied van Driest's wall damping function near the wall, and the Smagorinsky constant C_S is set to be 0.10, which is usually used for a channel flow LES. The velocity and pressure fields are obtained by solving equations 6.10-6.12 using modified SOLA [111].

6.2.3 Computational Grid and Boundary Conditions

Figure 6.1 shows the schematic of the computational grids for the precursor and nozzle simulations.

A precursor simulation of a fully developed turbulent flow in a rectangular channel, in which periodic boundary condition is adopted at the inlet and exit as illustrated in Figure 6.1, is conducted to generate the inlet boundary condition for the nozzle simulation. The length, width and depth of the precursor simulation domain are 8 mm, 8 mm and 2 mm, respectively. The precursor simulation is carried out until a quasi-steady state turbulent channel flow data are obtained. The velocity data at the center cross-section are

used as the inlet boundary condition for the nozzle simulations. The initial exit pressure P_{out} is set to be 0.1 MPa, which agrees with the experimental condition.

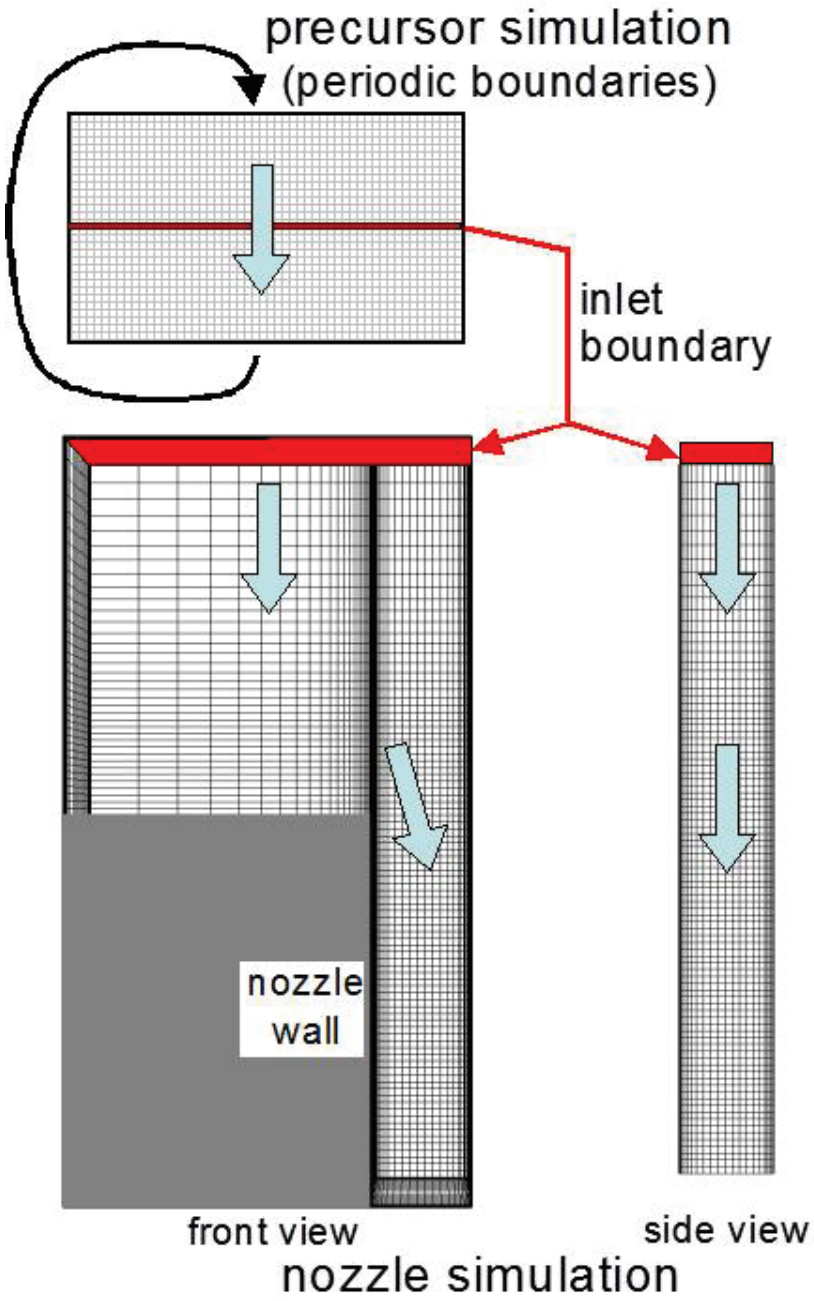

Figure 6.1: Computational grids for the precursor and the nozzle simulations (grid lines were drawn every $4 \times 4 \times 4$ cells)

In Figure 6.1, grid lines are drawn every $4 \times 4 \times 4$ cells. Through a sensitivity analysis, the minimum size of the cells near the nozzle wall is set to be 4 μm, by which one or two cells are assigned within the viscous sub layer. The largest mesh size in the nozzle center is 52 μm. About 700,000 cells are used for the precursor simulation, and 2,800,000 cells are used in the nozzle simulations. By using the fine grid we observed strong turbulence

and cavitation growth in the nozzle, while lesser bubbles grow in weaker turbulence flow using coarser grids whose minimum cell size is 8 μm or 12 μm.

A Linux computer with 3.0 GHz $\times$ 32 core, 16 CPU and 64 GB memories per node is used for the numerical calculations. Time step Δt is set to be $10^{-8} s$. The CPU time for a precursor simulation is about three weeks to reach steady state, while that for a nozzle simulation is about one week.

6.3 Results and Discussion

6.3.1 Turbulent Flow in Nozzle

Figure 6.2 shows the mean and turbulence velocities measured by LDV at 8 mm upstream of the nozzle and the predicted results for the fully developed turbulent channel flow in the precursor simulations. Calculated turbulent flow in the upstream is in good agreement with measured result.

Measured and simulated velocities at y=-1.5, -3.0 and 6.0 mm, where y is the vertical distance from the inlet of the nozzle, for $V_n = 12.8\ m/s$ are shown in Figure 6.3. The calculated results by the Smagorinsky and Vreman's SGS models are represented in red and blue lines, respectively. These results agree well for each other.

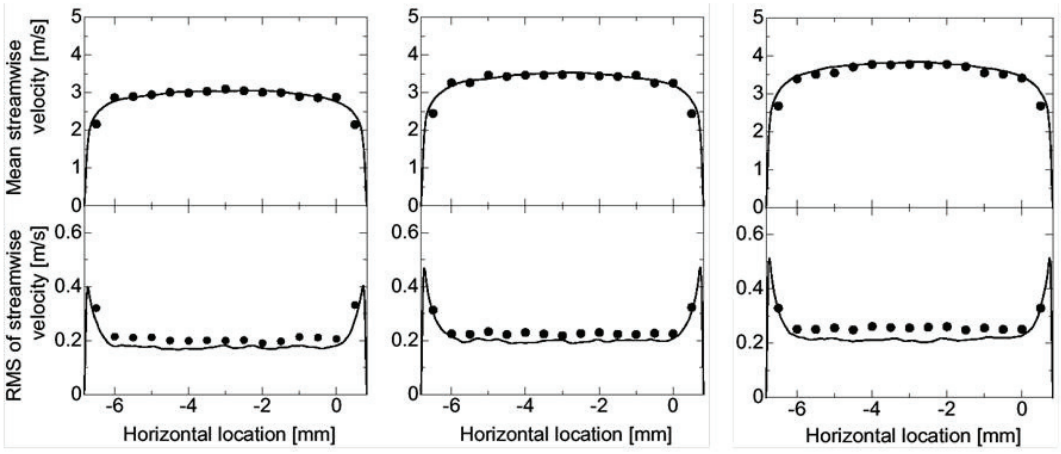

Figure 6.2: Liquid velocity in the upstream of the nozzle

Although a slight underestimation in turbulence is found near the outer edge of the recirculation zone, where cell size is not very fine, both SGS models give a reasonable

prediction for a turbulent flow with a recirculation flow and the reattachment of the separated boundary layer occurring at the position of y=3.0-6.0 mm.

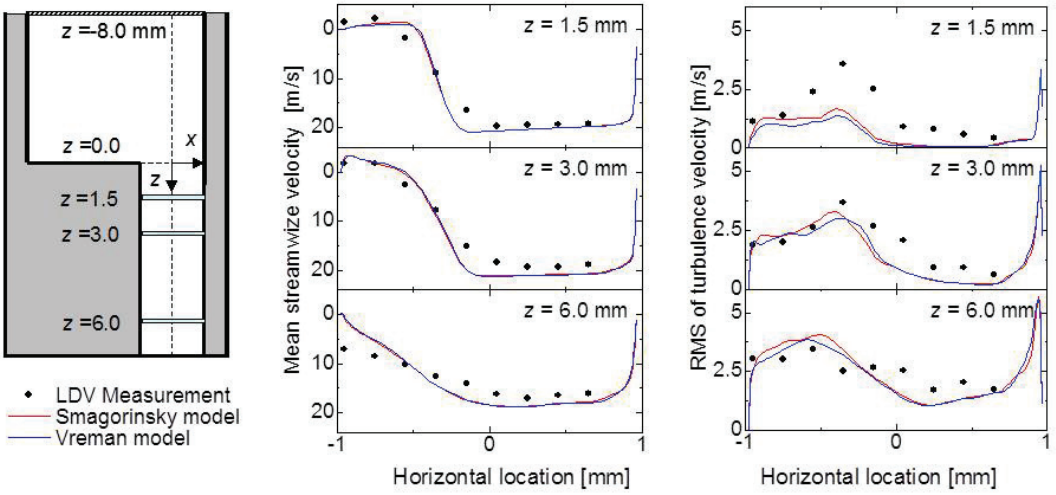

Figure 6.3: Mean and turbulence velocities in the nozzle ($V_n = 12.8m/s$)

6.3.2 Transient Cavitation in Nozzle

Figure 6.4 shows the experimental and calculated cavitation flows using the standard Smagorinsky model for $V_n = 12.8m/s$. Note that we obtained an almost same numerical result by using Vreman's model. Pressure, velocity and vorticity distributions are the results at the middle plane in depth of the nozzle channel.

The image shown in Figure 6.4(a) was taken using the high speed camera whose exposure time was 50 μs. The calculated bubble distribution shows the integrated cavitation in the depth direction, since the experimental pictures of cavitation bubbles are also integrated in the depth direction using a back lighting. In the computed bubble distribution, only the bubbles larger than 3.3 μm were drawn in real scale.

As obtained, a great number of nuclei grow in the low pressure regions along the outer edge of the recirculation zone with a large shear and the vortex shedding from the tail of the reattachment point. We can conclude that the calculated and experimental bubble distributions agree well, which indicates the applicability of the combination of LES, BTM and RP to the cavitation inception in the nozzle. Note that diameters of most of the growing bubbles are less than 20 μm in the case. Also, Figure 6.5 shows measured and calculated mean cavitation lengths at vertical direction when P_{inj}=0.22 MPa. As seen that cavitation length is well-predicted with a small error by the combination of LES, BTM

and RP models.

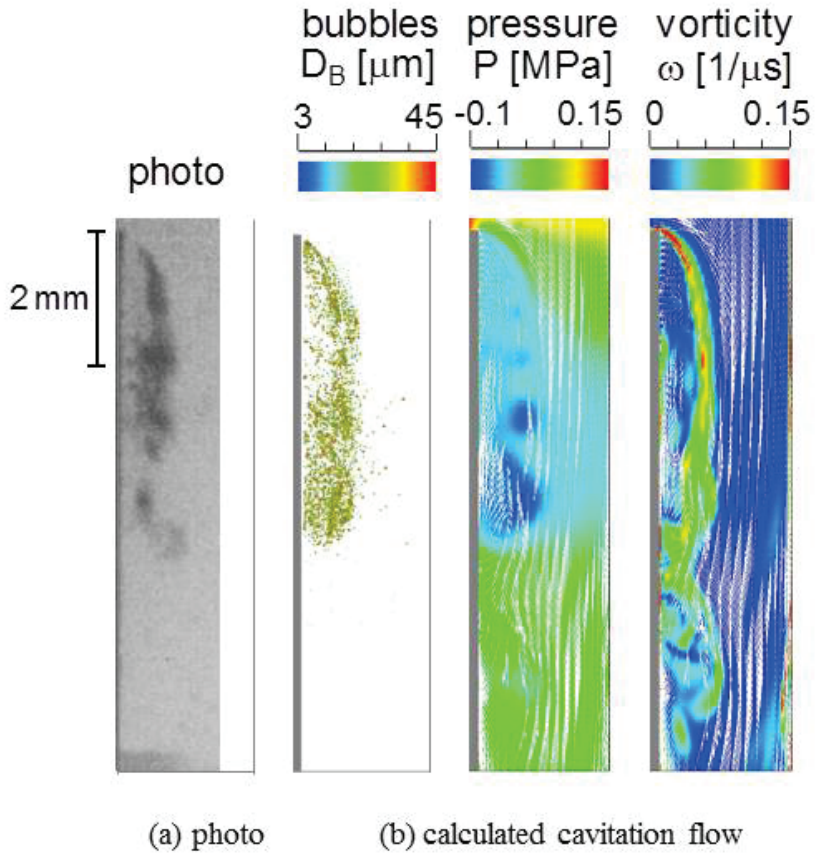

Figure 6.4: Observed and calculated cavitation flows ($V_n = 12.8m/s$)

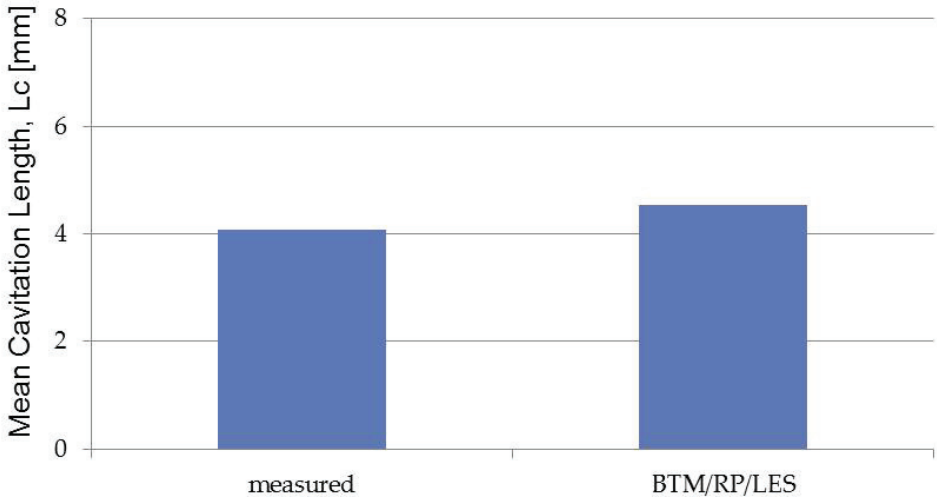

Figure 6.5: Measured and calculated mean cavitation lengths ($P_{inj} = 12.8m/s$)

High speed images of transient cavitation flow and calculated cavitation behavior at $V_n = 12.8m/s$ were illustrated in Figure 6.6. The calculation is again with the Smagorinsky model, which agrees with that with Vreman's model. The transient result clearly concludes

that the shedding of a vortex accompanied by clouds of collapsing bubbles, which plays a dominant role in the deformation and atomization of discharged liquid jet and has not predicted well in the previous simulations yet, is well simulated by the present combination of model.

A good agreement is also obtained in the case of lower velocity of $V_n = 10.6m/s$ as shown in Figure 6.7. These results conclude that the LES/BTM/RP model enables us to simulate cavitation cloud shedding in incipient cavitation regime and to quantitatively predict the turbulent flow and the cavitation length and thickness in a nozzle.

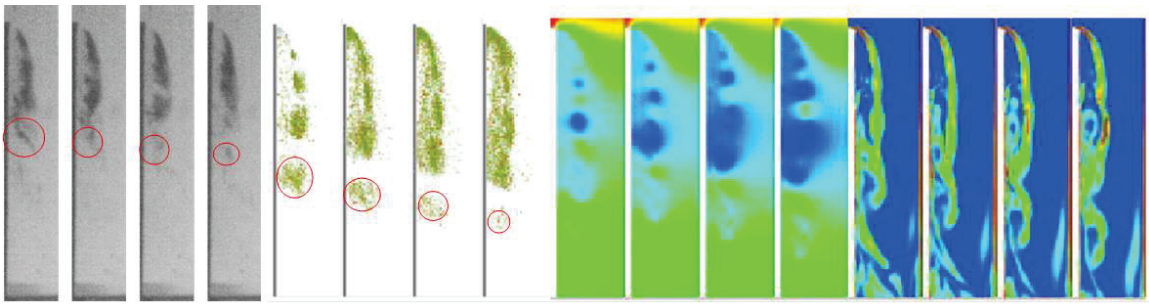

(a) high-speed image (b) simulated bubbles (c) pressure contour (d) vorticity contour

Figure 6.6: Transient cavitation motion ($V_n = 12.8m/s$, results are shown every 50 μs)

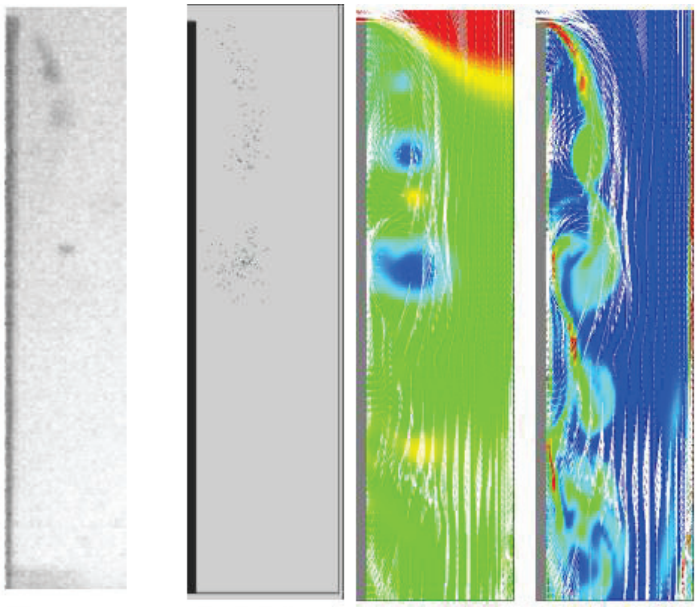

Figure 6.7: Observed and calculated cavitation flows ($V_n = 10.6m/s$)

6.4 Summary

In this Chapter, results of the combination of Large Eddy Simulation (LES), Bubble Tracking Method (BTM), and the Rayleigh–Plesset (RP) bubble dynamics equation is presented in order to predict quantitatively the cavitation thickness and length and to simulate cavitation cloud shedding in incipient cavitation flows inside the nozzle of a Diesel fuel injector.

Precursor simulations of fully-developed turbulent flows in a rectangular channel are carried out to generate inlet boundary condition for cavitating nozzle simulations.

To verify the validity of the new model, the length and thickness of cavitation zone in an one-side rectangular nozzle are used, and the transient motion of incipient cavitation with a cloud shedding as well as turbulent velocity in the nozzle were acquired by using a high-speed camera and a Laser Doppler Velocimetry (LDV), respectively. As a result, it is found that

- a recirculation flow near the inlet edge and the vortex shedding from the tail of the reattachment point are successfully predicted and turbulent flows in the nozzle are quantitatively predicted well by LES with a fine grid,
- the length and thickness of the cavitation zone are quantitatively predicted well,
- a cavitation cloud in a vortex shedding from the tail of the cavitation zone is well reproduced by solving the RP equation for all nuclei and bubbles tracked in a Lagrangian manner for incipient cavitation regime.

Chapter 7

Application of New Bubble Dynamics Model to Fuel Injector Nozzle

7.1 Introduction

As already mentioned before, cavitation occurring inside diesel injector nozzles plays a key role in atomization of fuel spray. Most of cavitation models based on bubble dynamics use the Rayleigh (R) equation, which employs the vapour saturation pressure P_V and it is sometimes called simplified Rayleigh-Plesset (RP) equation, to simulate the growth and collapse of bubbles.

We have already found that that R equation over-predicts for cavitation when local pressure is slightly below P_V as indicated in Chapter 3. Therefore, a Modified Rayleigh (MR) equation taking into account the critical pressure P_C is proposed, and presented its validity by comparing with R and RP equations using several test cases with uniform pressure in Chapter 3.

In this Chapter, the applicability of the MR equation to turbulent cavitating flows and its superiority versus R equation in a fuel injector nozzle are presented. OpenFOAM is used for the numerical simulation of turbulent cavitating flows and turbulent effect is taken into account using RNG $k-\epsilon$, which is known to applicable to the flow with separation and reattachment. Table 7.1 shows the summary of the combined models used within this chapter.

Numerical results are validated with the experimental data, whose results are presented in Chapter 4, in terms of cavitation length, thickness and cavitation cloud shedding behaviour in an one-side rectangular nozzle. The transient cavitation motion and turbulent velocity in a rectangular nozzle was acquired by using a high speed camera and Laser Doppler Velocimetry (LDV), which are useful for a quantitative verification of

turbulent cavitation flow models.

Table 7.1: Summary of the combined models

	Multiphase Modelling	**Cavitation Modelling**	**Bubble Dynamics**	**Turbulence Model**	**CFD Tool**
1.	Simplified VOF	Schnerr-Sauer	MR	RNG $k-\epsilon$	OpenFOAM
2.	Simplified VOF	Schnerr-Sauer	R	RNG $k-\epsilon$	OpenFOAM

7.2 Numerical Model

7.2.1 Two-phase Flow Modelling

In order to model the turbulent cavitating flow, two-phase treatment is needed to be determined with the mechanism of the phase transformation between liquid and gas phases. A homogeneous equilibrium two-phase mixture method (HEM) is used, which supposed that liquid and vapour phases are perfectly mixed in each cell and one set of conservation equations are solved for the mixture phase. To specify the phase change between liquid and vapour, the following transport equation based on liquid volume fraction α_L is used

$$\frac{\partial(\alpha_L \rho_L)}{\partial t} + \nabla \cdot (\alpha_L \rho_L \mathbf{U}) = R_c + R_e \tag{7.1}$$

where $\mathbf{U}$, R_c and R_e display mixture velocity, rate of mass transfer source terms for condensation and evaporation, respectively. The density and viscosity of the mixture phase are calculated based on the volume fraction of the liquid phase as follows

$$\rho_m = (1-\alpha_L)\rho_V + \alpha_L \rho_L \tag{7.2}$$

$$\mu_m = (1-\alpha_L)\mu_V + \alpha_L \mu_L \tag{7.3}$$

where ρ_m and μ_m are the density and viscosity of mixture phase, while ρ_V, ρ_L, μ_V and μ_L represent vapour and liquid densities and dynamic viscosities, respectively. The continuity (mass conservation) was given for the mixture phase by

$$\frac{\partial \rho_m}{\partial t} + \nabla \cdot (\rho_m \mathbf{U}) = 0 \tag{7.4}$$

By substituting Equation 7.1 into Equation 7.4, the mass conservation can be rewritten in the form of velocity divergence as

$$\nabla \cdot \mathbf{U} = -\frac{1}{\rho_m}\frac{d\rho_m}{dt} = \frac{\rho_L - \rho_V}{\rho_m}\frac{d\alpha_L}{dt} \tag{7.5}$$

This shows that divergence velocity field is no longer zero. If Equation 7.5 is put into Equation 7.1, the mass transfer source terms can be obtained as

$$R_c + R_e = \frac{\rho_L \rho_V}{\rho_m}\frac{d\alpha_L}{dt} \tag{7.6}$$

Regarding to mass transfer source terms definition in Equation 7.6, the continuity equation can be written subject to the source terms as follows:

$$\nabla \cdot \mathbf{U} = R_c + R_e\left(\frac{1}{\rho_L} - \frac{1}{\rho_V}\right) \tag{7.7}$$

The momentum equation is written for the mixture phase

$$\frac{\partial \rho_m \mathbf{U}}{\partial t} + \nabla \cdot (\rho_m \mathbf{U}\mathbf{U}) = -\nabla P + \nabla \cdot [\mu_{eff}(\nabla \mathbf{U} + (\nabla \mathbf{U})^T)] \tag{7.8}$$

where μ_{eff} is the effective viscosity and given by

$$\mu_{eff} = \mu_m + \mu_t \tag{7.9}$$

where μ_m and μ_t denote the molecular and turbulence viscosities. The latter is modelled by one of the RANS turbulence model such as RNG $k - \epsilon$ model.

7.2.2 Cavitation Model

To specify sources terms in the RHS of the transport Equation 7.1, the cavitation model, which is based on bubble dynamics and developed by Schnerr and Sauer [20], is chosen due to widely use in the literature [57, 71–76].

Bubble growth and collapse are calculated using Rayleigh (R) equation in this model, and model equations are already given in section 2.4.2.2. R equation uses vapour saturation pressure P_V as threshold for evaporation and condensation. In this model, mass transfer rates are given by using R equation as

$$R_e = \quad -C_v \frac{3\rho_L \rho_V}{\rho_m}\frac{\alpha_L(1-\alpha_L)}{R_b} sgn(P_V - P_L)\sqrt{\frac{2\,|P_V - P_L|}{3\rho_L}} \qquad , P_L < P_V \tag{7.10}$$

$$R_c = \quad C_c \frac{3\rho_L \rho_V}{\rho_m} \frac{\alpha_L(1-\alpha_L)}{R_b} sgn(P_V - P_L) \sqrt{\frac{2\,|P_L - P_V|}{3\rho_L}} \qquad , P_V < P_L \tag{7.11}$$

where C_c and C_v are the rate constants for condensation and vaporization, respectively and they are set to be 1 for calculations. Therefore, the effects of the empirical constants are ignored. However, as already shown in Chapter 3, R equation over-estimates bubble growth since cavitation takes place when the local pressure is less than the vapour saturation pressure P_V instead of critical pressure P_C. To avoid this overestimation and to precisely model the cavitation inside injector nozzle, the MR equation based on the critical pressure, whose definition is given in section 3.2.1, is used.

Bubble collapse in Schnerr-Sauer model is also driven by R equation. However, the bubble collapse speed is faster than the bubble growth speed. Therefore, R equation is slightly modified for the bubble collapse by changing the constant $2/3$ to 1.27 [89]. Finally, mass transfer rates based on P_C are given as,

$$R_e = -C_v \frac{3\rho_L \rho_V}{\rho_m} \frac{\alpha_L(1-\alpha_L)}{R_b} sgn(P_C - P_L) \sqrt{\frac{2\,|P_V - P_L|}{3\rho_L}} \quad , P_L < P_C$$

$$R_e = R_c = 0 \qquad , P_C < P_L < P_V \tag{7.12}$$

$$R_c = C_c \frac{3\rho_L \rho_V}{\rho_m} \frac{\alpha_L(1-\alpha_L)}{R_b} sgn(P_L - P_C) \sqrt{1.27 \frac{|P_L - P_V|}{\rho_L}} \quad , P_V < P_L$$

As seen in Equation 3.12 and Equation 3.13, the critical pressure P_C depends on the injection pressure P_{inj} and the initial radius R_0 of the bubble nuclei. The relationship between P_C and initial nuclei diameter $D_0 = 2R_0$ is shown in Figure 7.1 for a water injection case when the injection pressure of P_{inj} is 0.22 MPa.

As seen in Figure 7.1, P_C does not change a lot for $D_0 \geq 2\mu m$. For the all the present simulations, initial bubble radius R_0 and the nuclei number density n_0 are set to be 1 μm and 10^{14} $nuclei/m^3$, respectively. It should be noted that nuclei do not grow at or slightly below P_V but start to grow when $P_L < P_C$ and start to collapse when $P_V < P_L$ for proposed MR model.

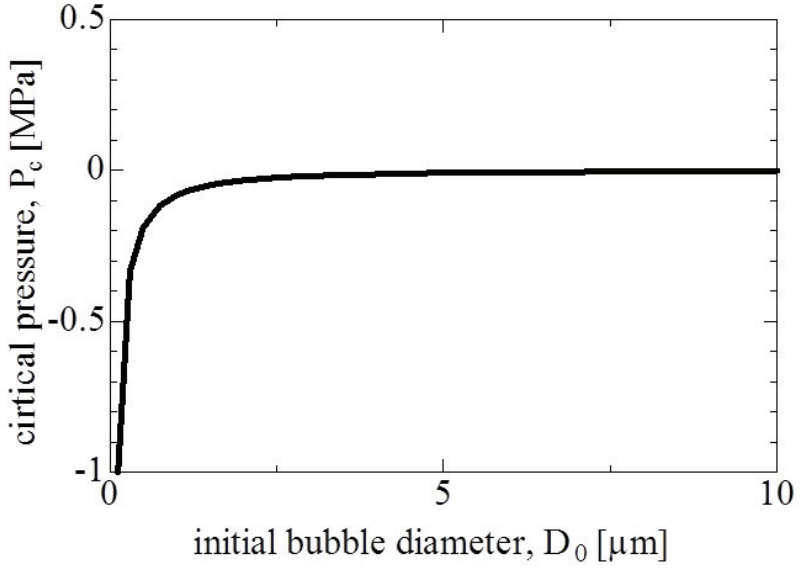

Figure 7.1: P_C variation subject to D_0 at P_{inj} = 0.22 MPa

7.2.3 RNG $k-\epsilon$ Turbulence Model

RNG $k-\epsilon$ turbulence model proposed by Yakhot *et al.* [112] is used to represent the effects of turbulence in the simulations. This model is derived from conventional $k-\epsilon$ model by modifying the dissipation rate ϵ equation in order to include the effects of the different scales of motion changes into turbulent diffusion. Model equations are given by [113]

$$\frac{\partial \rho_L k}{\partial t} + \nabla \cdot (\rho_L k \mathbf{U}) = \nabla \cdot (\alpha_k \mu_{eff} \nabla k) + \tau_{ij}.S_{ij} - \rho_L \epsilon \tag{7.13}$$

$$\frac{\partial \rho_L \epsilon}{\partial t} + \nabla \cdot (\rho_L \epsilon \mathbf{U}) = \nabla \cdot (\alpha_\epsilon \mu_{eff} \nabla \epsilon) + C^*_{1\epsilon} \tau_{ij}.S_{ij} - C_{2\epsilon} \rho_L \frac{\epsilon^2}{k} \tag{7.14}$$

where $\alpha_k = \alpha\epsilon$, $C_{1\epsilon}$ and $C_{1\epsilon}$ are models constants and given 1.39, 1.42 and 1.68, respectively. Reynolds stresses and $C^*_{1\epsilon}$ are defined

$$\tau_{ij} = -\rho_L \overline{u_i' u_j'} = 2\mu_t S_{ij} - \frac{2}{3}\rho_L k \delta_{ij} \tag{7.15}$$

$$C^*_{1\epsilon} = C_{1\epsilon} - \frac{\eta(1-\eta/\eta_0}{1+\beta\eta^3} \tag{7.16}$$

and

$$\eta = \frac{k}{\epsilon}\sqrt{2S_{ij}.S_{ij}} \tag{7.17}$$

where η_0 = 4.377 and β = 0.012. To calculate the turbulent viscosity μ_t, initial inlet velocity fluctuating is supposed to be 5% of the mean inlet velocity V_{in} and the turbulent kinetic energy k at the inlet is calculated as follows

$$k = \frac{3}{2}(0.05V_{in})^2 \tag{7.18}$$

The turbulent dissipation rate ϵ was figured up by

$$\epsilon = C_{\mu}^{3/4}\frac{k^{3/2}}{l} \tag{7.19}$$

where C_μ is the constant and taken as 0.09. l shows the characteristic length, and it is set to be 20% of the nozzle width W_n. Finally, turbulent viscosity μ_t is calculated as follows:

$$\mu_t = \rho_L C_\mu \frac{k^2}{\epsilon} \tag{7.20}$$

It should be noted that all given model constant are derived explicitly in RNG procedure except β, which is derived from experiment.

7.2.4 Mesh Description and Calculation Conditions

One of the discretisation errors in the CFD simulation is caused by the discretisation of the solution domain, which includes insufficient mesh resolution. That is why turbulent flow calculations are strongly affected by computational mesh, especially in the zones of the high gradients in velocity. For this reason, a mesh independency test is carried out to verify the proper mesh using three different meshes whose properties were shown in Table 7.2.

Table 7.2: Properties of the different meshes

	Course mesh	**Middle mesh**	**Fine mesh**
Total mesh number	32,300	73,100	190,270
Minimum mesh size	100 μm	50 μm	25 μm
CPU time	1 day	2.5 days	4.5 days

Hexahedral structured grids, whose smallest meshes are located in the recirculation zone, are created using blockMesh utility of OpenFOAM and h-refinement, which is applied to make locally refinement. In this refinement method, additional points are inserted locally in the regions where high resolution is needed without disturbing the rest of the mesh. Figure 7.2 shows the structured middle mesh using 73,100 hexahedral cells

whose minimum cell size is 50 μm.

Figure 7.3 shows the measured and calculated mean velocities at $y = -1.5, -3.0, -6.0$ mm with the combinations of VOF/MR/RNG $k - \epsilon$ when P_{inj} was 0.22 MPa. The coarse mesh illustrated by black lines overestimates the mean stream velocity in the recirculation zone especially $x = 0\ 0.6$ mm, while middle mesh shown by blue and the fine mesh shown by green lines give almost identical results with the LDV measurement.

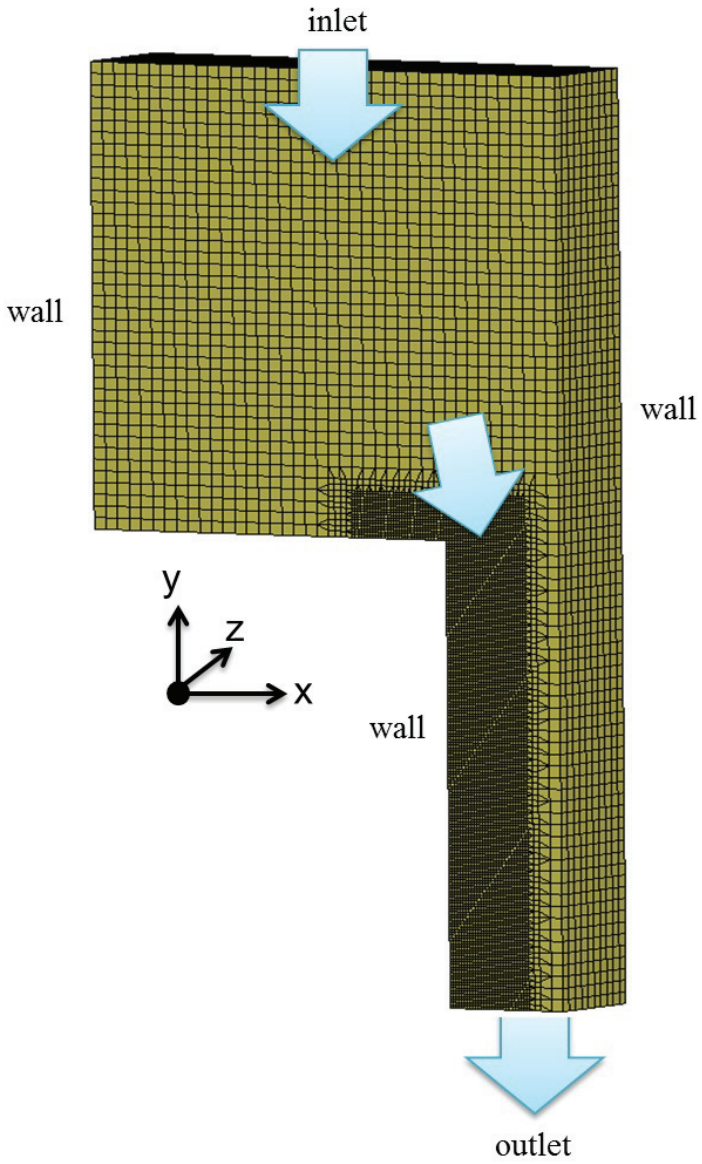

Figure 7.2: 3-D computational grid (middle mesh)

Figure 7.4 displays the comparison of the calculated liquid volume fraction α_L with three meshes at P_{inj} = 0.22 MPa. Since the cavitation region changes with the time, all the simulated results are taken from same time step and the central cross section in depth of the nozzle. As obtained, coarse mesh underestimates the cavitation length and

thickness, and also recirculation zone, while the middle and fine meshes give almost good predictions compared to the experiment. Figure 7.5 shows the measured and calculated mean cavitation lengths with different mesh sizes. As seen that, coarse mesh predicts the cavitation length around 60% error, whereas middle and fine mesh about 7-10%. In the view of these results and CPU time, middle mesh is chosen for the following numerical calculations.

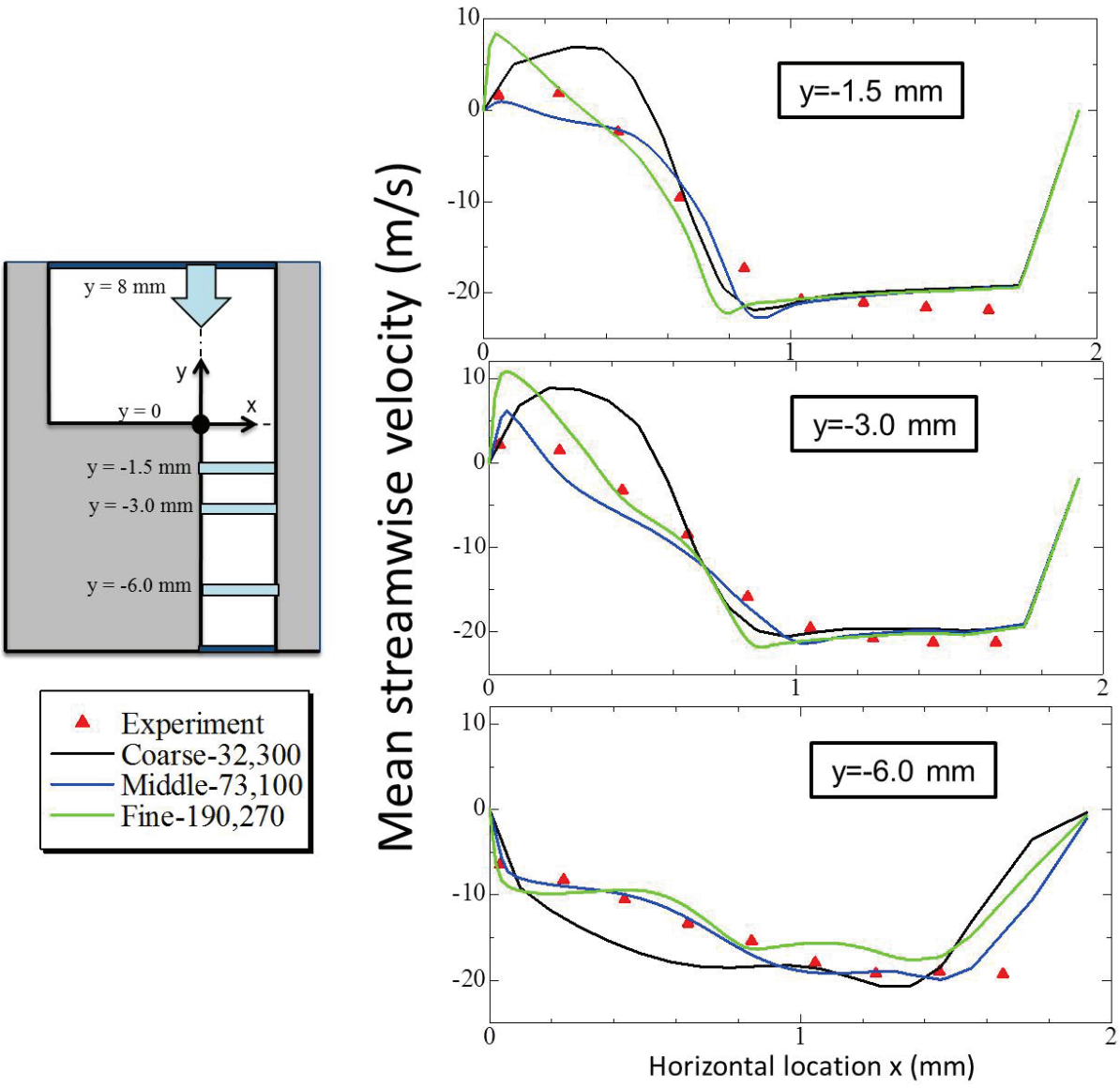

Figure 7.3: Measured and calculated mean velocities at P_{inj} = 0.22 MPa

An Intel Core i7 CPU X 980 @ 3.33 GHz X 6 core (each core has 2 threads), 12 GB RAM PC is employed for the calculations. Injection pressure P_{inj} is set to be 0.22 and 0.25 MPa, while outlet pressure P_{out} is fixed to the environment pressure as 0.1 MPa. At the nozzle walls, a no-slip condition is applied. The default wall functions provided by OpenFOAM are employed for the turbulent quantities k, ϵ, υ_t. The iterative PIMPLE

algorithm is used to solve pressure P and correct the mixture velocity **U** in the solver.

The second order linerUpwind scheme is chosen for the discretization of advection terms in the momentum Equation 7.8, while an implicit first order Euler scheme is used for the time integration. The advection term in the transport Equation 7.1 is discretised using van Leer scheme [114] without any artificial interface compression.

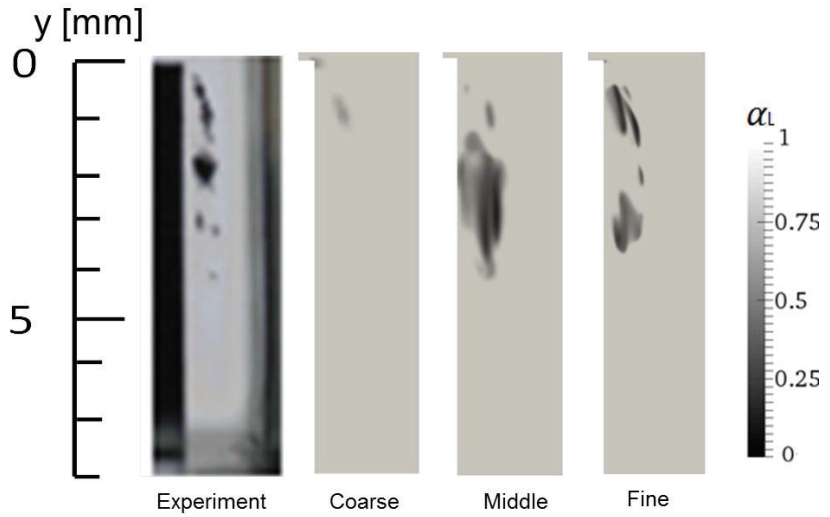

Figure 7.4: Calculated liquid volume fraction with different mesh sizes (P_{inj} = 0.22 MPa)

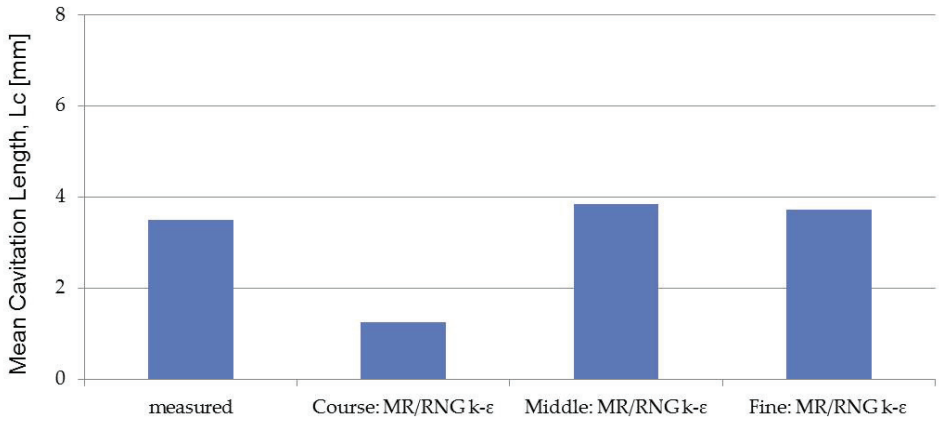

Figure 7.5: Measured and calculated mean cavitation lengths with different mesh sizes (P_{inj} = 0.22 MPa)

The first order upwind scheme is used for the discretisation of the convection terms of the turbulence parameters due to stability reasons. Time step $\triangle t$ and the maximum Courant number are set to be 10^{-8} s and 0.1, respectively. Each calculations takes approximately 2.5 days.

As a liquid, water, whose physical properties were given in Table 7.3, is used both in the experiment and numerical calculations. The saturation pressure P_V(=2.3 kPa) is

taken as the threshold of the cavitation for R model, while P_C is set to be -31.8 kPa and -33.2 kPa (calculated according to Equation 3.12) for the MR model at P_{inj} 0.25 MPa and 0.22 MPa, respectively. Since the simulations are isothermal, these properties are constant throughout the calculations.

Simulations are run in the non-cavitating condition for about 15 ms by increasing the inlet velocity slowly until the initial flow fields of fully developed turbulent flows are obtained. After that, the cavitation model is activated to simulate cavitation as depicted in Figure 7.6.

Table 7.3: Fluid properties

	density, $\rho(kg/m^3)$	**viscosity,** $\mu(Pa.s)$
Liquid (water)	998.2	1.00x10^{-3}
vapour	1.73x10^{-2}	1.00x10^{-6}

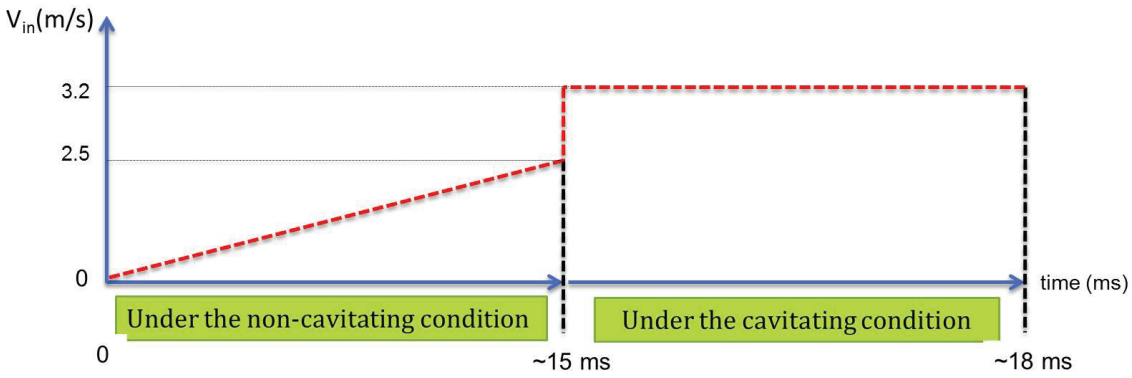

Figure 7.6: Solution methodology

7.3 Results and Discussion

Figure 7.7 and Figure 7.8 show the instantaneous results of R/RNG $k-\epsilon$ and MR/RNG $k-\epsilon$ models at P_{inj} = 0.22 MPa (σ=1.19) and P_{inj} = 0.25 MPa (σ=0.94), respectively. Results are illustrated in terms of liquid volume fraction α_L, pressure contours P and velocity vectors, which are taken at the middle plane in depth of the nozzle.

As seen in Figure 7.7 (a) and Figure 7.8 (a), R equation over-estimates the cavitation region from the points of cavity length and thickness since cavitation takes place when the local pressure is less than the vapour saturation pressure P_V instead of critical pressure P_C.

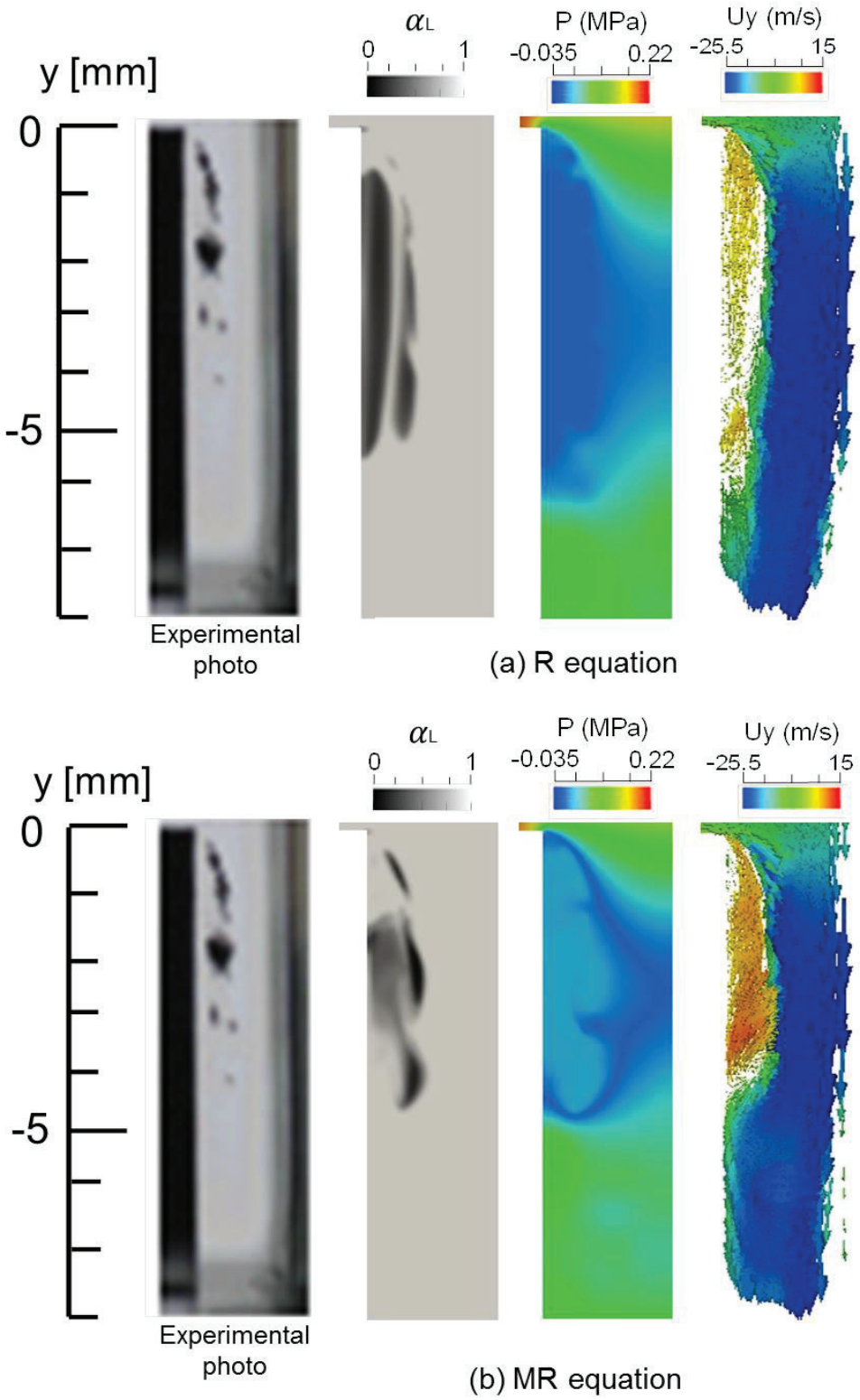

Figure 7.7: Calculated cavitating flows with (a) R Equation and (b) MR Equation (P_{inj} = 0.22 MPa)

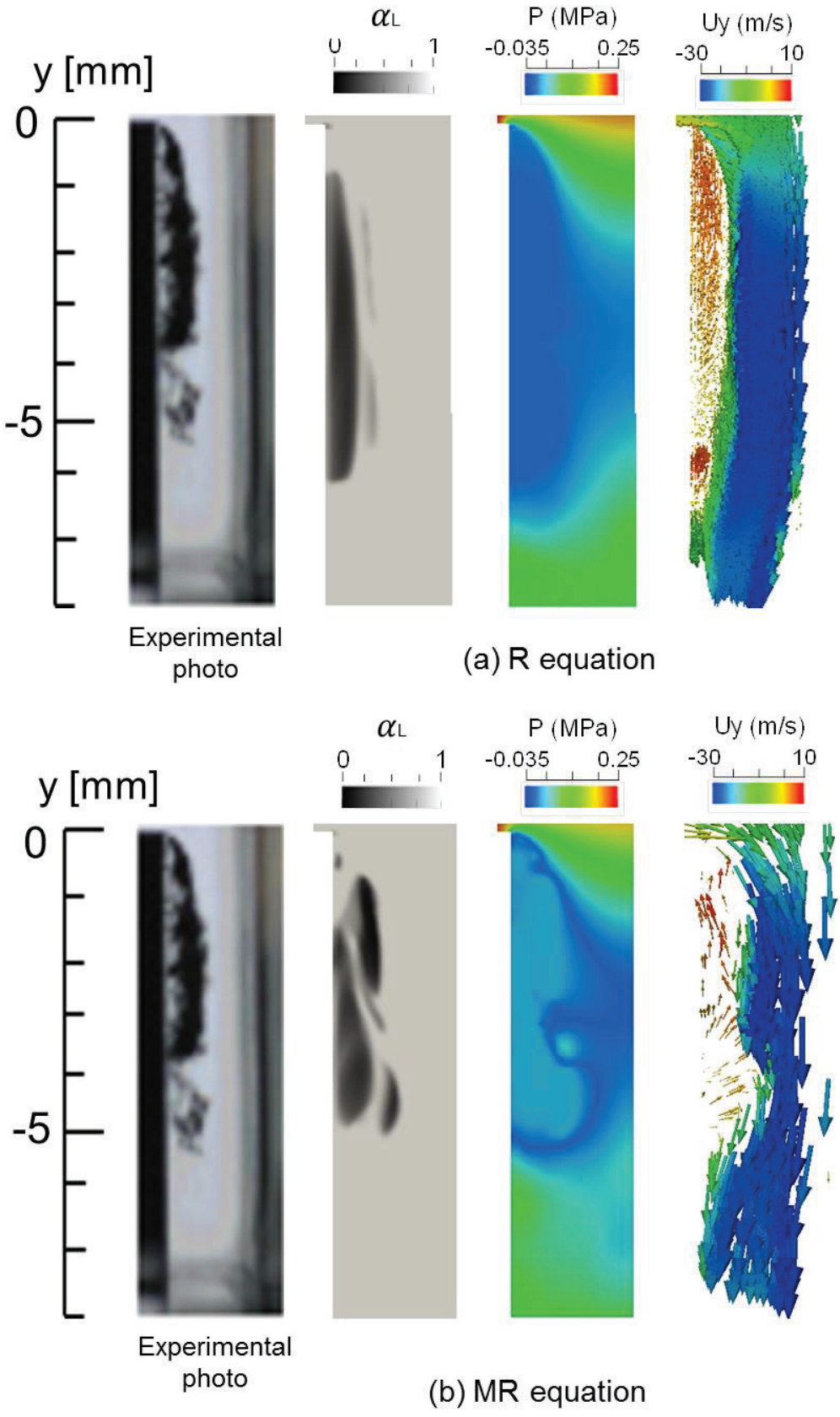

Figure 7.8: Calculated cavitating flows with (a) R Equation and (b) MR Equation (P_{inj} = 0.25 MPa)

On the other hand, MR equation based on the critical pressure P_C gives better estimation in the sense of cavity length and thickness when compared to R equation, as shown in Figure 7.7 (b) and Figure 7.8 (b).

The over-prediction of R equation can also be seen in Figure 7.9, which illustrates the time-averaged mixture density distributions in same time period calculated by R and MR equations when P_{inj} = 0.22 MPa. These distributions were taken at vertical distance y= -1.0, 3.0 and -4.5 mm from the entrance of the nozzle, respectively. The time-averaged mixture density was calculated according to Equation 7.2. As observed, model with R equation predicts that cavitation starts much earlier in comparison with MR equation due to using P_V. To be more accurate at y=-1.0 mm and -4.5 mm, model based on R equation observed that cavitation starts x=0.0 mm for both distance, while MR equation predicts a value of x=0.42 and 0.45 mm, respectively. Experimental data gives a value of x=0.40 mm and 0.42 mm.

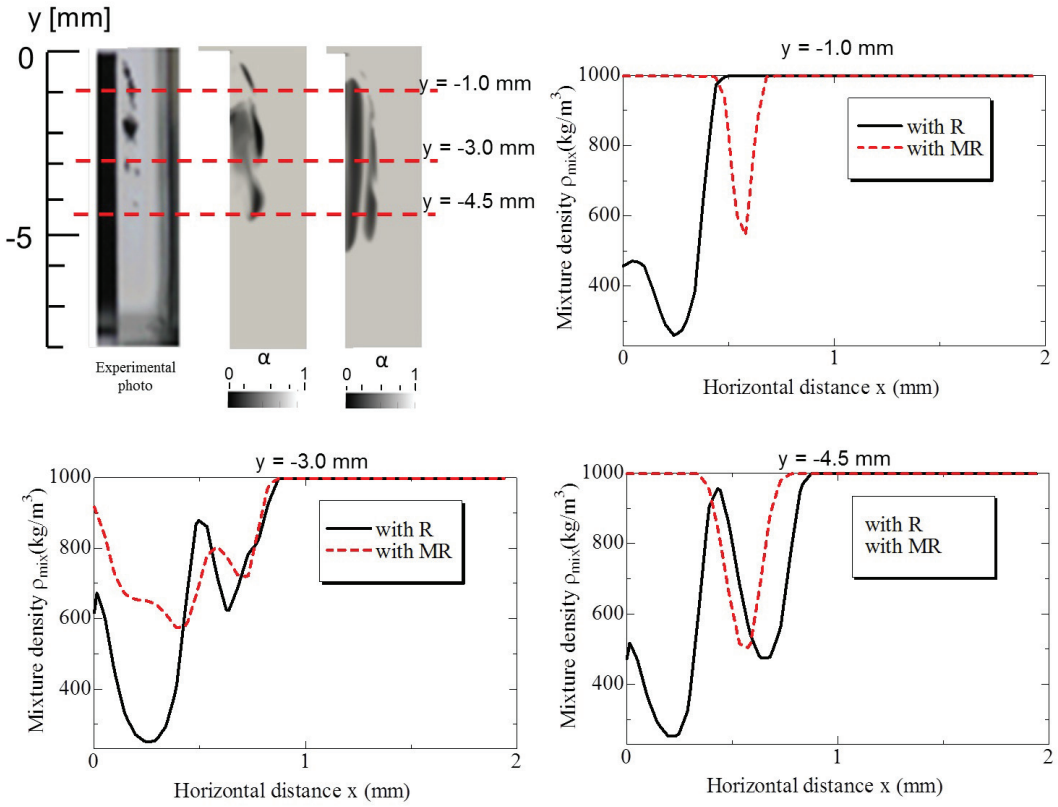

Figure 7.9: Time-average density distribution over different sections of the nozzle obtained with R equation and MR equation (P_{inj} = 0.22 MPa)

This can be clearly seen in the Figure 7.10, which shows measured and calculated mean cavitation lengths with MR/RNG $k-\epsilon$ and R/RNG $k-\epsilon$ models. As seen that

R model gives over prediction for the cavitation length whereas MR model gives well prediction with small error. Therefore, we conclude that MR model gives better prediction for cavitation.

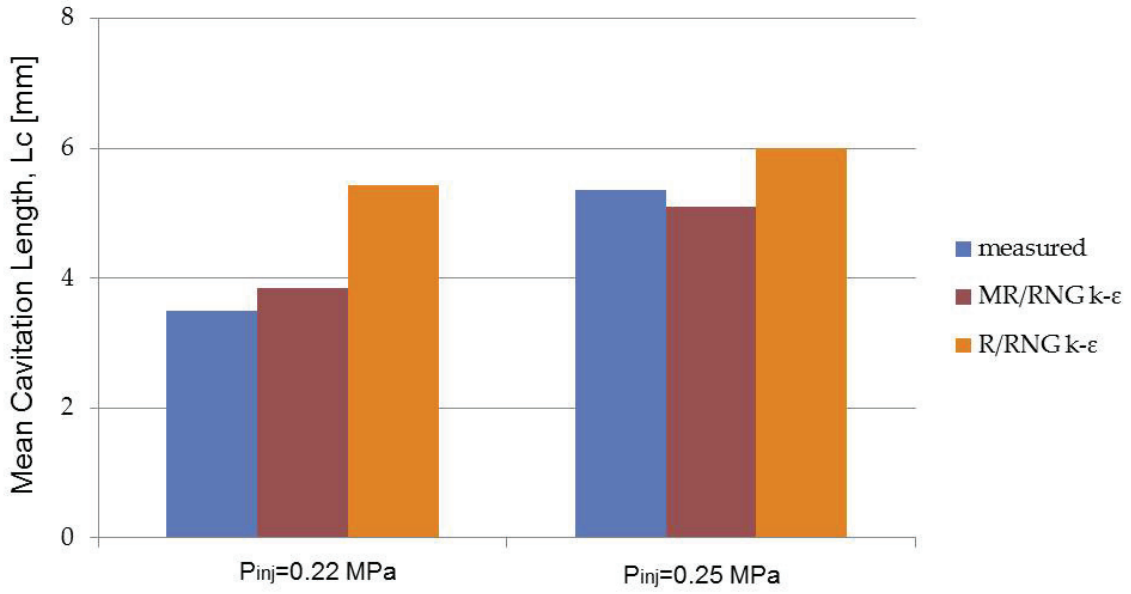

Figure 7.10: Measured and calculated mean cavitation lengths with MR/R equations at different conditions

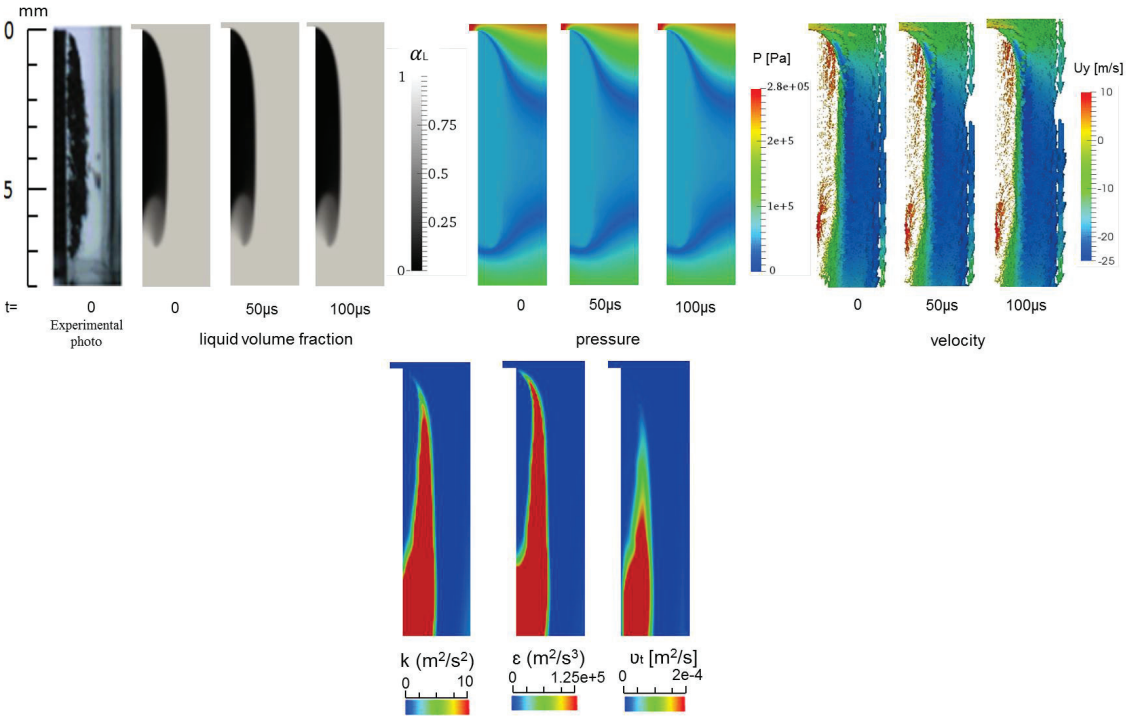

Figure 7.11: Calculated results with MR Equation at P_{inj} = 0.28 MPa

Figure 7.11 also shows the supercavitation case calculated with the combination of MR/RNG $k-\epsilon$ models. The results of liquid volume fraction, pressure, velocity and

turbulence model parameters are taken from the central cross section in depth of the nozzle when P_{inj} is 0.28 MPa. As seen, even though supercavitation inside nozzle is slightly underestimated, a good prediction is obtained by proposed MR model.

7.3.1 Transient Cavitation in Nozzle

Figure 7.12 shows experimental high speed images of transient cavitation and calculated cavitation flows using MR equation and RNG $k-\epsilon$ for P_{inj} = 0.22 MPa. Figure 7.12 (a) was taken using the high speed camera whose time internal was 50 μs. In the low pressure zones within the recirculation region, a huge number of nuclei grew and vortices are shed from the reattachment point. The vortex accompanied by clouds of bubbles is shed and the bubbles collapse during the shedding. The phenomena are well simulated with MR model and agreed quite satisfactorily with the high speed image. Figure 7.13 also confirms the validation of the proposed MR model, which displays a good agreement in the prediction of cavitation cloud shedding with the combination of MR and RNG $k-\epsilon$ when P_{inj} was 0.25 MPa.

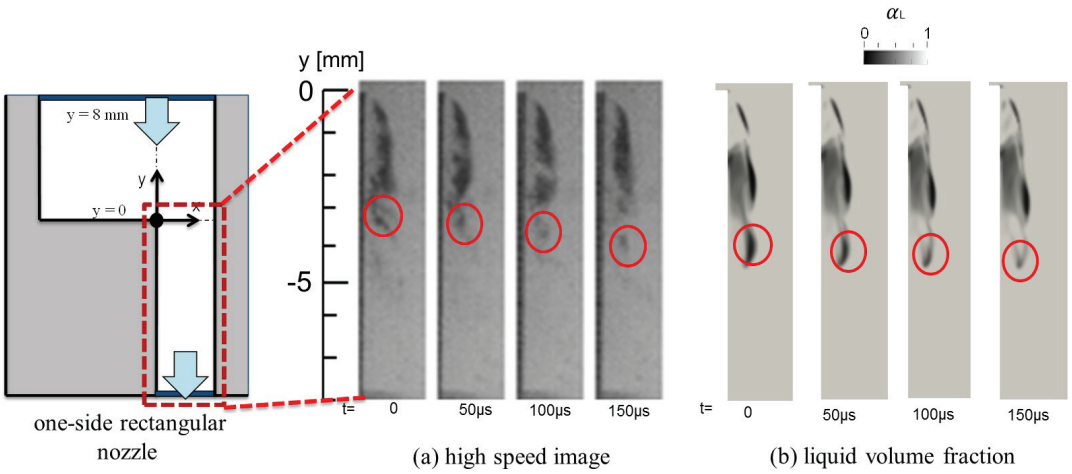

Figure 7.12: Transient cavitation motion with (a) high speed image (b) MR equation (P_{inj} = 0.22 MPa)

Figure 7.14 illustrates a sequence of cavitation cycle with velocity vectors distributions that are taken at the middle plane in depth of the nozzle. These results are obtained using the combination of MR and RNG $k-\epsilon$ when P_{inj} 0.22 MPa. The cycle begins with the small development of cavitation near the entrance of the nozzle due to sharp edge frame (a), which is called incipient cavitation. Then, cavity moves downstream and develops through the middle of the nozzle between the frames (b) and (f). The re-entrant jet induces

vortex shedding (f) and shortens the cavity among the frames (g)-(j). Finally, new cycle starts with the development of small cavity at the entrance of the nozzle, frames (k) and (l). It should be noted that due to using of RANS, the prediction of reverse flow structures and observation of the cloud shedding moving until the exit of the nozzle are limited compared to Large Eddy Simulations (LES).

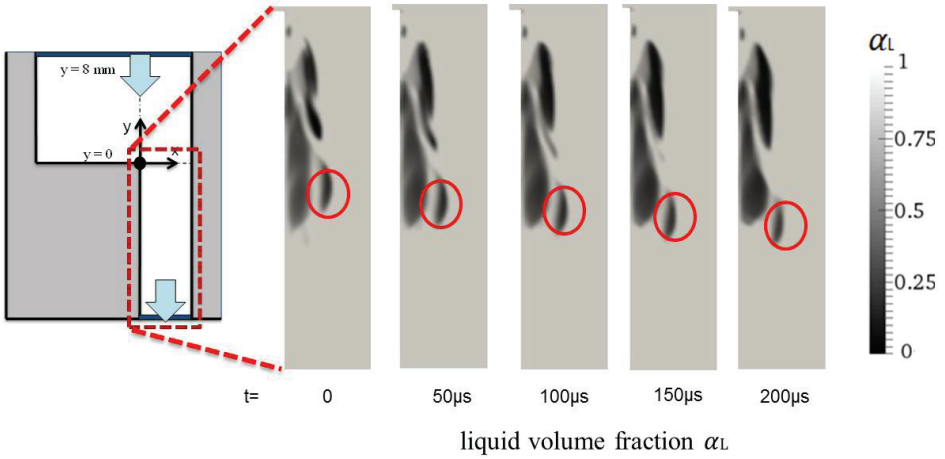

Figure 7.13: Transient cavitation motion obtained with MR equation (P_{inj} = 0.25 MPa)

7.4 Summary

In this Chapter, the feasibility and applicability of the proposed Modified Rayleigh (MR) equation based on critical pressure P_C is presented in CFD to precisely predict the cavitation region and its cloud shedding inside a nozzle. To verify the validity of the proposed model, results are compared with the conventional cavitation model based on R equation, which uses P_V as a threshold of cavitation, and experimental data.

It is found out that R equation over-estimates cavitation region from the points of cavity length and thickness, while MR equation based on the critical pressure P_C gives better estimation in the sense of cavity length and thickness for all cases. The transient motion of cavitation in the recirculation zone, such as cloud shedding, the development of the re-entrant jet and the cavity break-off is well predicted with the combination of MR and RNG $k-\epsilon$. This approach is easy to be employed and applied for cavitation simulation inside nozzle since it does not need very fine grid, and therefore it has a short CPU time.

As a final comment, it can be stated that the combination of VOF, MR and RNG $k-\epsilon$ model with a proper mesh gives a fairly good prediction and can be used to obtain an insight into cavitation phenomena within a fuel injector.

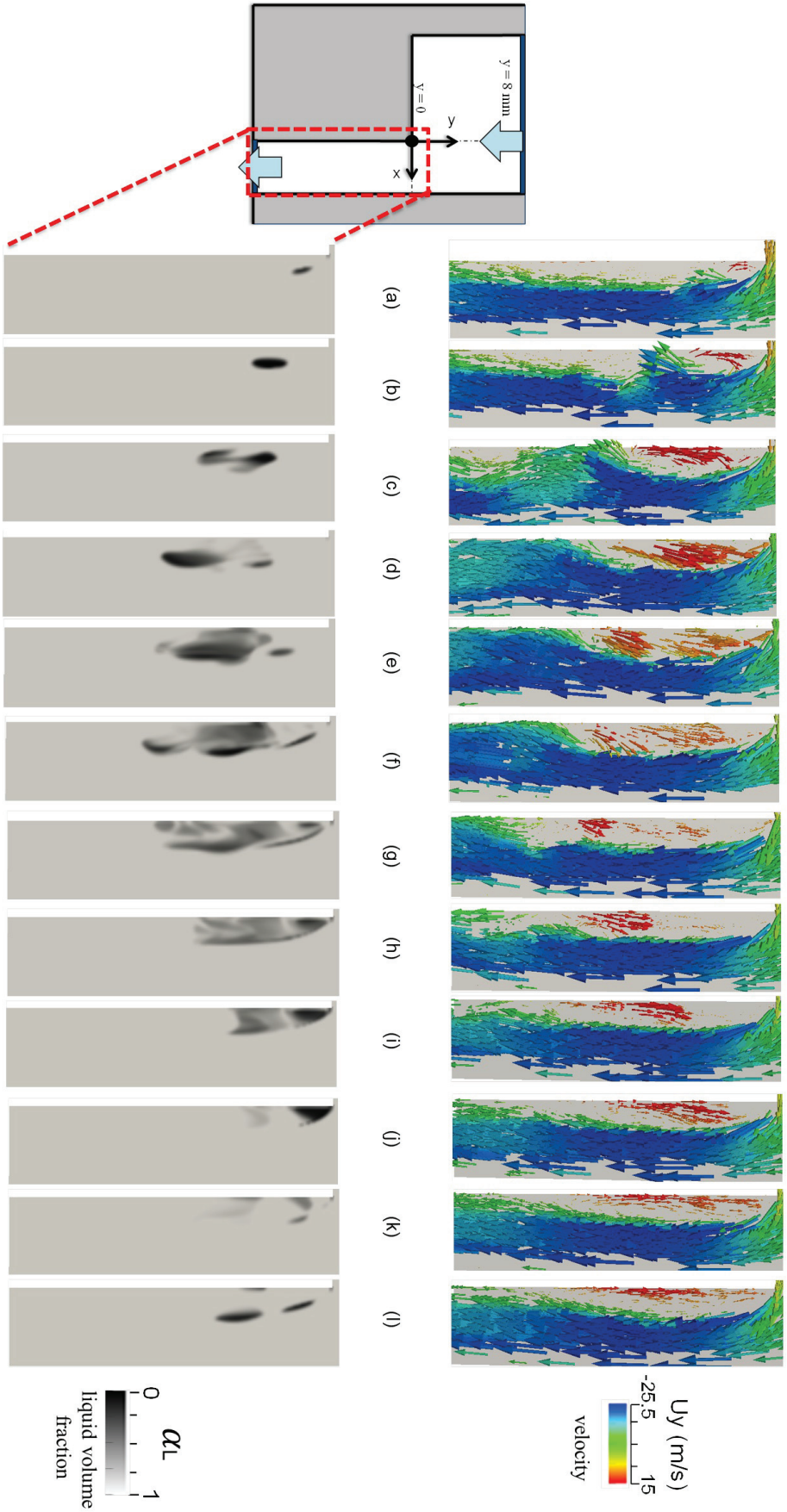

Figure 7.14: Sequence of cavity cycle(P_{inj} = 0.22 MPa, results are shown every 0.5 ms)

Chapter 8

Effects of Turbulence Model on Turbulent Cavitation Flow

8.1 Introduction

This Chapter presents applicability of Modified Rayleigh equation with various turbulence models to the turbulent cavitating flows in a rectangular nozzle whether we can simulate cavitation cloud shedding process captured by a high-speed camera or not and can quantitatively predict the cavitation length and thickness. OpenFOAM is used for the numerical calculations of turbulent cavitating flows.

The two-equation turbulence models within the framework of RANS, such as $k-\omega$ SST and RNG $k-\epsilon$ models with various meshes of different cell sizes and one equation eddy viscosity sub-grid scale model under the framework of Large Eddy Simulation (LES) are tested to simulate the turbulent cavitation flow, whose liquid velocity was measured by Laser Doppler Velocimetry (LDV).

Table 8.1 displays the summary of the model combinations which are used within this chapter. The results of first combination with RNG $k-\epsilon$ model have been already illustrated in the previous Chapter 7 using various meshes of different cell sizes. As obtained, the combination of the MR/RNG $k-\epsilon$ model with a fine mesh of about 25 - 50 μm in the minimum mesh size Δx_{min} is able to capture the transient motion of cavitation in the recirculation zone, such as cloud shedding, the development of the re-entrant jet and the cavity break-off. Therefore, in this chapter, the model equations of $k-\omega$ SST and LES models are given, and finally the comparisons of the three different turbulence models and their results are presented.

Table 8.1: Summary of the combined models

	Multiphase Modelling	**Cavitation Modelling**	**Bubble Dynamics**	**Turbulence Model**	**CFD Tool**
1.	Simplified VOF	Schnerr-Sauer	MR	RNG $k-\epsilon$	OpenFOAM
2.	Simplified VOF	Schnerr-Sauer	MR	$k-\omega$ SST	OpenFOAM
3.	Simplified VOF	Schnerr-Sauer	MR	LES	OpenFOAM

8.2 The Combination of MR / $k-\omega$ SST model

8.2.1 $k-\omega$ SST Model

The $k-\omega$ SST (Shear Stress Transport) formulation is based on the two-equation eddy-viscosity model within RANS application which was proposed by Menter and Florian [115]. In this model, the turbulent kinetic energy k and the specific turbulent dissipation rate ω equations are given as follows:

$$\frac{(\partial\rho_L k)}{\partial t}+\frac{\partial(\rho_L u_j k)}{\partial x_j}=P_k^*-\beta^*\rho_L k\omega+\frac{\partial}{\partial x_j}\left[(\mu_{eff}+\sigma_k\mu_t)\frac{\partial k}{\partial x_j}\right] \tag{8.1}$$

$$\begin{aligned}\frac{(\partial\rho_L \omega)}{\partial t}+\frac{\partial(\rho_L u_j \omega)}{\partial x_j}=&\alpha\rho_L S^2-\beta\rho_L\omega^2+\frac{\partial}{\partial x_j}\left[(\mu_{eff}+\sigma_\omega\mu_t)\frac{\partial\omega}{\partial x_j}\right]\\&+2(1-F_1)\sigma_{\omega 2}\frac{1}{\omega}\frac{\partial k}{\partial x_i}\frac{\partial\omega}{\partial x_i}\end{aligned} \tag{8.2}$$

where the blending function F_1 is described by:

$$F_1=tanh\left\{\left\{min\left[max\left(\frac{\sqrt{k}}{\beta^*\omega y},\frac{500\nu}{y^2\omega}\right),\frac{4\rho\sigma_{\omega 2}k}{CD_{k\omega}y^2}\right]\right\}^4\right\} \tag{8.3}$$

where y shows the distance nearest to wall and $CD_{k\omega}$ is given by:

$$CD_{k\omega}=max\left(2\rho\sigma_{\omega 2}\frac{1}{\omega}\frac{\partial k}{\partial x_i}\frac{\partial\omega}{\partial x_i},10^{-10}\right) \tag{8.4}$$

It should be noted that blending function F_1 corresponds to zero far from the surface ($k-\epsilon$ model), and switches over the to one within the boundary layer ($k-\omega$ model). The

turbulent eddy viscosity is calculated as follows:

$$\nu_t = \frac{a_1 k}{max(a_1\omega, SF_2)} \tag{8.5}$$

where S is rate of strain tensor whereas F_2 is a second blending function and identified by:

$$F_2 = tanh\left\{\left[\left(\frac{\sqrt{k}}{\beta^*\omega y}, \frac{500\nu}{y^2\omega}\right)\right]^2\right\} \tag{8.6}$$

In $k-\omega$SST model, a production limiter P_k^* is employed as indicated in Equation 8.1 in order to hinder the build-up of turbulence in the stagnation areas:

$$P_k = \mu_t \frac{\partial u_i}{\partial x_j}\left(\frac{\partial u_i}{\partial x_j} + \frac{\partial u_j}{\partial x_i}\right) \tag{8.7}$$

where P_k^* equals to:

$$P_k^* = min\left(P_k, 10\beta^* k\omega\right) \tag{8.8}$$

All constants of the model are calculated as a linear combination of the corresponding coefficients of the underlying models:

$$\alpha = \alpha_1 F_1 + \alpha_2(1 - F_1) \tag{8.9}$$

The model constants are: $\beta^* = 0.09$, $\alpha_1 = 5/9$, $\alpha_2 = 0.44$, $\beta_1 = 3/40$, $\beta_2 = 0.0828$, $\sigma_{k1} = 0.85$, $\sigma_{k2} = 1$, $\sigma_{\omega 1} = 0.5$, $\sigma_{\omega 2} = 0.856$ and $a_1 = 0.31$. To calculate the initial boundary conditions of k and ω at the inlet, the velocity fluctuating is supposed to be 5% of the mean inlet velocity V_{in} and the turbulent kinetic energy k at the inlet is calculated as follows

$$k = \frac{3}{2}(0.05V_{in})^2 \tag{8.10}$$

The specific turbulent dissipation rate ω is figured up by

$$\omega = C_\mu^{-1/4}\frac{\sqrt{k}}{l} \tag{8.11}$$

where C_μ is the constant and taken as 0.09. l shows the characteristic length, and it is set to be 20% of the nozzle width W_n.

8.2.2 Mesh Description and Calculation Conditions

Since the turbulent flow calculations are strongly affected by computational mesh, especially in the zones of high velocity gradient, a mesh independency test are carried out for $k-\omega$ SST model calculations to determine the proper mesh number using three different mesh sizes as indicated in Table 8.2.

Table 8.2: Properties of the different meshes

	Course mesh	**Middle mesh**	**Fine mesh**
Total mesh number	73,100	228,320	621,020
Minimum mesh size	50 μm	25 μm	12.5 μm
CPU time	2.5 day	5 days	10 days

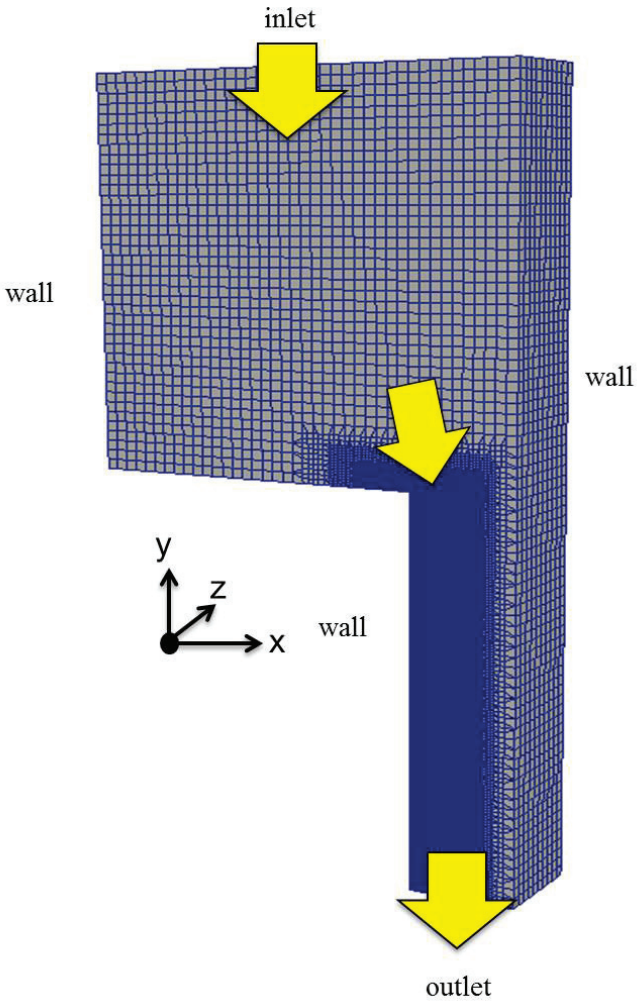

Figure 8.1: 3-D computational grid (middle mesh)

Uniform hexahedral structured grids, whose smallest meshes were located in the recirculation zone, are created using blockMesh and refineMesh utilities of OpenFOAM. Figure 8.1 shows the uniform structured middle mesh with 228,320 hexahedral cells whose minimum cell size is 25 mum.

Figure 8.2 displays the measured and calculated mean velocities at y = -1.5, -3.0, -6.0 mm with the combination of MR/$k-\omega$ SST model when P_{inj}=0.22 MPa. The coarse mesh illustrated by black lines overestimates the mean stream velocity in in the recirculation zone especially x=0.6 2 mm, while middle mesh shown by blue and the fine mesh shown by green lines give almost identical results with the LDV measurement.

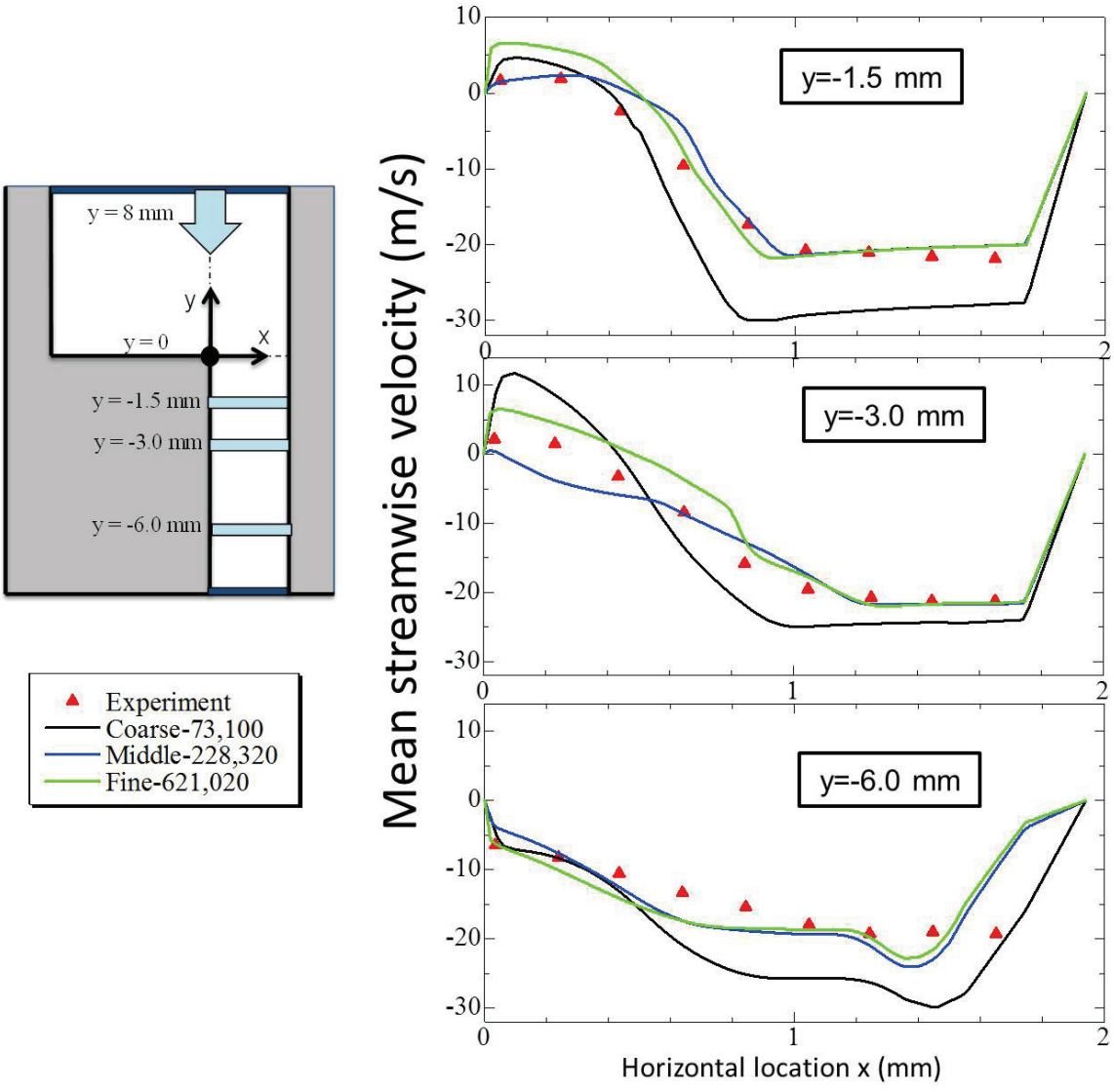

Figure 8.2: Measured and calculated mean velocities with MR/$k-\omega$ SST at P_{inj} = 0.22 MPa

Figure 8.3 shows the comparison of the calculated liquid volume fraction α_L with

three meshes at at P_{inj} = 0.22 MPa. Since the cavitation region changes with the time, all the simulated results are taken from same time step and from the central cross section in depth of the nozzle.

As obtained, the coarse mesh underestimates the cavitation length and thickness, and also recirculation zone, while the middle and fine meshes give almost good predictions compared to the experiment. Also, the coarse mesh close the nozzle wall results in smearing the results and gives wrong attached cavitation on the wall. Addition to this, Figure 8.4 shows the measured and calculated mean cavitation lengths with different mesh sizes. As seen that, coarse mesh predicts the cavitation length with around 40% error, whereas middle and fine mesh about with 8-12% error. In the view of these results and CPU time, middle mesh, which is shown in Figure 8.1 and inserted 40 cells with 25 μm size in Δx_{min} in the recirculation zone, is chosen for next numerical calculations.

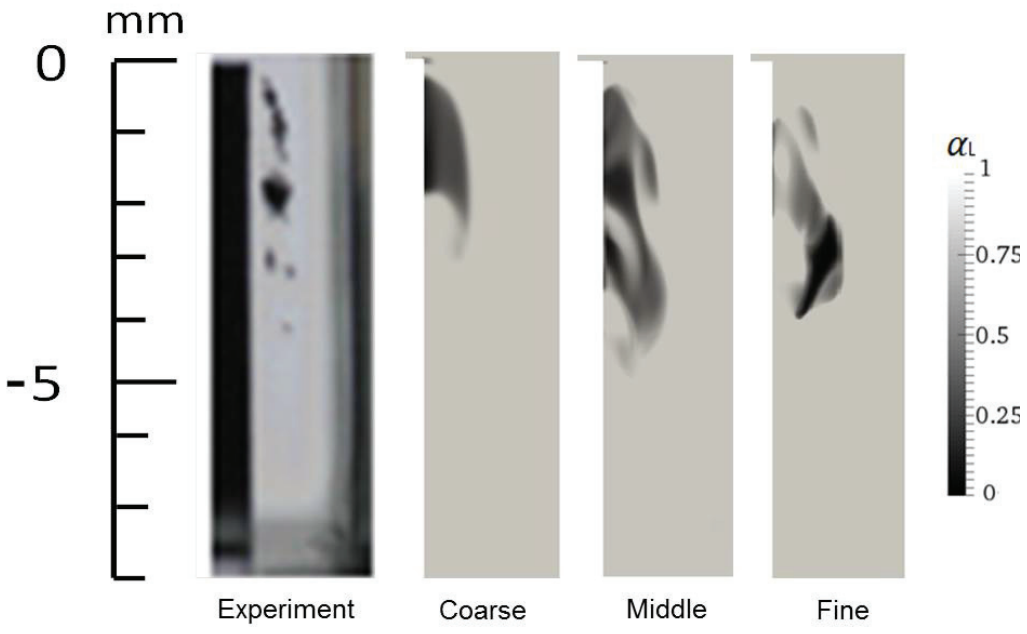

Figure 8.3: Calculated liquid volume fraction α_L with different mesh sizes at P_{inj} = 0.22 MPa

An Intel i7 CPU X 980 @ 3.33 GHz x 6 core (each core has two threads), 12 GB RAM PC is employed for the calculations. Injection pressure P_{inj} is set to be 0.22 MPa, while outlet pressure P_{out} is fixed to the environment pressure as 0.1 MPa. At the nozzle walls, a no-slip condition is applied. The iterative PIMPLE algorithm is used to solve pressure P and correct the mixture velocity **U** in the solver.

The advection term in the transport is discretised using van Leer scheme without any

Figure 8.4: Measured and calculated mean cavitation lengths with different mesh sizes at P_{inj} = 0.22 MPa

artificial interface compression. Time step Δt and the maximum Courant number are set to be 10^{-8} s and 0.1, respectively. As a liquid, water is used both in the experiment and numerical calculations.

Simulations are run in the non-cavitating condition for about 15 ms until the initial flow fields of fully developed turbulent flows are obtained. After that, the cavitation model is activated to simulate cavitation as already illustrated and explained in Figure 7.6.

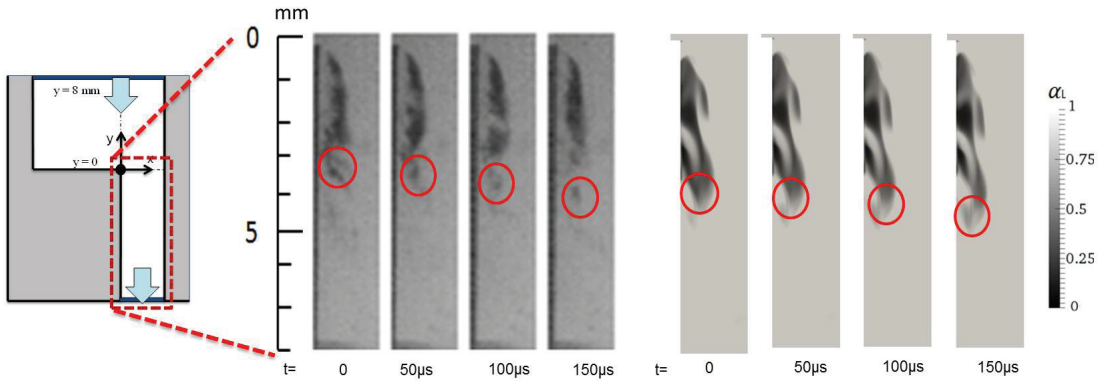

Figure 8.5: Transient cavitation motion with (a) high speed image (b) MR/$k-\omega$ SST (P_{inj} = 0.22 MPa)

8.2.3 Results and Discussion

Figure 8.5 shows experimental high speed images of transient cavitation and calculated cavitating flows with MR equation and $k-\omega$ SST model for P_{inj} = 0.22 MPa. Figure 8.5 (a) was taken using the high speed camera whose time internal was 50 μs. In the low pressure zones within the recirculation region, a huge number of nuclei grew and vortices

are shed from the reattachment point. The vortex accompanied by clouds of bubbles is shed and the bubbles collapse during the shedding. The phenomena is well simulated with MR and $k-\omega$ SST turbulence model using 228,320 meshes, where minimum mesh size Δx_{min} 25 μm, and results were agreed quite satisfactorily with the high speed image.

8.3 LES Model (One Equation Eddy Viscosity Model)

The main idea in LES modelling is to resolve the large-scale turbulent motion in order to model the small scale eddies, which are more common. This situation can be defined as an energy cascade concept, which explains the turbulence energy transfer from large-scale eddies to smaller scales until they are dissipated into heat by viscosity at the molecular level. Therefore, it is main principal in LES first to resolve the turbulent energy of the large eddies, and then use a sub-grid scale(SGS) model to represent small scale eddies.

8.3.1 Model Equations

Basic filtered mass and momentum conservation equations for incompressible turbulent liquid flow have been already given in section 6.2.2. Addition to this, in the modelling of the one equation eddy viscosity model for incompressible flow, one more balance equation is solved to simulate the behaviour of turbulent kinetic energy k, where it is given

$$\frac{\partial k}{\partial t} + \nabla \cdot (\mathbf{U}k) - \nabla \cdot (\mu_{eff} \nabla k) = -S : B - C_e \frac{k^{3/2}}{\triangle} \tag{8.12}$$

where C_e is the model parameter and given 1.048, while $\triangle$ is the cell volume. ":" corresponds to double dot product of the second rank of S and B tensors, which produces a scalar. Tensors B and S are given as,

$$B = \frac{2}{3} kI - \nu_{sgs} dev(S) \tag{8.13}$$

$$S = symm(\nabla U) = \frac{1}{2}[\nabla U + (\nabla U)^T] \tag{8.14}$$

respectively. In Equation 8.2, I indicates identity tensor and is given

$$I = \begin{pmatrix} 1 & 0 & 0 \\ 0 & 1 & 0 \\ 0 & 0 & 1 \end{pmatrix}.$$

whereas "dev" represents deviatoric operator that manipulates the tensor S, and it is given

$$dev(S) = S - \frac{1}{3}(trS)I \tag{8.15}$$

where "tr" shows the trace of tensor S which was evaluated by summing the diagonal components. Sub-grid scale viscosity is calculated as

$$\nu_{sgs} = C_k\sqrt{k}\triangle \tag{8.16}$$

where C_k is model constant and taken as 0.094. Finally, effective viscosity ν_{eff} is obtained as follow

$$\nu_{eff} = \nu_m + \nu_{sgs} \tag{8.17}$$

where ν_m shows molecular viscosity.

An hexahedral structured grid with small mesh 4.4 μm mesh is used to avoid the numerical error introduced by non-orthogonality, as well as LES filtering communication error.

The superiority of LES model versus to RANS are significant that can be seen in the results in terms of vortex shedding and unsteady separation.

8.3.2 Mesh Description and Calculation Conditions

Regarding to LES modelling, one equation eddy viscosity sub-grid scale (SGS) model, which has been already implemented into OpenFOAM, is used. For LES calculation, proper mesh number is determined by increasing mesh number gradually until the satisfied results are obtained due to low PC performance. The properties of chosen mesh are shown in Table 8.3.

Table 8.3: Properties of the proper mesh

	Total mesh number	**Min. mesh number**	**CPU time**
chosen mesh	2,082,520	4.4 μm	22 days

Mesh is created using uniform structured cells whose smallest cells are located in the recirculation zone using blockMesh and refineMEsh utilities of OpenFOAM. Figure 8.6 shows the uniform structured middle mesh with 2,082,520 hexahedral cells whose minimum cell size is 4.4 mum.

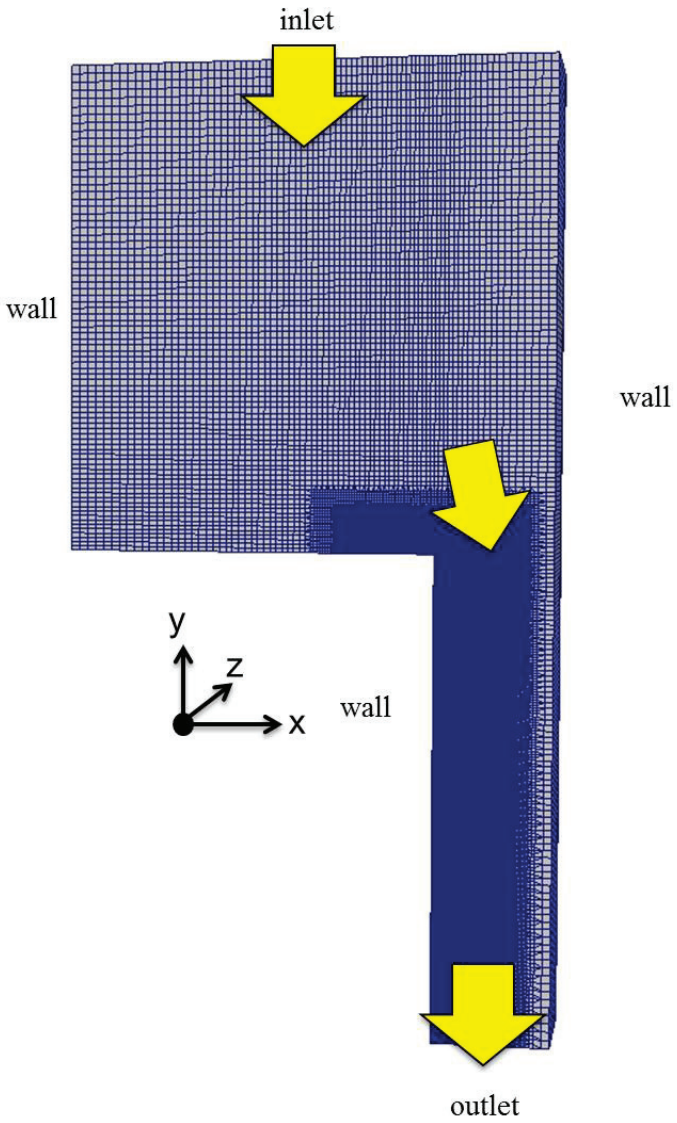

Figure 8.6: 3-D computational grid (chosen mesh)

An Intel i7 CPU X 980 @ 3.33 GHz x 6 core (each core has two threads), 12 GB RAM PC is employed for the calculations. Injection pressure P_{inj} is set to be 0.22, while outlet pressure P_{out} is fixed to the environment pressure as 0.1 MPa. At the nozzle walls, a no-slip condition is applied. An iterative PIMPLE algorithm is used to solve pressure P and correct the mixture velocity **U** in the solver.

The advection term in the transport is discretised using van Leer scheme without any artificial interface compression. Time step Δt and the maximum Courant number are set to be 10^{-8} s and 0.1, respectively. As a liquid, water is used both in the experiment and numerical calculations.

Simulations are run in the non-cavitating condition for about 15 ms until the initial

flow fields of fully developed turbulent flows are obtained. After that, the cavitation model is activated to simulate cavitation. The calculation takes almost 22 days.

8.3.3 Results and Discussion

Figure 8.7 displays the measured and calculated mean velocities at y = -1.5, -3.0, -6.0 mm with the combination of MR equation and LES model when P_{inj}=0.22 MPa. The calculated results with 2,082,520 hexahedral cells, whose minimum cell size is 4.4 μm, illustrated by black lines give almost identical results with the LDV measurement.

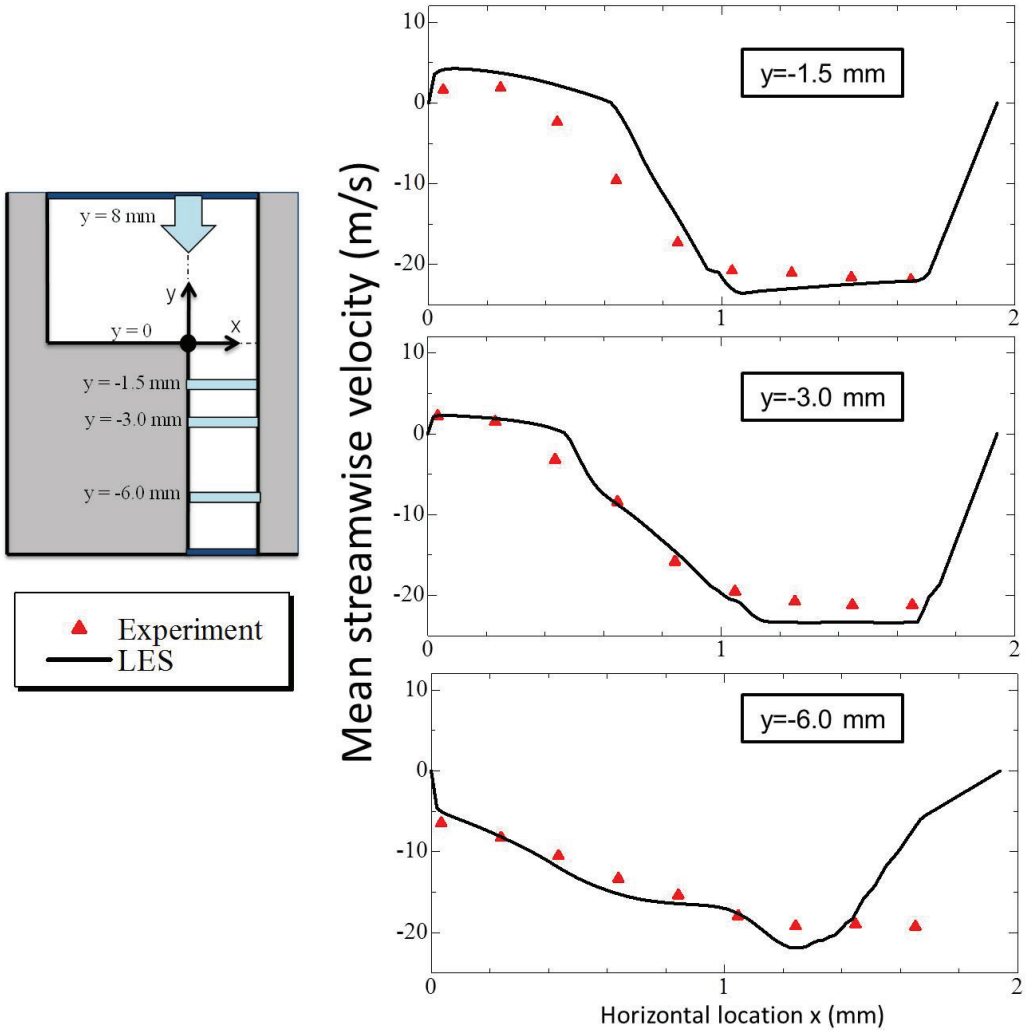

Figure 8.7: Measured and calculated mean velocities with MR/LES at P_{inj} = 0.22 MPa

Figure 8.8 shows high speed images of cavitation flow and calculated cavitation using the combination of MR equation and LES model at P_{inj}=0.22 MPa. The liquid volume fraction α_L, pressure contours P and vorticity contours are taken at the middle plane in

depth of the nozzle channel. The transient shedding of vortex accompanied by clouds is clearly predicted well compared to previous RANS model's results.

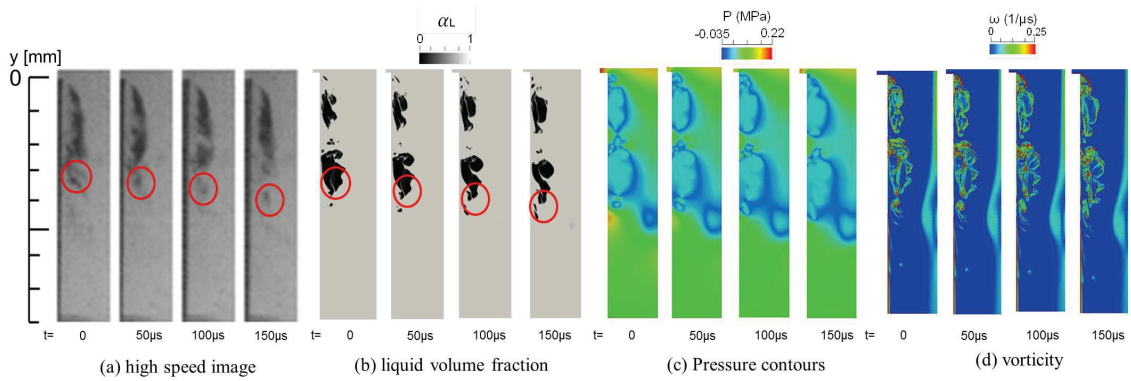

Figure 8.8: Transient cavitation motion with MR/LES (P_{inj} = 0.22 MPa)

Figure 8.9 shows measured and calculated mean cavitation lengths with the combination of MR/LES when P_{inj}=0.22 MPa. As obtained that cavitation length is well-predicted with 9% error using the combination of MR/LES model.

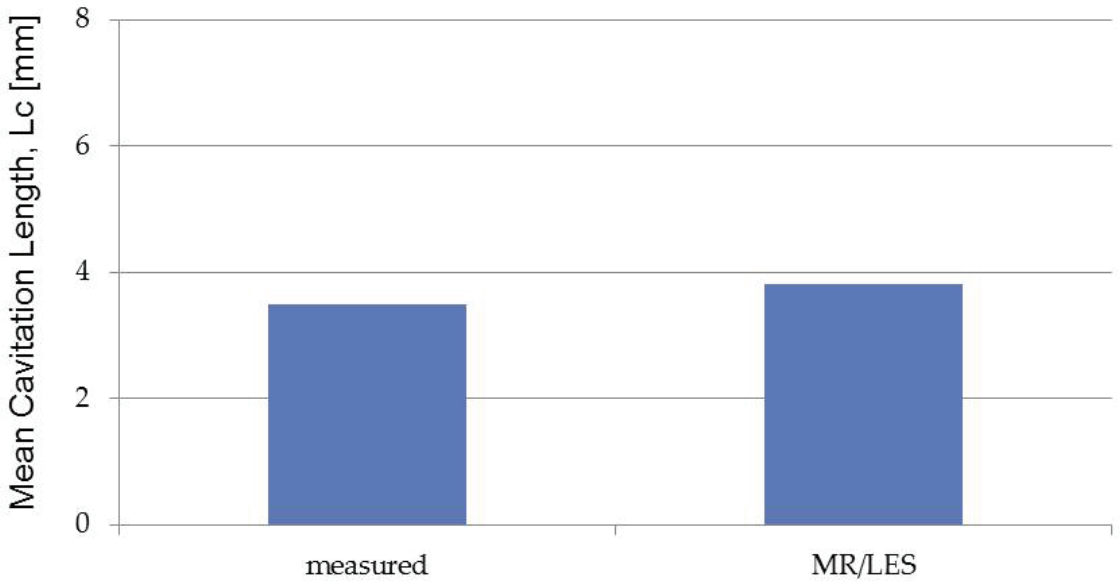

Figure 8.9: Measured and calculated mean cavitation lengths with MR/LES (P_{inj} = 0.22 MPa)

It should be noted that the transient motion of cavitation cloud shedding is monitored and well simulated down to exit of nozzle as indicated in Figure 8.10 by the combination MR/LES using 2,082,520 meshes, where 250 cells are inserted with minimum 4.4 μm size in Δx_{min} in the recirculation zone. The results are shown in every 0.25 ms.

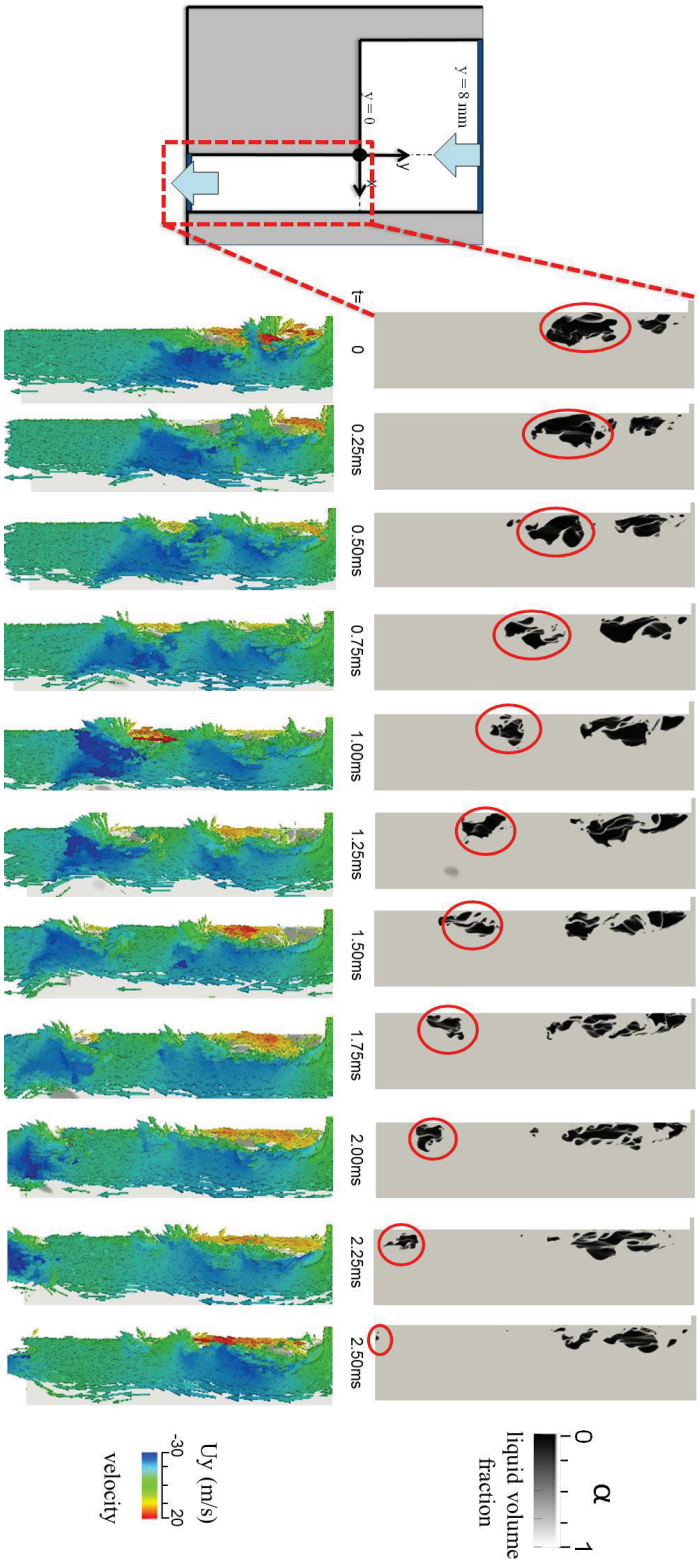

Figure 8.10: Transient cavitation cloud shedding with MR/LES (P_{inj} = 0.22 MPa)

8.4 Comparison of the Turbulence Models

Measured and calculated turbulence velocities at y = -1.5, -3.0, -6.0 mm for P_{inj} = 0.22 MPa are illustrated in Figure 8.11.

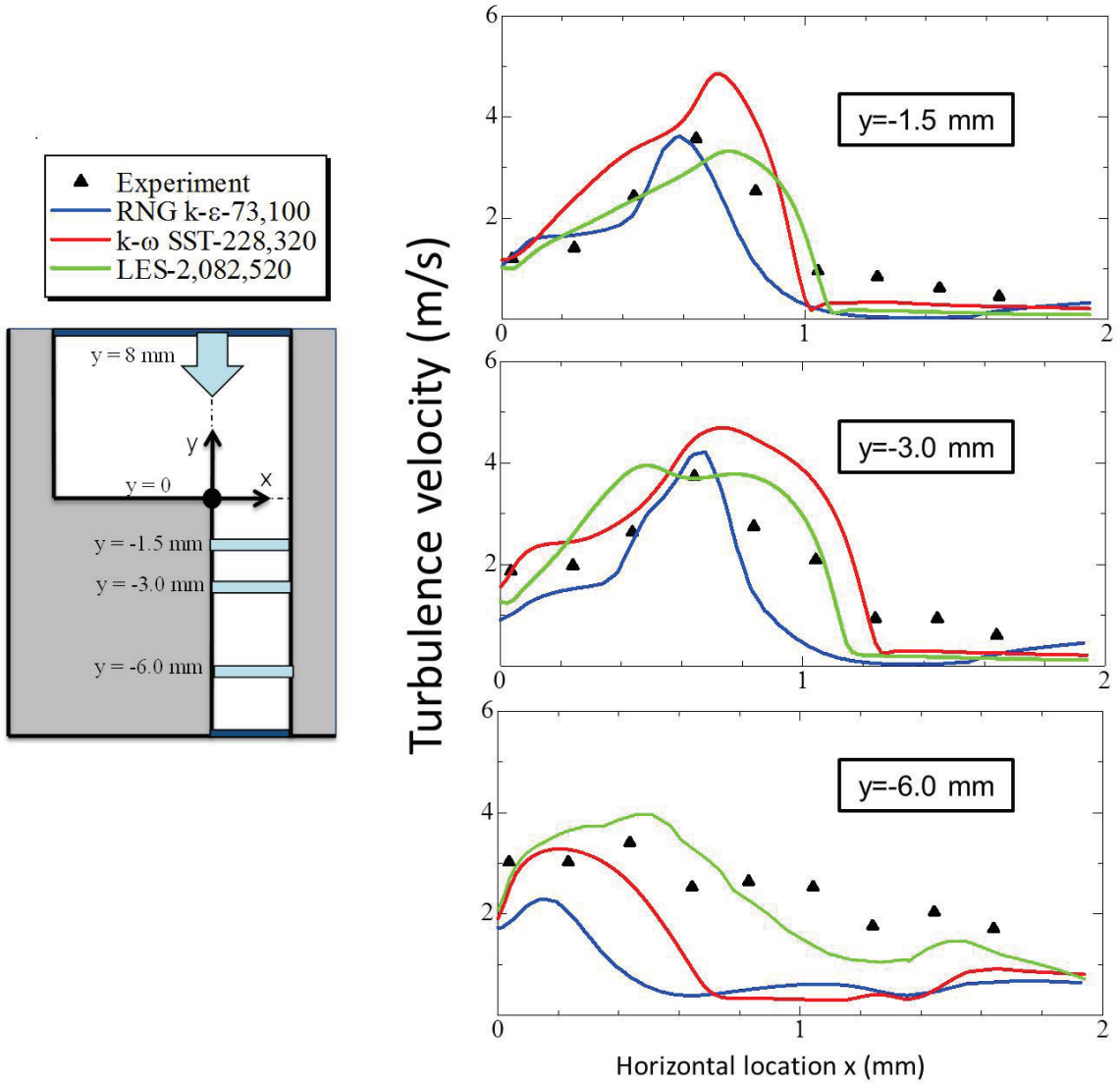

Figure 8.11: Measured and calculated turbulence velocities at (P_{inj} = 0.22 MPa)

The results calculated by RNG $k-\epsilon$ model were shown in blue lines. It gives slightly overestimation where y=- 1.5 and 3.0 mm near the inner of recirculation zone and it is found an underestimation in turbulence at y=-6.0 mm near the inner and outer edge of the recirculation zone where the cell size is not fine enough. However, the combination of MR/RNG $k-\epsilon$ model gives a good prediction for a turbulent cavitating flow.

The second results calculated by $k-\omega$ SST model were shown in red lines, which indicates good results where y=- 1.5 and 3.0 mm near the inner of recirculation zone, and

it is found similar an underestimation in turbulence at y=-6.0 mm near the outer edge of the recirculation zone where the cell size is not fine enough.

Although, the third results calculated by LES shown in green lines gives a slight underestimation near the outer edge of the recirculation zone, where the cell size is not very fine, it is found that it gives a reasonable prediction for a turbulent flow with a recirculation flow for all positions where y=- 1.5, -3.0 and -6.0 mm.

These findings showed that turbulence models are highly mesh dependence, where RNG $k-\epsilon$ model can predict good results with more coarse mesh compared to $k-\omega$ SST model, and LES models requires much more fine grids within recirculation zone. Therefore, before deciding whether turbulence model properly works or not, it is important to find out correct mesh range where the model works properly.

Finally, it should be noted that RANS turbulence modelling has an important shortcoming since it averages over all the turbulent scales and thus, gives a time-averaged field. However, LES model provides time-dependent fields and takes into account the small scale eddies using sub-grid model.

8.5 Summary

In this Chapter, applicability of MR equation with various turbulence models to the to turbulent cavitating flows in a rectangular nozzle is presented in order to predict quantitatively the cavitation thickness and length, and to simulate cavitation cloud shedding captured by a high-speed camera inside the nozzle of a fuel injector. For this purpose, within the framework of RANS, the two-equation turbulence models such as $k-\omega$ SST and RNG $k-\epsilon$ models with various meshes of different cell sizes and one equation eddy viscosity sub-grid scale model under the framework of Large Eddy Simulation (LES) are tested to simulate the turbulent cavitation flow, whose liquid velocity was measured by Laser Doppler Velocimetry (LDV). As a result, following findings are obtained:

- The RNG $k-\epsilon$ model with MR equation gives a good prediction for the turbulent cavitating flow in the nozzle with a fine mesh of about 25 - 50 μm in the minimum mesh size Δx_{min}. Also, the transient motion of cavitation in the recirculation zone, such as cloud shedding is well captured by RNG $k-\varepsilon$ using minimum mesh size Δx_{min}=50 μm.

- The $k-\omega$ SST model with MR equation gives a good prediction for the turbulent

cavitating flow in the nozzle with a finer mesh equal and lower than 25 μm in Δx_{min}. Also, the transient motion of cavitation in the recirculation zone, such as cloud shedding is well captured with the combination of MR/$k-\omega$ SST model using minimum mesh size Δx_{min}=25 μm.

- The reverse flow structure and observation of the transient motion of vortex accompanied by clouds shedding until the exit of the nozzle are well simulated with the combination of MR/LES models using fine grid where minimum mesh size is Δx_{min}=4.4 μm compared to RANS models.

- Finally, this study showed that turbulence models are highly mesh dependence. Therefore, before deciding whether turbulence model works or not, it is important to find out model's mesh range where it works properly.

Chapter 9

Conclusion

In this present thesis, a cavitation model, which is based on bubble dynamics and taking into account critical pressure P_C, is proposed. First, the proposed model is assessed by comparing bubble radii with the existing bubble dynamics bubble dynamics models, i.e., the Rayleigh-Plesset (RP) equation, simplified RP which is called Rayleigh (R) equation under the various cases, such as a at low water injection pressure and at high diesel injection pressure. Before this assessment, the validity of RP equation is confirmed through the calculated and measured bubble radii.

Next, the applicability of the various combinations of different cavitation models to simulate the unsteady transient cavitating flows in a nozzle of liquid fuel injector for diesel engines is examined.

First, the applicability of the barotropic cavitation model and Kunz's cavitation models which are not based on bubble dynamics approach, are investigated. A barotropic cavitation model is coupled with Homogeneous Equilibrium Model (HEM)and RNG $k-\varepsilon$ turbulence model, whereas Kunz's cavitation model is combined with the Volume-of-Fluids (VOF), Mass Transfer Model (MTM) and RNG $k-\varepsilon$ model.

Second, the combination in a house code based on Lagrangian Bubble Tracking Method (BTM), RP equation and Large Eddy Simulation (LES) is examined.

Third, the combination of Volume-of-Fluids (VOF), RNG $k-\varepsilon$ model and Mass Transfer Model (MTM), whose source terms rre given by R or MR equations, is tested using OpenFOAM.

Finally, the effect of the turbulence model on cavitation simulation have been tested using two-equation turbulence models under the definition of RANS, such as; $k-\omega$ SST and RNG $k-\varepsilon$ models with various meshes of different cell sizes and one equation eddy viscosity model under the framework of Large Eddy Simulation (LES) with fine mesh.

All CFD simulations are validated by comparing with the experimental data, which is obtained using one-side rectangular nozzle whose images are captured by a high-speed camera and the turbulent velocity was measured by a Laser Doppler Velocimetry (LDV). The findings and some important results of the present thesis can be summarized as follows:

- The Rayleigh–Plesset (RP) equation gives a good prediction for the radius of a spherical bubble without bubble–bubble interaction, bubble–wall interaction, bubble deformation, coalescence, and breakup, only when the time step Δt is enough small.

- Regarding to first assessment of the proposed MR model, when the pressure P_L around the bubble is lower than the critical pressure P_C ($P_L < P_C$), R and MR equations give identical results with a large Δt for the estimation of the bubble growth as provided by RP equation. However, when P_L lies between P_C and P_V ($P_C < P_L < P_V$), the R equation overestimates the bubble growth rate, where MR equation gives a good prediction for the bubble diameter at a wide range of pressure with a large time step Δt.

- The R equation also gives wrong estimation in the case of bubble collapse since its predictions always tend to overestimate, whereas the MR equation gives a small error in the estimation of bubble collapse rate, which is reduced by modifying the collapse rate coefficient.

- Regarding to CFD simulation with the combination of HEM, Baro and RNG $k - \epsilon$ under-estimates the cavitation region and results in a wrong prediction for cavitation length and thickness. Also, it cannot reproduce transient cavitation behaviour, which plays a dominant role in atomization of injected liquid jet and spray. Therefore, applicability of barotropic model into modelling of the nozzle cavitation is limited.

- Regarding to Kunz's model, it is found that tuning of model constant parameters are so important. The original value 100 for the model constants gives underestimation for the cavitation region, and results in wrong prediction for the cavitation length and thickness within recirculation zone. It is also unable to capture the cavitation cloud shedding. After tuning model parameters to 1000, the combination of VOF, Kunz

and RNG $k-\epsilon$ models results in good prediction and gives better estimation in the sense of cavity length and thickness within nozzle. Also, the transient motion such as cavitation cloud shedding in the recirculation zone is well predicted. Therefore, tuning of the model constants is crucial for the correct applicability of Kunz's cavitation model.

- The length and thickness of the cavitation zone,and a recirculation flow near the inlet edge and the vortex shedding from the tail of the reattachment point are successfully predicted by the combination of Lagrangian Bubble Tracking Method (BTM), RP equation and Large Eddy Simulation (LES). Also, a cavitation cloud in a vortex shedding from the tail of the cavitation zone is well reproduced by solving the RP equation for all nuclei and bubbles tracked in a Lagrangian manner for incipient cavitation regime. It should be noted that this combination requires a fine grid and a long CPU time, and is applicable only to incipient cavitation with a low void fraction.

- Regarding to feasibility and applicability of the proposed MR equation, it is found out that R equation over-estimates cavitation region from the points of cavity length and thickness, while MR equation based on the critical pressure P_C gives better estimation in the sense of cavity length and thickness. Also, the transient motion of cavitation in the recirculation zone, such as the cavitation cloud shedding, the development of the re-entrant jet and the cavity break-off was well predicted with the combination of MR and RNG $k-\epsilon$. This approach is easy to be employed and applied for cavitation simulation inside nozzle since it does not need very fine grid, and therefore it has a short CPU time.

- Regarding to effects of different turbulence models on the nozzle cavitation, it is obtained that RNG $k-\epsilon$ with MR equation gives a good prediction for the turbulent cavitating flow in the nozzle with a fine mesh of about 25 - 50 μm in the minimum mesh size Δx_{min}. Also, the transient motion of cavitation in the recirculation zone, such as cloud shedding is well captured by RNG $k-\varepsilon$ using minimum mesh size Δx_{min}=50 μm.

- The $k-\omega$ SST model with MR equation gives good prediction for the turbulent cavitating flow in the nozzle with a finer mesh equal and lower than 25 μm in Δx_{min}. Also, the transient motion of cavitation in the recirculation zone, such as cloud shedding is well captured with the combination of MR/$k-\omega$ SST model using minimum mesh size Δx_{min}=25 μm.

- The reverse flow structure and observation of the transient motion of vortex accompanied by clouds shedding until the exit of the nozzle are well simulated with the combination of MR/LES models using fine grid where minimum mesh size is Δx_{min}=4.4 μm compared to RANS models.

- This study showed that turbulence models are highly mesh dependence rather than cavitation model. Therefore, before deciding whether turbulence model works well or not, it is important to correctly determine the model's mesh range where they work properly.

- As a final finding, which concludes that proposed MR equation together with appropriate turbulence model and a fine mesh can simulate not only the complex cavitating recirculation flow, cloud cavitation shedding and re-entrant jet flow but also cavitation thickness, length as well as mean and turbulence velocities quantitatively, and can be used to explore cavitation phenomena inside fuel injector nozzles.

Bibliography

[1] G. G. G. E. D. United State Environmental Protection Agency EPA. *http://www.epa.gov/climatechange/ghgemissions/global.html/*.

[2] W. H. Organization, "Health aspects of air pollution with particulate matter, ozone and nitrogen dioxide: report on a who working group," vol. Bonn, Germany 13-15 January, 2003.

[3] H. Hiroyasu, "Break-up length of a liquid jet and internal flow in a nozzle," in *Proceedings of* 5^{th} *Internatuinal Conference of ICLASS*, pp. 275–282, 1991.

[4] H. Chaves, M. Knapp, A. Kubitzek, F. Obermeier, and T. Schneider, "Experimental study of cavitation in the nozzle hole of diesel injectors using transparent nozzles," tech. rep., SAE Technical Paper, 1995.

[5] C. Badock, R. Wirth, A. Fath, and A. Leipertz, "Investigation of cavitation in real size diesel injection nozzles," *International Journal of Jeat and Fluid Flow*, vol. 20, no. 5, pp. 538–544, 1999.

[6] A. Sou, S. Hosokawa, and A. Tomiyama, "Effects of cavitation in a nozzle on liquid jet atomization," *International Journal of Heat and Mass Transfer*, vol. 50, no. 17, pp. 3575–3582, 2007.

[7] C. Brennen, "Cavitation and bubble dynamics," Oxford University Press, New York, 1995.

[8] R. T. Knapp, J. W. Daily, and F. G. Hammitt, "Cavitation," Institute of Hydraulic Research, University of Iowa, 1979.

[9] A. Andriotis, "Investigation of cavitation inside multi-hole injectors for large diesel engines and its effect on the near-nozzle spray structure," in *PhD Thesis, City Univeristy*, 2009.

[10] L. He and F. Ruiz, "Effect of cavitation on flow and turbulence in plain orifices for high-speed atomization," *Atomization and Sprays*, vol. 5, no. 6, 1995.

[11] C. Soteriou, R. Andrews, and M. Smith, "Direct injection diesel sprays and the effect of cavitation and hydraulic flip on atomization," tech. rep., SAE Technical Paper, 1995.

[12] W. Lauterborn and C. D. Ohl, "Cavitation bubble dynamics," *Ultrasonics Sonochemistry*, vol. 4, no. 2, pp. 65–75, 1997.

[13] M. E. Henry and S. H. Collicott, "Visualization of internal flow in a cavitating slot orifice," *Atomization and Sprays*, vol. 10, no. 6, 2000.

[14] E. Winklhofer, E. Kull, E. Kelz, and A. Morozov, "Comprehensive hydraulic and flow field documentation in model throttle experiments under cavitation conditions," in *ILASS-Europe,* 17^{th} *International Conference on Liquid Atomization and Spray Systems*, 2001.

[15] A. Andriotis, M. Gavaises, and C. Arcoumanis, "Vortex flow and cavitation in diesel injector nozzles," *Journal of Fluid Mechanics*, vol. 610, pp. 195–215, 2008.

[16] T. Hayashi, M. Suzuki, and M. Ikemoto, "Visualization of internal flow and spray formation with real size diesel nozzle," in 12^{th} *Triennial International Conference on Liquid Atomization and Spray Systems, ICLASS*, pp. 2–6, 2012.

[17] H. Watanabe, M. Nishikori, T. Hayashi, M. Suzuki, N. Kakehashi, and M. Ikemoto, "Visualization analysis of relationship between vortex flow and cavitation behavior in diesel nozzle," *International Journal of Engine Research*, vol. 16, no. 1, pp. 5–12, 2015.

[18] D. P. Schmidt, C. J. Rutland, and M. L. Corradini, "A fully compressible, two-dimensional model of small, high-speed, cavitating nozzles," *Atomization and Sprays*, vol. 9, no. 3, 1999.

[19] A. Sou, B. Biçer, and A. Tomiyama, "Numerical simulation of incipient cavitation flow in a nozzle of fuel injector," *Computers & Fluids*, vol. 103, pp. 42–48, 2014.

[20] G. H. Schnerr and J. Sauer, "Physical and numerical modeling of unsteady cavitation dynamics," in 4^{th} *International Conference on Multiphase Flow, New Orleans, USA*, vol. 1, 2001.

[21] A. K. Singhal, M. M. Athavale, H. Li, and Y. Jiang, "Mathematical basis and validation of the full cavitation model," *Journal of Fluids Engineering*, vol. 124, no. 3, pp. 617–624, 2002.

[22] R. F. Kunz, D. A. Boger, D. R. Stinebring, T. S. Chyczewski, J. W. Lindau, H. J. Gibeling, S. Venkateswaran, and T. Govindan, "A preconditioned navier–stokes method for two-phase flows with application to cavitation prediction," *Computers & Fluids*, vol. 29, no. 8, pp. 849–875, 2000.

[23] A. Alajbegovic, D. Greif, B. Basara, and U. Iben, "Cavitation calculation with the two-fluid model," in 3^{rd} *European-Japanese Two-Phase Flow Group Meeting, Certosa di Pontignano*, 2003.

[24] P. J. Zwart, A. G. Gerber, and T. Belamri, "A two-phase flow model for predicting cavitation dynamics," in *Proceedings of the* 5^{th} *International Conference on Multiphase Flow, Yokohama, Japan*, 2004.

[25] C. L. Merkle, J. Feng, and P. E. Buelow, "Computational modeling of the dynamics of sheet cavitation," in 3^{rd} *International Symposium on Cavitation, Grenoble, France*, vol. 2, pp. 47–54, 1998.

[26] E. Giannadakis, M. Gavaises, and C. Arcoumanis, "Modelling of cavitation in diesel injector nozzles," *Journal of Fluid Mechanics*, vol. 616, pp. 153–193, 2008.

[27] OpenFOAM. `http://www.opencfd.co.uk`.

[28] W. Bergwerk, "Flow pattern in diesel nozzle spray holes," *Proceedings of the Institution of Mechanical Engineers*, vol. 173, no. 1, pp. 655–660, 1959.

[29] R. Spikes and G. Pennington, "Discharge coefficient of small submerged orifices," *Proceedings of the Institution of Mechanical Engineers*, vol. 173, no. 1, pp. 661–674, 1959.

[30] W. Nurick, "Orifice cavitation and its effect on spray mixing," *Journal of Fluids Engineering*, vol. 98, no. 4, pp. 681–687, 1976.

[31] K. J. Wu, C. C. Su, R. Steinberger, D. Santavicca, and F. Bracco, "Measurements of the spray angle of atomizing jets," *Journal of Fluids Engineering*, vol. 105, no. 4, pp. 406–413, 1983.

[32] J. Bode, H. Chaves, F. Obermeier, and T. Schneider, "'influence of cavitation in turbulent nozzle flow on atomization and spray formation of a liquid jet," *Proceedings, Sprays and Aerosols*, vol. 91, pp. 107–112, 1991.

[33] C. Soteriou, M. Smith, and R. Andrews, "Diesel injection: laser light sheet illumination of the development of cavitation in orifices," in *IMECHE Conference Transactions*, pp. 137–158, 1998.

[34] C. Soteriou, R. Andrews, and M. Smith, "Further studies of cavitation and atomization in diesel injection," tech. rep., SAE Technical Paper, 1999.

[35] C. Arcoumanis, H. Flora, M. Gavaises, and M. Badami, "Cavitation in real-size multi-hole diesel injector nozzles," tech. rep., SAE Technical Paper, 2000.

[36] H. Roth, M. Gavaises, and C. Arcoumanis, "Cavitation initiation, its development and link with flow turbulence in diesel injector nozzles," tech. rep., SAE Technical Paper, 2002.

[37] A. L. Knox-Kelecy and P. V. Farrell, "Spectral characteristics of turbulent flow in a scale model of a diesel fuel injector nozzle," tech. rep., SAE Technical Paper, 1993.

[38] M. Kato, H. Kano, K. Date, T. Oya, and K. Niizuma, "Flow analysis in nozzle hole in consideration of cavitation," tech. rep., SAE Technical Paper, 1997.

[39] L. Ganippa, G. Bark, S. Andersson, and J. Chomiak, "Comparison of cavitation phenomena in transparent scaled-up single-hole diesel nozzles," *http://resolver. caltech. edu/cav2001: sessionA9. 005*, 2001.

[40] E. Matsumura, T. Tomita, K. Takeda, S. Furuno, and J. Senda, "Analysis of visualized fuel flow inside the slit nozzle of direct injection si gasoline engine," tech. rep., SAE Technical Paper, 2003.

[41] R. Ochoterena, P. Li, M. Vera-Hernández, and S. Andersson, "Influence of cavitation on atomisation at low pressures using up-scaled and transparent nozzles," in 23^{rd}

Annual ILASS-Europe Conference on Liquid Atomization and Spray Systems, Brno, Czech Republic, 2010.

[42] S. R. Kim, K. W. Ku, J. G. Hong, and C. W. Lee, "An experimental investigation of discharge coefficient and cavitation length in the elliptical nozzles," in *ILASS-Europe 2010,* 23^{rd} *Annual Conference on Liquid Atomization and Spray Systems*, Brno, Czechoslovakia, 2010.

[43] M. Blessing, G. Konig, C. Kruger, U. Michels, and V. Schwartz, "Analysis of flow and cavitation phenomena in diesel injection nozzles and its effects on spray and mixture formation," in *Fuel Injection Systems 2003: IMechE Conference Transactions 2003*, vol. 2, p. 21, 2003.

[44] S. H. Collicott and H. Li, "True-scale true-pressure internal flow visualization for diesel injectors," tech. rep., SAE Technical Paper, 2006.

[45] K. H. Goney and M. L. Corradini, "Isolated effects of ambient pressure, nozzle cavitation and hole inlet geometry on diesel injection spray characteristics," tech. rep., SAE Technical Paper, 2000.

[46] J. Desantes, R. Payri, F. Salvador, and J. Gimeno, "Measurements of spray momentum for the study of cavitation in diesel injection nozzles," tech. rep., SAE Technical Paper, 2003.

[47] V. Macian, V. Bermudez, R. Payri, and J. Gimeno, "New technique for determination of internal geometry of a diesel nozzle with the use of silicone methodology," *Experimental Techniques*, vol. 27, no. 2, pp. 39–43, 2003.

[48] J. Walther, J. Schaller, R. Wirth, and C. Tropea, "Investigation of internal flow in transparent diesel injection nozzles using fluorescent particle image velocimetry," in *Proceeding of ICLASS*, vol. 20, 2000.

[49] P. Aleiferis, Y. Hardalupas, D. Kolokotronis, A. Taylor, and T. Kimura, "Investigation of the internal flow field of a diesel model injector using particle image velocimetry and cfd," tech. rep., SAE Technical Paper, 2007.

[50] W. Yuan and G. H. Schnerr, "Numerical simulation of two-phase flow in injection nozzles: Interaction of cavitation and external jet formation," *Journal of Fluids Engineering*, vol. 125, no. 6, pp. 963–969, 2003.

[51] M. Battistoni and C. N. Grimaldi, "Analysis of transient cavitating flows in diesel injectors using diesel and biodiesel fuels," tech. rep., SAE Technical Paper, 2010.

[52] C. W. Hirt and B. D. Nichols, "Volume of fluid (vof) method for the dynamics of free boundaries," *Journal of Computational Physics*, vol. 39, no. 1, pp. 201–225, 1981.

[53] O. Ubbink and R. Issa, "A method for capturing sharp fluid interfaces on arbitrary meshes," *Journal of Computational Physics*, vol. 153, no. 1, pp. 26–50, 1999.

[54] J. Brackbill, D. B. Kothe, and C. Zemach, "A continuum method for modeling surface tension," *Journal of computational physics*, vol. 100, no. 2, pp. 335–354, 1992.

[55] R. Marcer and J. LeGouez, "Simulation of unsteady cavitating flows in diesel injector with an improved vof method," in 17^{th} *ILASS-Europe Conference*, 2001.

[56] V. Srinivasan, A. J. Salazar, and K. Saito, "Modeling the disintegration of cavitating turbulent liquid jets using a novel vof–cimd approach," *Chemical Engineering Science*, vol. 65, no. 9, pp. 2782–2796, 2010.

[57] E. Roohi, A. P. Zahiri, and M. Passandideh-Fard, "Numerical simulation of cavitation around a two-dimensional hydrofoil using vof method and les turbulence model," *Applied Mathematical Modelling*, vol. 37, no. 9, pp. 6469–6488, 2013.

[58] Y. Dellanoy and J. Kueny, "Two phase flow approach in unsteady cavitation modeling," in *Cavitation and Multiphase Flow Forum*, vol. 98, pp. 153–158, 1990.

[59] D. P. Schmidt, C. J. Rutland, and M. Corradini, "A numerical study of cavitating flow through various nozzle shapes," tech. rep., SAE Technical Paper, 1997.

[60] G. B. Wallis, "One-dimensional two-phase flow," McGraw-Hill, 1969.

[61] F. P. Karrholm, H. Weller, and N. Nordin, "Modelling injector flow including cavitation effects for diesel applications," in 5^{th} *Joint Fluids Engineering Conference*, pp. 465–474, American Society of Mechanical Engineers, 2007.

[62] F. Salvador, J.-V. Romero, M.-D. Roselló, and J. Martínez-López, "Validation of a code for modeling cavitation phenomena in diesel injector nozzles," *Mathematical and Computer Modelling*, vol. 52, no. 7, pp. 1123–1132, 2010.

[63] F. Salvador, J. Martínez-López, J.-V. Romero, and M.-D. Roselló, "Influence of biofuels on the internal flow in diesel injector nozzles," *Mathematical and Computer Modelling*, vol. 54, no. 7, pp. 1699–1705, 2011.

[64] B. Biçer, A. Tanaka, T. Fukuda, and A. Sou, "Numerical simulation of cavitation phenomena in diesel injector nozzles," in 16^{th} *Annual Conference on Liquid Atomization & Spray Systems (ILASS Asia)*, 2013.

[65] O. Coutier-Delgosha, R. Fortes-Patella, and J.-L. Reboud, "Evaluation of the turbulence model influence on the numerical simulations of unsteady cavitation," *Journal of Fluids Engineering*, vol. 125, no. 1, pp. 38–45, 2003.

[66] R. K. Avva, A. K. Singhal, and D. H. Gibson, "An enthalpy based model of cavitation," *ASME-Publications-Fed*, vol. 226, pp. 63–70, 1995.

[67] N. Dumont, O. Simonin, and C. Habchi, "Numerical simulation of cavitating flows in diesel injectors by a homogeneous equilibrium modeling approach," in *Proceeding of* 4^{th} *International Symposium on Cavitation (CAV2001)*, 2001.

[68] W. Xie, T. Liu, and B. Khoo, "Application of a one-fluid model for large scale homogeneous unsteady cavitation: The modified schmidt model," *Computers & Fluids*, vol. 35, no. 10, pp. 1177–1192, 2006.

[69] E. Goncalves and R. F. Patella, "Numerical simulation of cavitating flows with homogeneous models," *Computers & Fluids*, vol. 38, no. 9, pp. 1682–1696, 2009.

[70] L. Rayleigh, "Viii. on the pressure developed in a liquid during the collapse of a spherical cavity," *The London, Edinburgh, and Dublin Philosophical Magazine and Journal of Science*, vol. 34, no. 200, pp. 94–98, 1917.

[71] S. Kim, "A numerical study of unsteady cavitation on a hydrofoil," in *Proceedings of the* 7^{th} *International Symposium on Cavitation, Ann Arbor, MI, USA*, 2009.

[72] M. Morgut, E. Nobile, and I. Biluš, "Comparison of mass transfer models for the numerical prediction of sheet cavitation around a hydrofoil," *International Journal of Multiphase Flow*, vol. 37, no. 6, pp. 620–626, 2011.

[73] Y. L. Young and B. R. Savander, "Numerical analysis of large-scale surface-piercing propellers," *Ocean Engineering*, vol. 38, no. 13, pp. 1368–1381, 2011.

[74] A. Gosset, M. Lema, and F. L. Peña, "Periodic phenomena on a partially cavitating hydrofoil," in *Proceedings of the* 8^{th} *International Symposium on Cavitation*, pp. 685–690, 2012.

[75] Z. Shang, D. R. Emerson, and X. Gu, "Numerical investigations of cavitation around a high speed submarine using openfoam with les," *International Journal of Computational Methods*, vol. 9, no. 3, 2012.

[76] C. Deimel, M. Günther, and R. Skoda, "Application of a pressure based cfd code with mass transfer model based on the rayleigh equation for the numerical simulation of the cavitating flow around a hydrofoil with circular leading edge," in *EPJ Web of Conferences*, vol. 67, p. 02018, EDP Sciences, 2014.

[77] T. Watanabe, T. Kawamura, Y. Takekoshi, M. Maeda, and S. H. Rhee, "Simulation of steady and unsteady cavitation on a marine propeller using a rans cfd code," in *Proceedings of the* 5^{th} *International Symposium on Cavitation, Osaka, Japan*, 2003.

[78] M. Dular, R. Bachert, B. Stoffel, and B. Širok, "Experimental evaluation of numerical simulation of cavitating flow around hydrofoil," *European Journal of Mechanics-B/Fluids*, vol. 24, no. 4, pp. 522–538, 2005.

[79] S. Som, S. Aggarwal, E. El-Hannouny, and D. Longman, "Investigation of nozzle flow and cavitation characteristics in a diesel injector," *Journal of Engineering for Gas Turbines and Power*, vol. 132, no. 4, pp. 1–12, 2010.

[80] A. Kubota, H. Kato, H. Yamaguchi, *et al.*, "A new modelling of cavitating flows: A numerical study of unsteady cavitation on a hydrofoil section," *Journal of Fluid Mechanics*, vol. 240, no. 1, pp. 59–96, 1992.

[81] H. Kato, H. Kayano, and Y. Kageyama, "A consideration of thermal effect on cavitation bubble growth," tech. rep., American Society of Mechanical Engineers, New York, NY (United States), 1994.

[82] Y. Chen and S. D. Heister, "Two-phase modeling of cavitated flows," *Computers & Fluids*, vol. 24, no. 7, pp. 799–809, 1995.

[83] I. Senocak and W. Shyy, "A pressure-based method for turbulent cavitating flow computations," *Journal of Computational Physics*, vol. 176, no. 2, pp. 363–383, 2002.

[84] V. Srinivasan, A. Salazar, and K. Saito, "Computational prediction of the flow inside cavitating injectors by supplementing a homogeneous equilibrium model (hem) with a pressure correction equation," in *Proceeding International Congress on Liquid Atomization and Spray Systems (ICLASS), Kyoto, Japan*, 2006.

[85] V. Srinivasan, A. J. Salazar, and K. Saito, "Numerical simulation of cavitation dynamics using a cavitation-induced-momentum-defect (cimd) correction approach," *Applied Mathematical Modelling*, vol. 33, no. 3, pp. 1529–1559, 2009.

[86] R. E. Bensow and G. Bark, "Implicit les predictions of the cavitating flow on a propeller," *Journal of Fluids Engineering*, vol. 132, no. 4, p. 041302, 2010.

[87] R. Payri, B. Tormos, J. Gimeno, and G. Bracho, "The potential of large eddy simulation (les) code for the modeling of flow in diesel injectors," *Mathematical and Computer Modelling*, vol. 52, no. 7, pp. 1151–1160, 2010.

[88] B. Ji, X. Luo, R. E. Arndt, X. Peng, and Y. Wu, "Large eddy simulation and theoretical investigations of the transient cavitating vortical flow structure around a naca66 hydrofoil," *International Journal of Multiphase Flow*, vol. 68, pp. 121–134, 2015.

[89] B. Biçer and A. Sou, "Bubble dynamics model for predicting the growth and collapse of cavitation bubbles in diesel injector," *Atomization and Sprays*, vol. 24, no. 10, 2014.

[90] M. S. Plesset and A. Prosperetti, "Bubble dynamics and cavitation," *Annual Review of Fluid Mechanics*, vol. 9, no. 1, pp. 145–185, 1977.

[91] W. Yuan, J. Sauer, and G. H. Schnerr, "Modeling and computation of unsteady cavitation flows in injection nozzles," *Mécanique & Industries*, vol. 2, no. 5, pp. 383–394, 2001.

[92] J.-P. Franc, "Physics and control of cavitation," tech. rep., DTIC Document, 2006.

[93] T. Leighton, *The acoustic bubble*. Academic Press, 1994.

[94] A. Sou and T. Kinugasa, "Numerical simulation of developing cavitating flow in a nozzle of pressure atomizer," in *Thiesel Conference on Thermo and Fluid Dynamic Processes in Diesel Engines, Valencia, Spain*, 2010.

[95] K. Tomoyuki, S. Akira, and K. Yusuke, "Numerical models of cavitation in fuel injector," in *Proceeding of International Symposium on Marine Engineering (ISME) Oct. 17–21, Kobe, Japan*, 2011.

[96] W. Yuan and G. H. Schnerr, "Optimization of two-phase flow in injection nozzles: interaction of cavitation and external jet formation," in *Joint US-European Fluids Engineering Division Conference*, pp. 431–438, American Society of Mechanical Engineers, 2002.

[97] A. Vogel, W. Lauterborn, and R. Timm, "Optical and acoustic investigations of the dynamics of laser-produced cavitation bubbles near a solid boundary," *Journal of Fluid Mechanics*, vol. 206, pp. 299–338, 1989.

[98] Y. Tomita and A. Shima, "High-speed photographic observations of laser-induced cavitation bubbles in water," *Acta Acustica United with Acustica*, vol. 71, no. 3, pp. 161–171, 1990.

[99] H. Lin, B. D. Storey, and A. J. Szeri, "Inertially driven inhomogeneities in violently collapsing bubbles: the validity of the rayleigh–plesset equation," *Journal of Fluid Mechanics*, vol. 452, pp. 145–162, 2002.

[100] S. Popinet and S. Zaleski, "Bubble collapse near a solid boundary: a numerical study of the influence of viscosity," *Journal of Fluid Mechanics*, vol. 464, pp. 137–163, 2002.

[101] Z. Qin, K. Bremhorst, H. Alehossein, and T. Meyer, "Simulation of cavitation bubbles in a convergent–divergent nozzle water jet," *Journal of Fluid Mechanics*, vol. 573, pp. 1–25, 2007.

[102] S. Fujikawa and T. Akamatsu, "Effects of the non-equilibrium condensation of vapour on the pressure wave produced by the collapse of a bubble in a liquid," *Journal of Fluid Mechanics*, vol. 97, no. 3, pp. 481–512, 1980.

[103] S. H. Yang, S. Y. Jaw, and K. C. Yeh, "Single cavitation bubble generation and observation of the bubble collapse flow induced by a pressure wave," *Experiments in Fluids*, vol. 47, no. 2, pp. 343–355, 2009.

[104] P. K. Sweby, "High resolution schemes using flux limiters for hyperbolic conservation laws," *SIAM Journal on Numerical Analysis*, vol. 21, no. 5, pp. 995–1011, 1984.

[105] B. Biçer and A. Sou, "Numerical models for simulation of cavitation in diesel injector nozzles," *Atomization and Sprays*, vol. 25, no. 1, pp. 1–18, 2015.

[106] A. Sou and A. Tomiyama, "Numerical simulations of liquid jet deformation based on hybrid combination of interface tracking and bubble tracking methods," *Multiphase Science and Technology*, vol. 17, no. 1-2, 2005.

[107] A. Sou, Y. Masaki, and T. Nakajima, "Numerical analysis of cavitating flow in a spray nozzle," in *ILASS-Asia,* 6^{th} *Annual Conference on Liquid Atomization and Spray Systems*, pp. 283–288, 2001.

[108] B. Befrui, G. Corbinelli, D. Robart, W. Reckers, and H. Weller, "Les simulation of the internal flow and near-field spray structure of an outward-opening gdi injector and comparison with imaging data," tech. rep., SAE Technical Paper, 2008.

[109] K. Jagus, X. Jiang, G. Dober, G. Greeves, N. Milanovic, and H. Zhao, "Assessment of large-eddy simulation feasibility in modelling the unsteady diesel fuel injection and mixing in a highspeed direct-injection engine," *Proceedings of the Institution of Mechanical Engineers, Part D: Journal of Automobile Engineering*, vol. 223, no. 8, pp. 1033–1048, 2009.

[110] A. Vreman, "An eddy-viscosity subgrid-scale model for turbulent shear flow: Algebraic theory and applications," *Physics of Fluids*, vol. 16, no. 10, pp. 3670–3681, 2004.

[111] M. Hirano and A. Tomiyama, "A numerical method for an adiabatic two-fluid model based on the modified sola method. 1st report, numerical solution method.," *Trans JSME*, vol. 58, no. 556, pp. 3613–3618, 1992.

[112] V. Yakhot, S. Orszag, S. Thangam, T. Gatski, and C. Speziale, "Development of turbulence models for shear flows by a double expansion technique," *Physics of Fluids A: Fluid Dynamics*, vol. 4, no. 7, pp. 1510–1520, 1992.

[113] H. K. Versteeg and W. Malalasekera, *An introduction to computational fluid dynamics: the finite volume method*. Pearson Education, 2007.

[114] B. Van Leer, "Towards the ultimate conservative difference scheme. iv. a new approach to numerical convection," *Journal of Computational Physics*, vol. 23, no. 3, pp. 276–299, 1977.

[115] F. R. Menter, "Two-equation eddy-viscosity turbulence models for engineering applications," *The American Institute of Aeronautics and Astronautics (AIAA) Journal*, vol. 32, no. 8, pp. 1598–1605, 1994.